State of Oregon
Oregon Department of Geology and Mineral Industries
Brad Avy, State Geologist

OPEN-FILE REPORT O-19-04

COMPARISON OF OREGON TSUNAMI HAZARD SCENARIOS TO A PROBABILISTIC TSUNAMI HAZARD ANALYSIS (PTHA)

by George R. Priest and Jonathan C. Allan[1]

2019

[1]Oregon Department of Geology and Mineral Industries, Coastal Field Office, P.O. Box 1033, Newport, OR 97365

DISCLAIMER

This product is for informational purposes and may not have been prepared for or be suitable for legal, engineering, or surveying purposes. Users of this information should review or consult the primary data and information sources to ascertain the usability of the information. This publication cannot substitute for site-specific investigations by qualified practitioners. Site-specific data may give results that differ from the results shown in the publication.

Oregon Department of Geology and Mineral Industries Open-File Report O-19-04
Published in conformance with ORS 516.030

DOGAMI Administrative Offices
800 NE Oregon Street, Suite 965
Portland, OR 97232
Telephone (971) 673-1555
https://www.oregongeology.org/
https://www.oregon.gov/DOGAMI/

TABLE OF CONTENTS

LIST OF FIGURES

LIST OF TABLES

EXECUTIVE SUMMARY

The Oregon Department of Geology and Mineral Industries (DOGAMI) published in 2013 coast-wide velocity, flow depth, and momentum flux data for five Cascadia subduction zone (CSZ) tsunami inundation scenarios (categorized in "T-shirt" sizes of SM1, M1, L1, XL1, and XXL1) (Priest and others, 2013; Witter and others, 2013). This paper is primarily aimed at evaluating which scenario best approximates a 1,000-yr exceedance event based on comparison of results generated from a 2019 probabilistic tsunami hazard analysis (PTHA) undertaken by AECOM Technology Corporation (Thio, 2019). We also compare DOGAMI and AECOM wave amplitudes at 100 m depth for 2,475-yr (Thio, 2017) and 1,000-yr exceedances (Thio, 2019). Based on a quasi-probabilistic PTHA considering only CSZ earthquake source parameters, the DOGAMI M1 scenario should approximate a conservative 1,000-yr exceedance event. The next larger DOGAMI scenario, L1, would be a highly conservative choice for a 2,475-yr exceedance. However, AECOM PTHAs do not generally match these estimates. In general, the 1,000-yr and 2,475-yr tsunami amplitudes at 100 m depth offshore resemble DOGAMI scenarios L1 and XL1, respectively. Tsunami flow depths, velocities, and momentum flux data at open coastal bridge sites in northern and central Oregon generally followed the same pattern. Open coastal sites on the south coast had AECOM tsunami flow depths and inundation resembling or slightly smaller than the SM1 scenario. Understanding the reasons for the mismatch with the quasi-probabilistic PTHA was hampered by lack of access to digital point data on slip and vertical deformation of AECOM CSZ sources, recurrences of sources, and details of the PTHA computations. Some potential reasons may be AECOM's use of (1) much larger coseismic slips than deemed reasonable by DOGAMI from consideration of slip balance on the CSZ for the last ~10,000 yrs of paleoseismic record, (2) much heavier emphasis than DOGAMI on partial CSZ fault ruptures known to have occurred over the last 10,000 yrs on the southern CSZ, and (3) global seismic data not representative of the CSZ to estimate coseismic slip from rupture area.. Comparison of AECOM to DOGAMI data is difficult at inland sites owing to some mismatches of digital elevation models (DEMs) used in the respective studies and possible differences in numerical models, as well as adoption of zero bottom friction by DOGAMI versus Thio's Manning friction coefficient of 0.025.

If any DOGAMI tsunami scenarios are to be used for bridge design, we recommend that the scenarios be conservatively large to reflect the relatively large uncertainties revealed by comparison of the DOGAMI and AECOM approaches. For example, the tsunami amplitudes of AECOM at 100 m depth approximate the DOGAMI scenario L1 at 1,000-yr exceedance and XL1 at 2,475-yr exceedance so use of these two DOGAMI scenarios for these exceedances should encompass hazard estimates of both approaches. Any new simulations of these or other source scenarios should be run with improved inputs, including bottom friction and computational grid spacing small enough to simulate key elements of each site. Time histories of current forces and direction should be extracted to evaluate how long peak forces persist. These time histories are not routinely provided by a PTHA unless obtained by disaggregation of the simulations and collecting time history data during each computer run.

1.0 INTRODUCTION

The Oregon Department of Transportation (ODOT) with funding support from California and Washington, commissioned Dr. Hong Kie Thio (AECOM Technology Corporation) to produce 1,000-yr exceedance probabilistic tsunami hazard maps for the western United States (Thio, 2019[1]). This work effectively builds on a collaborative probabilistic tsunami hazard analysis (PTHA) originally undertaken by the Pacific Earthquake Engineering Research Center (PEER), the U.S. Geological Survey (USGS), the California Department of Transportation (Caltrans), the California Geological Survey (CGS), and American Society of Civil Engineers (ASCE) to produce 2,475-year exceedance tsunami inundation maps for the five western U.S. states. The purpose of the 1,000-year exceedance study is to develop American Association of State Highway and Transportation Officials (AASHTO) design standards and guidance for mitigating tsunami hazards around bridges, especially as it relates to estimation of tsunami current forces (momentum fluxes).

ODOT contracted with Oregon Department of Geology and Mineral Industries (DOGAMI) to evaluate in a report the PTHA results of AECOM (Thio, 2019) compared with results of tsunami inundation modeling undertaken by DOGAMI between 2009 and 2013 of the Cascadia subduction zone (CSZ) (Priest and others, 2009, 2010, 2013; Witter and others, 2011, 2013). This report summarizes that comparison but also includes similar comparisons of AECOM tsunami amplitudes at 100 m depth for a 2,475-yr exceedance (Thio, 2017[2]) and 1,000-yr exceedance (Thio, 2019).

Deterministic earthquake source scenarios for the DOGAMI work are full-length ruptures of the Cascadia megathrust and the corresponding surface deformation (Witter and others, 2011, 2013). The scenarios reflect five CSZ earthquake size classes defined by peak slip deficit (years of CSZ convergence) released: small (SM, 300 yrs), medium (M, 310–660 yrs), large (L, 680–1,000 yrs) and extra-large (XL, 1,050–1,200 yrs). A fifth scenario termed extra-extra-large (XXL) assumes 1,200 years of slip deficit release, differing from the XL scenario only by not reducing slip progressively north to south. XXL is a maximum considered event used in evacuation planning for the State of Oregon. According to Witter and others (2013), these size classes correspond to approximate recurrence rates as follows: SM, 1/2,000 yrs; M, 1/1,000 yrs; L, 1/3,333 yrs; and XL, <1/10,000 yrs. Recurrence for the XXL event was not estimated. The five tsunami sizes were intended to cover the possible model space for the ~40+ CSZ tsunamis inferred from paleoseismic data to have occurred in the last 10,000 years.

The immediate objective of this project is to determine how closely tsunami forces at typical coastal bridges compare between the DOGAMI and AECOM (Thio, 2019) tsunami simulations. The long-term objective is to determine the best and most cost-effective approach for estimating the current forces of a 1,000-yr exceedance tsunami for bridge design. Specific objectives for this initial study are:

1) Compare AECOM 1,000-year exceedance data to DOGAMI deterministic tsunami scenarios with emphasis on scenarios with estimated recurrences 1/1,000 years (M) and 1/3,333 years (L);
2) Compare at an initial 6 to 8 bridge sites identified for the Oregon coast.
3) Compare modeled tsunami flow depths, current velocities, momentum flux, and inundation extents for each bridge site, identifying differences between the two data sets.

[1] Thio, H. K., 2019, Notes on the production of the 1,000 year probabilistic tsunami hazard maps for the Western United States: draft report (in review) by AECOM to the California Geological Survey.

[2] Thio, H. K., 2017, Probabilistic tsunami hazard maps for the State of California (phase 2): draft report (in review) by AECOM to the California Geological Survey.

4) Produce a technical report describing the model characteristics, differences, and the results of the model comparisons. The report should provide the necessary geologic reasoning for any differences and anomalies.

This report demonstrates at nine U.S. Highway 101 bridge sites in Oregon (**Figure 1-1**) that although there are differences between the AECOM and DOGAMI tsunami data, flow depths, velocities, and momentum flux values overlap at nearly every bridge site. The sources of these differences are differing digital elevation models (DEMs), assumptions about bottom friction, CSZ earthquake sources, and the fact that the DOGAMI deterministic approach differs fundamentally from the AECOM PTHA. Unlike a deterministic study that selects individual scenarios to represent each size class of tsunami, PTHA takes account of the relative importance of each source of uncertainty plus recurrence of each size class. For example, a PTHA provides a tsunami flow depth that will not likely be exceeded in a 1,000-yr observation period based on an amalgamation of many tsunami sources and the uncertainties of predicting flow depth from each.

Figure 1-1. Location map of bridge sites chosen for detailed comparison of DOGAMI and Thio (2019) tsunami data. R. = River; Hwy = Highway; Cr. = Creek.

2.0 METHODS

2.1 Approach

The approach is to compare DOGAMI (Witter and others, 2011, 2013; Priest and others, 2013; Allan and others, 2018) and AECOM (Thio, 2017, 2019) tsunami data at coastal sites and at 100 m water depth offshore. The offshore comparisons are particularly useful, because the tsunami simulations in deep water are relatively free of influence from differences between the DOGAMI and AECOM bottom friction, inundation models, and digital elevation models (DEMs). For coastal sites we extracted values of tsunami velocity, flow depth, and momentum flux at computational grid points from DOGAMI and AECOM that lie close together at vulnerable ODOT bridge sites on the north, central, and south coast, explaining differences and similarities. We chose for comparisons nine bridges and one point at the Coquille River estuary mouth at Bandon (**Figure 1-1**); the latter was chosen to contrast how quickly tsunami forces decrease upstream between the Thio (2019) simulations that use a Manning friction coefficient (n) of 0.025 and the 2011 or 2013 DOGAMI simulations that use zero bottom friction. DOGAMI simulations using n = 0.025 and n = 0.030 (Allan and others, 2018) are also available for comparison at the Astoria, Highway 101 bridge over the Columbia River, as well as along the Columbia River navigation channel (mouth to Bonneville Dam). Tillamook County bridge sites are not compared owing to a computational grid error there that affects tsunami simulations of Priest and others (2013). A summary of modeling factors and capabilities of the two approaches is given in **Table 2-1** with qualitative estimates of the importance of each.

Table 2-1. Comparison of modeling parameters used by DOGAMI (Witter and others, 2011, 2013) and AECOM (Thio, 2017, 2019). PTHA is probabilistic tsunami hazard analysis; CSZ is Cascadia subduction zone; n is Manning friction coefficient.

Modeling Parameter	Effect on 1,000-yr Exceedance Force Prediction	DOGAMI Deterministic Analysis	AECOM PTHA
aleatory uncertainties (e.g. chaotic asperities)	moderate to high, depending on how implemented	no	yes
epistemic uncertainties (e.g. geological and physical models)	high	yes, but more could be included	yes, but modifications probably needed
bottom friction (n)	high inland; low at open coast and offshore	no n = 0, except for recent modeling in the Columbia River	yes, n = 0.025
splay fault	high on north coast, low to no effect on south coast	yes	no, although the shallow (within 1 km depth) CSZ rupture model was intended to simulate a splay fault scenario
slip distribution updip and downdip on the CSZ	variable, depending on which Thio distribution is considered	1 "bell-shaped" distribution with 3 rupture scenarios that sample parts of the distribution	1 resembles Witter and others shallow buried rupture source; 1 with full slip to within 1 km depth may produce tsunamis very different from Witter and others
CSZ slip balance over the last 10,000 years	high	yes	no
actual CSZ convergence rate (varying with latitude)	moderate; affects slip budget check on possible sources	yes	no (Thio assumes a nearly constant rate of 20–25 mm/yr)
smoothly variable (unstructured) grid	small to moderate	yes	no (structured grid with nesting)
simulation of small estuarine channels	high	yes	not always, but could be addressed by DEM revision
simulation of coseismic subsidence of the coast	moderate	yes	yes
Tide	variable (proportional to ratio of tsunami height to tide; probably low for 1,000-yr tsunamis in Oregon)	static, mean higher high water (MHHW)	static, mean high water (MHW) for inundation but probabilistic for offshore exceedance amplitudes
provides 1,000-yr exceedance values	high	no, but results can be recast into a quasi-probabilistic estimate of which scenarios approximate a 1,000-yr exceedance	yes
extraction of time histories of force magnitude and direction	high, because allows judgement on whether force duration is long enough to be significant	yes	not routinely, but could be extracted by disaggregation of sources provided time history data were collected in each simulation
accurate momentum flux	high	yes for open coast and deep water; overestimates forces inland, because n = 0; can be addressed by rerunning with n = 0.025 or variable n values according to landscape	yes

2.2 Tsunami Simulation

Details of the DOGAMI tsunami simulation methods and data are summarized by Witter and others (2011, 2013), Priest and others (2013), and, for Columbia River simulations incorporating friction, Allan and others (2018). All use the deterministic CSZ earthquake sources and fault dislocation models of Witter and others (2011, 2013) to estimate vertical coseismic deformation assumed to be identical to the initial tsunami wave. All DOGAMI studies simulate tsunami propagation and inundation using the hydrodynamic finite element model SELFE (Semi-implicit Eulerian-Lagrangian Finite Element model) (Priest and others, 2009, 2010; Witter and others, 2012; Zhang and Baptista, 2008; Zhang and others, 2011). The 2018 simulations of the Columbia River use the nearly identical model SCHISM (Semi-implicit Cross-scale Hydroscience Integrated System Model; Zhang and others, 2016a). SELFE passed all standard tsunami benchmark tests (Zhang and Baptista, 2008; Zhang and others, 2011) and closely reproduced observed inundation and flow depths of the 1964 Alaska tsunami in a trial at Cannon Beach (Priest and others, 2009, 2010). More recently, SCHISM successfully passed a suite of standardized tsunami current benchmark tests (Zhang and others, 2016b; Lynett and others, 2017). SELFE and SCHISM use unstructured triangular computational grids with grid spacing varying according to the size of features that need to be simulated, getting down to a few meters for small features like jetties and expanding smoothly to kilometers at abyssal depths in the ocean. Digital elevation models (DEMs) for these grids were derived from lidar data for dry land and tide flats plus bathymetric data of NOAA and some local surveys of estuaries by DOGAMI. All simulations were run using a static mean higher high water (MHHW) tide.

Details of the AECOM tsunami simulation methods and data are summarized by Thio (2017, 2019). For inundation simulations, Thio (2019) used a two-step approach, determining first the offshore tsunami amplitudes from the PTHA of Thio (2017), then simulating tsunami inundation for a suite of scenarios that match offshore amplitudes that are consistent with the maps computed in the first stage. He used a Clawpack[3]-based code that was developed at AECOM. This code passed standard tsunami benchmark tests according to Thio (2017) and was also verified in the Lynett and others (2017) benchmark tests. The final maps were computed from structured rectangular grids with a horizontal spacing of 60 m in deep water and 10 m at shallow depths and on land (**Figure 2-1**). These grids and the underlying DEM are from NOAA (Eakins and Taylor, 2010) and were specifically developed for tsunami inundation modeling. All Thio (2019) inundation simulations were run using a static mean high water (MHW) tide that is ~0.2 m lower than the MHHW tide used by DOGAMI.

[3] "Conservation Laws Package" open-source software.

Figure 2-1. Location map of Thio (2019) 60-m (red) and 10-m (blue) computational grids for Oregon inundation simulations (after Figure 8 of Thio [2019]).

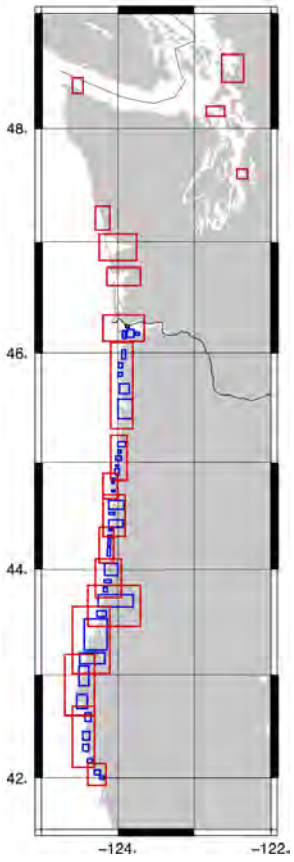

2.3 Comparison of DOGAMI and AECOM Tsunami Sources

Tsunami sources for both the DOGAMI (Witter and others, 2011, 2013) and AECOM (Thio, 2017, 2019) work are subduction zone earthquakes, but AECOM included many more earthquake sources than did DOGAMI to more fully explore aleatory and epistemic uncertainties for PTHA. The Thio (2017) study produced 2,475-yr exceedance wave heights at 100 m water depth offshore based on over 300 CSZ sources of varying length and slip distribution and used all significant distant tsunami sources, albeit with much simpler, maximized slip scenarios compared to the CSZ sources. Both AECOM and DOGAMI relied heavily on estimates of CSZ rupture length and recurrence over the last 10,000 years (**Figure 2-2**) described by Goldfinger and others (2012) and used these factors for the most important basal branches of their r logic trees. Thio (2019) selected 10 CSZ scenarios and 10 distant scenarios for simulations of inundation to build hazard curves at each computational point that encompass 1,000-yr exceedance events for California. For Oregon, DOGAMI focused chiefly on 500- to 10,000-yr events, creating 15 CSZ scenarios and 2 maximum-considered distant scenarios for the initial pilot study of tsunami inundation in the Bandon area of southern Oregon. DOGAMI completed simulations for only 5 of these 15 for the rest of the Oregon coast (SM1, M1, L1, XL1, and XXL1, **Figure 2-3**), all of which amplify coseismic uplift by ramping the megathrust slip up onto a splay fault (**Figure 2-4**, **Figure 2-5**, and **Figure 2-6**; Appendix D, **Figure D-3** and **Figure D-5**). DOGAMI judged that these five scenarios were suitable for emergency and land use planning applications.

Figure 2-2. Extent of Cascadia subduction zone coseismic ruptures and turbidites (light gray labels, T1, T2, etc.) according to Goldfinger and others (2012). Figure is modified from Priest and others (2014) and Goldfinger and others (2012). Dashed light gray lines = potential rupture segment boundaries: NB = Nehalem Bank, HB = Heceta Bank, CB = Coquille Bank. Barkley = Barkley submarine canyon; JDF = Juan da Fuca Plate; Astoria = Astoria submarine canyon; HR = Hydrate Ridge; Rogue = Rogue submarine canyon.

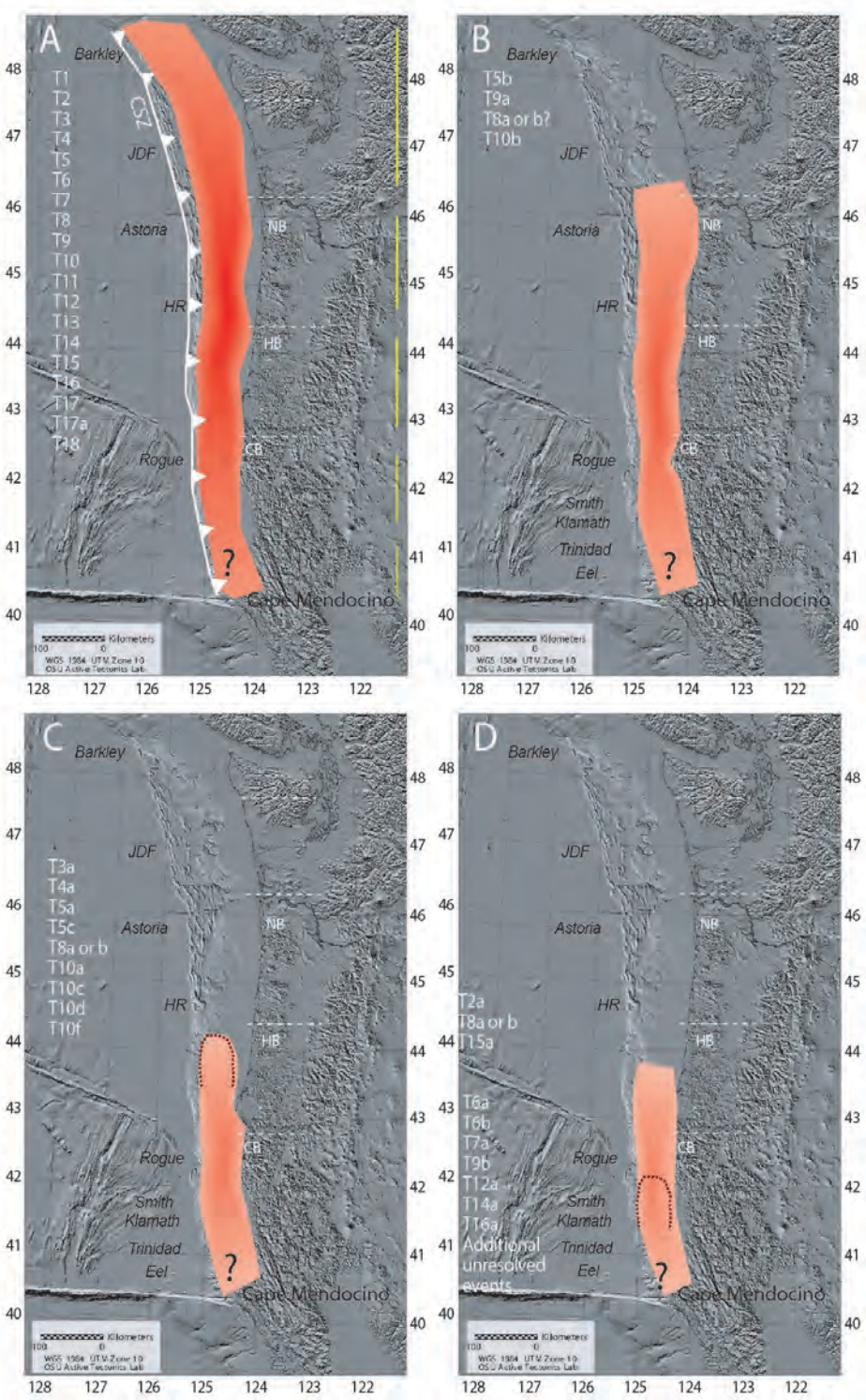

DOGAMI (Witter and others 2011, 2013) relied on global analogues to the CSZ for estimates of slip distribution up and down dip on the Cascadia megathrust, settling on a roughly "bell-shaped" distribution with slip decreasing to zero up and down dip from a peak slip equal to release of 100 percent of CSZ convergence at a fully locked zone tracking roughly along the shelf-slope break (**Figure 2-4**). The amount of peak slip released was then calculated in years multiplied by the convergence rate, which varies along the Cascadia margin (Appendix D, **Figure D-1**; Wang and others, 2003).

Figure 2-3. Schematic logic tree used by DOGAMI (Witter and others, 2011, 2013) to rank 15 Cascadia subduction zone (CSZ) earthquake scenarios. See Table 3 of Witter and others (2011) for a list of all parameters and weights used in the analysis. Earthquake sizes are extra-extra-large (XXL), large (XL), large (L), medium (M), and small (SM); logic tree weights for each earthquake size class is based on the fraction of the 19 full-margin CSZ ruptures that, from paleoseismic data, are thought to have occurred over the last 10,000 yrs. Modified from Witter and others (2011).

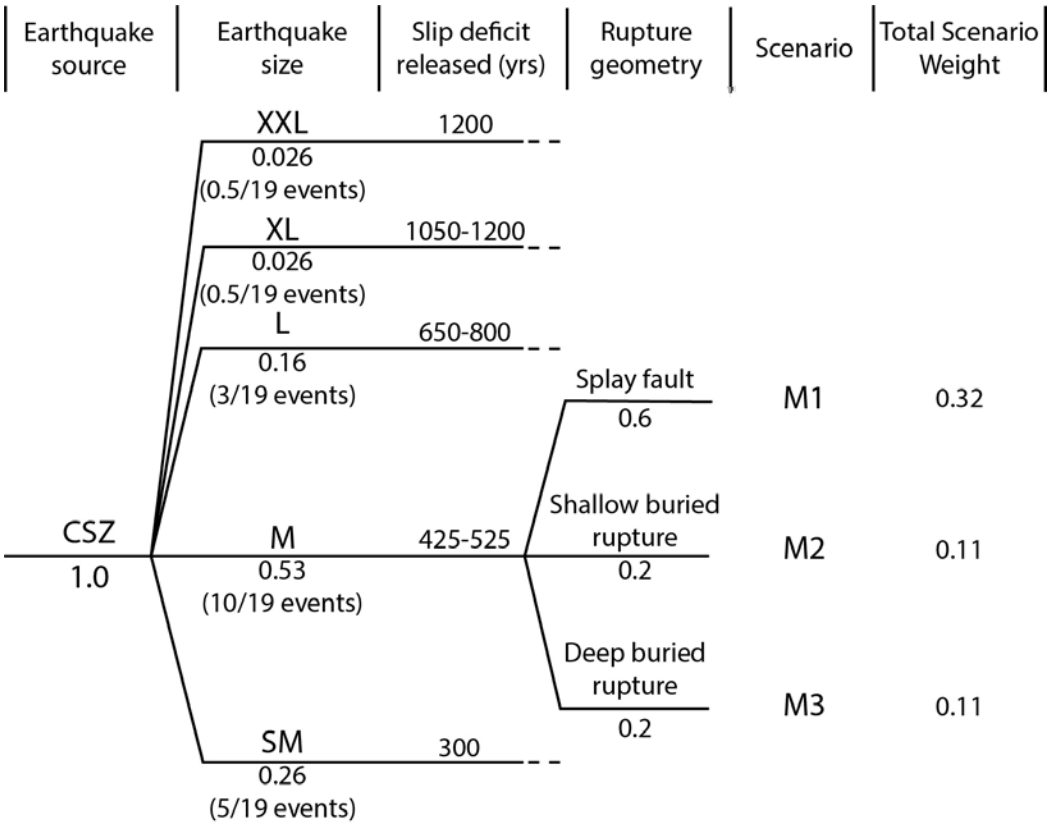

Figure 2-4. Generalized schematic cross section of the Cascadia subduction zone (CSZ) illustrating spatial relationships between geology, bathymetry, and coseismic slip distributions of the three fault sources of DOGAMI (Witter and others, 2011, 2013); approximate locations of the CSZ (black dashed line) and splay fault (red dashed line) are shown on the shaded relief map. The fully locked zone (bottom) stores ~100 percent of the plate convergence, thus building up a slip deficit that is released during the CSZ earthquake. The plates are less and less locked as temperature of the plates increases with depth below the fully locked zone. Between earthquakes the Pleistocene accretionary wedge of sediments scraped off the subducting plate rides passively, protected from deformation by the locked zone. During the earthquake the soft, water-saturated sedimentary rock of the Pleistocene wedge resists penetration by the seismic rupture, stopping the rupture near the seafloor scarp of the megathrust in the shallow buried rupture but stopping deeper in the buried rupture model. For the largest earthquakes much of the fault slip may be partitioned from the megathrust onto the splay fault. See Appendix D for further description of the seismic and interseismic fault rupture processes. There is no vertical exaggeration in cross section X-X'.

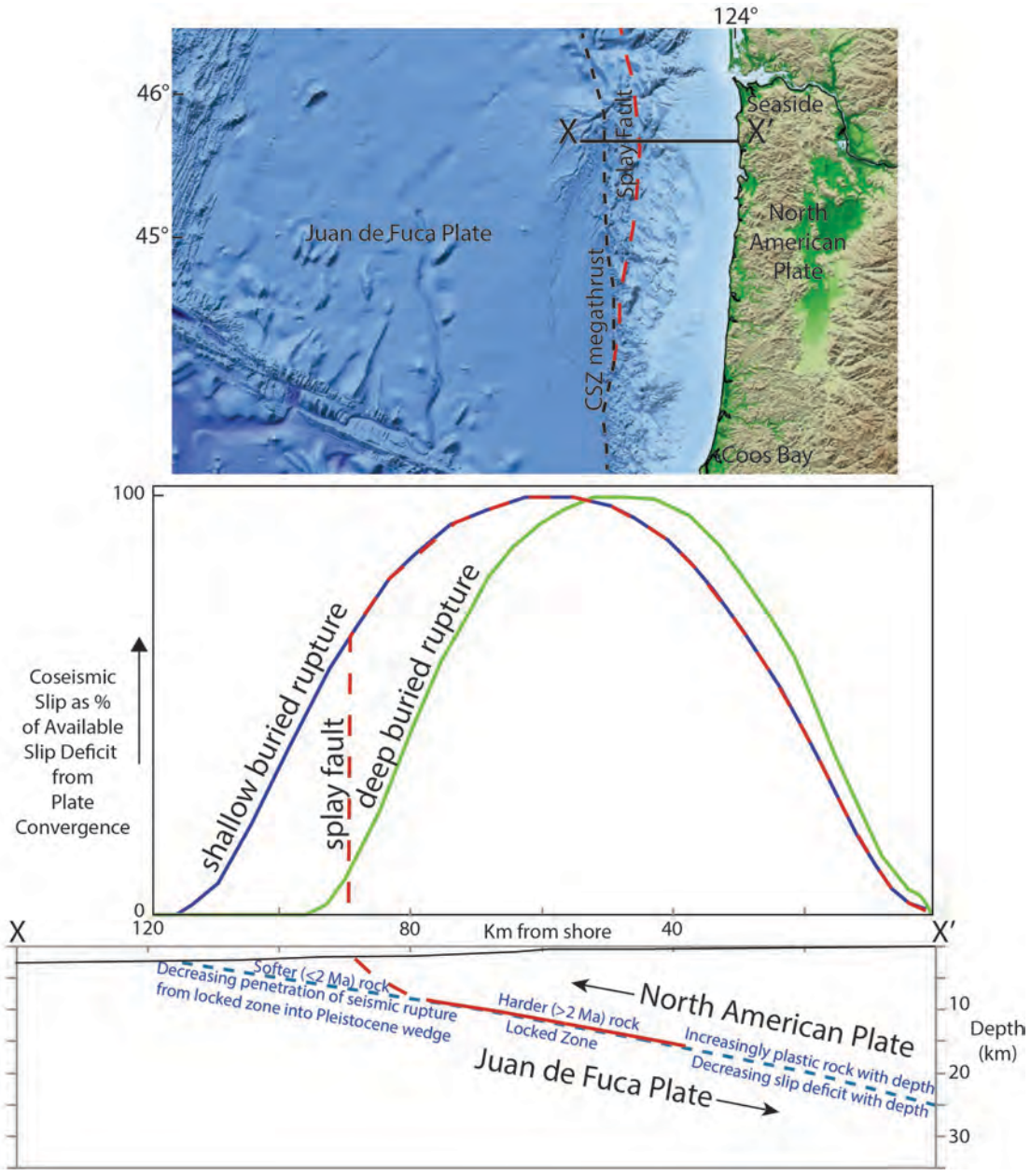

Figure 2-5. (top) Examples of DOGAMI earthquake rupture models using 425 to 525 years of peak slip d employed in Cascadia tsunami simulations of "M" scenarios. (A) Splay fault rupture model for the M1 scenario; dashed line delineates splay fault. (B) The shallow buried rupture model (M2) where the updip limit of slip is at the deformation front. (C) The deep buried rupture deformation model (M3) where the updip limit of rupture is located east of the deformation front where the boundary between the inner (>~2 million yrs) and outer (<~2 million yrs) accretionary wedge (sediment scraped of the subducting JDF plate onto the overriding continental plate) is defined by the change from westward-inclined thrust faults (and associated folds) in the outer wedge to eastward inclined thrust faults in the inner wedge. (bottom) Profiles of fault slip for each model at three locations along the margin: the Olympic Peninsula, Washington; Newport, Oregon; and Cape Blanco, Oregon. Slip profiles plotted as follows: M1 scenario, red; M2 scenario, blue; M3 scenario, green. Note that the splay fault essentially fuses with the surface rupture of the CSZ megathrust by the latitude of Cape Blanco, thus producing no amplification of uplift south of that latitude. Slip patches for each fault model use the same color scheme and extend to the same downdip limit. Taken from Witter and others (2011).

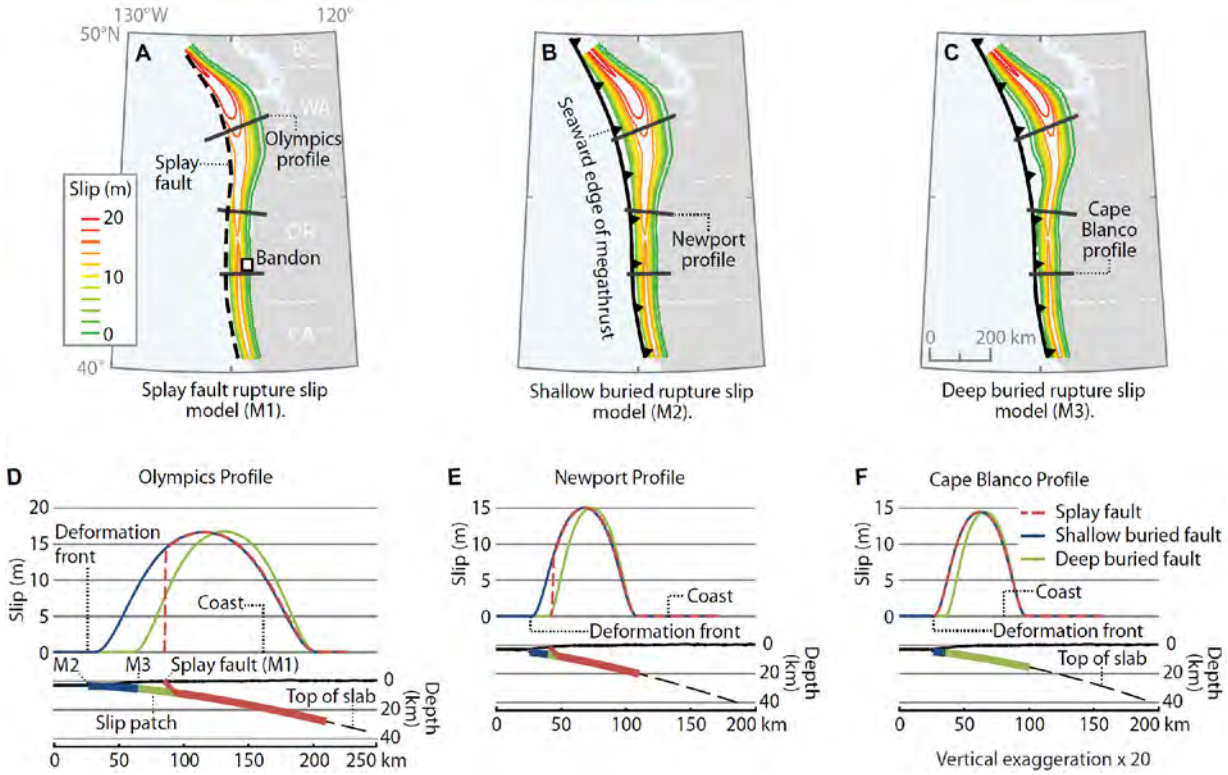

Figure 2-6. Maps of earthquake surface deformation for DOGAMI M1, M2, and M3 fault-rupture models (A, B, C), and profiles showing modeled surface deformation along the Olympics, Newport, and Cape Blanco profiles (D, E, F) for the three fault rupture models: BC—British Columbia; WA—Washington; OR—Oregon; CA—California. Note the amplification of uplift by the splay fault (M1) relative to slip only on the megathrust (M2 and M3). Taken from Witter and others (2011).

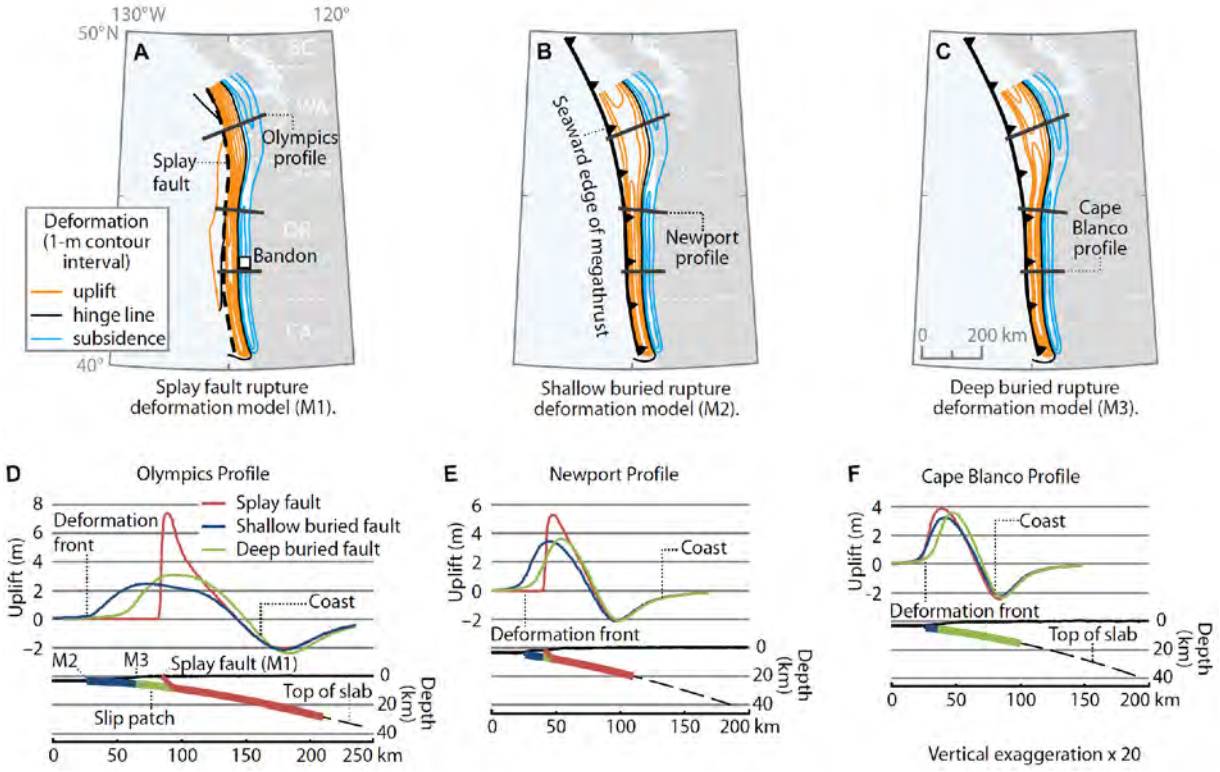

A key constraint on the size (extent and peak slip) of DOGAMI CSZ tsunami sources is the 10,000-yr record of earthquakes recorded offshore as margin-wide sand turbidites (**Figure 2-7**; Goldfinger and others, 2012). The amount of possible coseismic slip in each of the scenarios of **Figure 2-3** was estimated primarily from time intervals between these full-margin turbidites but also influenced by relative masses of turbidites (**Figure 2-7**) and the 10,000-yr slip budget. Each slip scenario except XXL and SM also incorporated a 15–20 percent reduction of slip from north to south to account in the slip budget for ~22 partial ruptures of the CSZ recorded as mud turbidites (**Figure 2-2**; Goldfinger and others, 2012; Witter and others, 2011, 2013; Priest and others, 2013). The matching onshore record of coseismic subsidence and inundation recorded in lakes and marshes (e.g., Witter and others [2012] and many others), when combined with the available coseismic slip from convergence on the CSZ provide severe limits on peak slip available for past earthquakes (e.g., Witter and others, 2011, 2012, 2013; Priest and others, 2017, 2018). For example, 12 CSZ tsunamis known to breach the barrier at Bradley Lake on the southern Oregon coast (near Bandon) over the last ~4,700 yrs require 70–110 percent of the ~4,700 years of slip deficit, even if most of them release only the minimum 8–13 m of peak slip to breach the various landscape possibilities (Witter and others, 2012; Priest and others, 2017, 2018).

Figure 2-7. Scaled turbidite masses of full-margin turbidite deposits over the last ~10,000 yrs (horizontal axis). Age ranges of the largest gaps include error of age dates. Taken from Figure 60a of Goldfinger and others (2012).

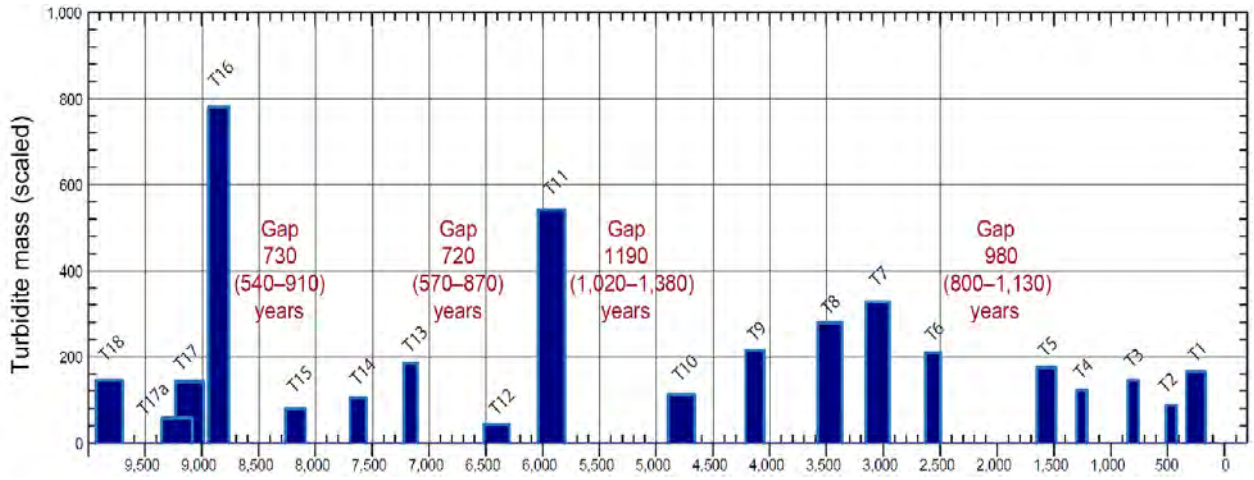

Branch weights in the basal (earthquake size) branch of the DOGAMI logic tree (**Figure 2-3**) are derived from the estimated fraction of the 19 full-margin ruptures (**Figure 2-2**) represented by each size class over the last 10,000 years: 1 XXL or XL, 3 L, 10 M, and 5 SM. These fractions therefore translate to recurrence rates of 1/10,000 yrs for XXL or XL, 1/3,333 yrs for L, 1/1,000 yrs for M, and 1/2,000 yrs for SM. Lower branches in the logic tree explore uncertainties of fault slip distribution in each size class.

The DOGAMI sources did not include partial ruptures of the CSZ recorded offshore in the southern CSZ as mud turbidites (Goldfinger and others, 2012; **Figure 2-2**). The amount of tsunami energy projected north from such ruptures is relatively small, as inferred from theoretical work on long, narrow fault ruptures like the CSZ (e.g., Geist, 1998) and demonstrated by Priest and others (2014, 2017, 2018). DOGAMI decided that the hazard from these partial ruptures was adequately estimated from the small to medium full-margin CSZ scenarios. A full PTHA would have to include the recurrence rates of these ~22 partial ruptures of the southern CSZ, which we explore in the Discussion section.

In a full PTHA, AECOM (Thio, 2017) developed CSZ sources (**Figure 2-8**) from a modification of the National Seismic Hazard Map sources (Petersen and others, 2014, updated by Frankel and others, 2015). AECOM estimated size of the earthquakes from global scaling relationships of Papazachos and others (2004), Strasser and others (2010), and Murotani and others (2013) that are linear regressions correlating seismic moment of modern subduction zone earthquakes to rupture area, mean slip, and asperity size (i.e., patches of extreme slip). In contrast to the DOGAMI full-margin CSZ fault ruptures, AECOM constructed both full and partial ruptures of the CSZ as well as north-south variations in slip within each rupture scenario such that an "asperity" with 2.2 times the mean slip occurred in 1/3 of each rupture (**Figure 2-9**). AECOM also departed from the DOGAMI approach by varying the downdip extent of rupture. DOGAMI did not include this factor, because Priest and others (2010) found in trials that most of the resulting variations in vertical deformation occur on land or in very shallow water and thus have only small effects on resulting tsunamis.

More importantly, AECOM did not include the regional splay fault of DOGAMI (Appendix D, **Figure D-3** and **Figure D-5**) and used different slip distributions for the outer part of the Cascadia megathrust. The AECOM approach is to allow the updip slip to taper to zero over a very shallow depth (0-1 km below the seafloor) and over 0–5 km depth on the megathrust (shallow and deep in **Figure 2-8**). The latter slip distribution should resemble the DOGAMI shallow buried rupture **(Figure 2-4**). Thio (2019, written

communication) intended the former slip distribution to partially emulate splay faulting as well as slip-to-the trench ruptures as in the 2011 Tohoku-oki earthquake. Priest and others (2010) found that in northern Cascadia (at Cannon Beach) the splay fault amplified open coastal tsunami elevations from the shallow buried rupture source (their symmetrical slip source) by ~26–30 percent and inundation by 6–20 percent. This disparity of tsunamis from the splay fault source relative to the deep AECOM source should decrease southward as the splay becomes shallower and finally merges with the surface trace of the megathrust (**Figure 2-4** through **Figure 2-6**, and Appendix D, **Figure D-3**).

The very shallow taper source of AECOM probably creates a larger area of uplift in deep water than do any of the DOGAMI sources. However, estimating the effect on tsunami runup and inundation relative to the DOGAMI sources is difficult without tsunami and coseismic deformation data from this source alone (i.e., separated from the AECOM PTHA). Experiments with the effect of seaward skew of slip relative to the buried symmetrical slip model of DOGAMI and similar model of Priest and others (2010) showed mixed effects in different parts of the coast. Priest and others (2010) found a ~35 percent increase in wave height at Cannon Beach from a seaward skewed source. Seaward skew decreased the ability of tsunamis to breach the Bradley Lake barrier on the southern Oregon coast (Witter and others, 2012). Tohoku-style slip to the trench had little effect on tsunami wave height in northern Cascadia owing to the competing effects of increased uplift at the frontal megathrust but decreased uplift landward relative to the buried symmetric slip model (Gao and others, 2018).

In any case, the likelihood of full slip tapering to zero at 0-1 km depth on the megathrust seems physically problematic and a poor simulation of splay faulting or Tohoku-oki-style slip. A much more gradual slip taper is thought to be typical of most subduction zones (Wang and Hu, 2006; Wang and He, 2008). A more gradual taper is especially likely where the weak Pleistocene accretionary wedge is wide as in northern Oregon and southwestern Washington. In this same locality, potential splay faulting likely starts much deeper on the megathrust than 1 km (**Figure 2-4**; Appendix D) and the continental slope is much lower than the steep slope expected for a Tohoku-oki-style slip-the-trench event (Priest and others, 2014).

Figure 2-8. Schematic logic tree for CSZ sources for the AECOM PTHA; figure taken from Thio (2017).

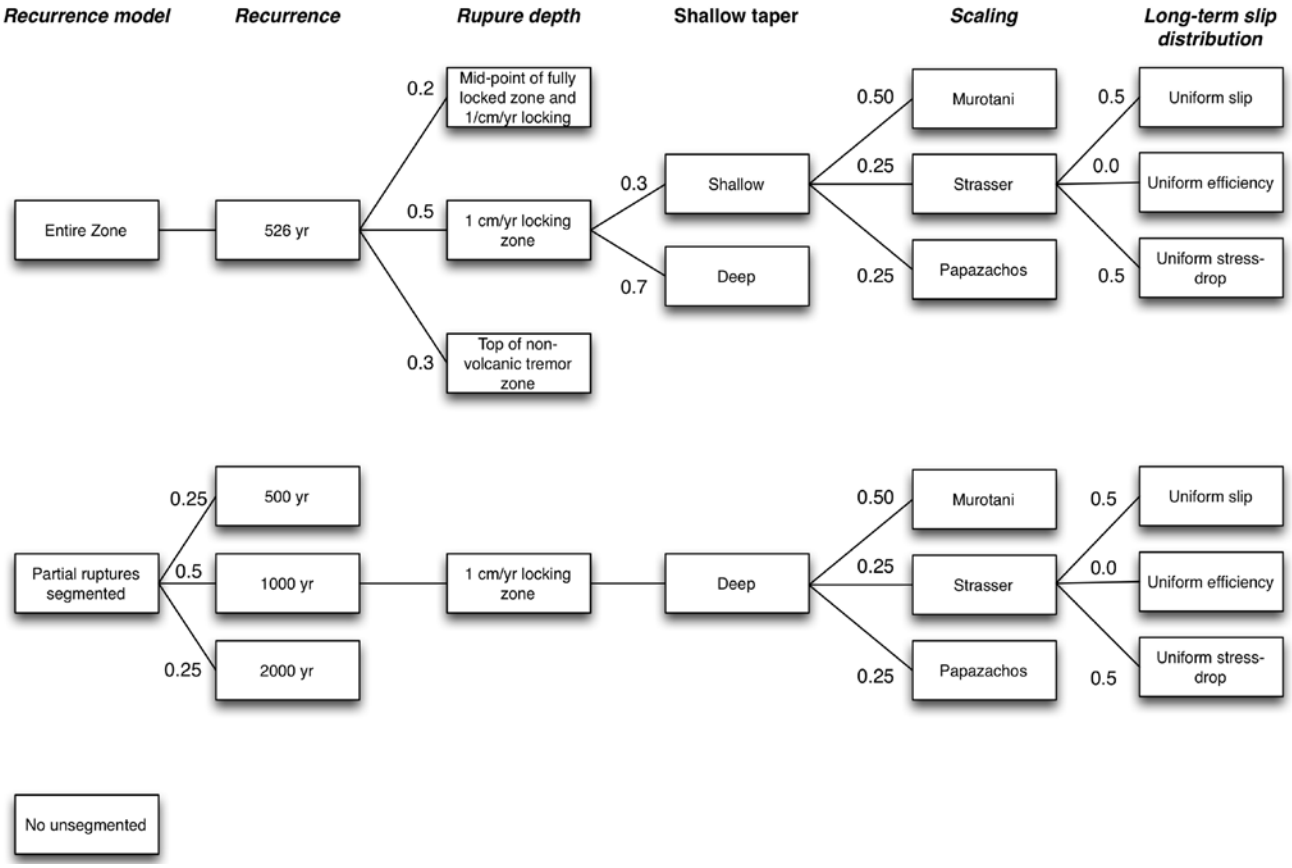

Figure 2-9. Vertical displacement field (red=uplift) for two CSZ scenarios generated by AECOM (Thio, 2019). Top is a full rupture earthquake, bottom is a partial rupture, each shown with three different asperity locations (left, middle, right). Black numbers in the maps are meters of vertical coseismic deformation.

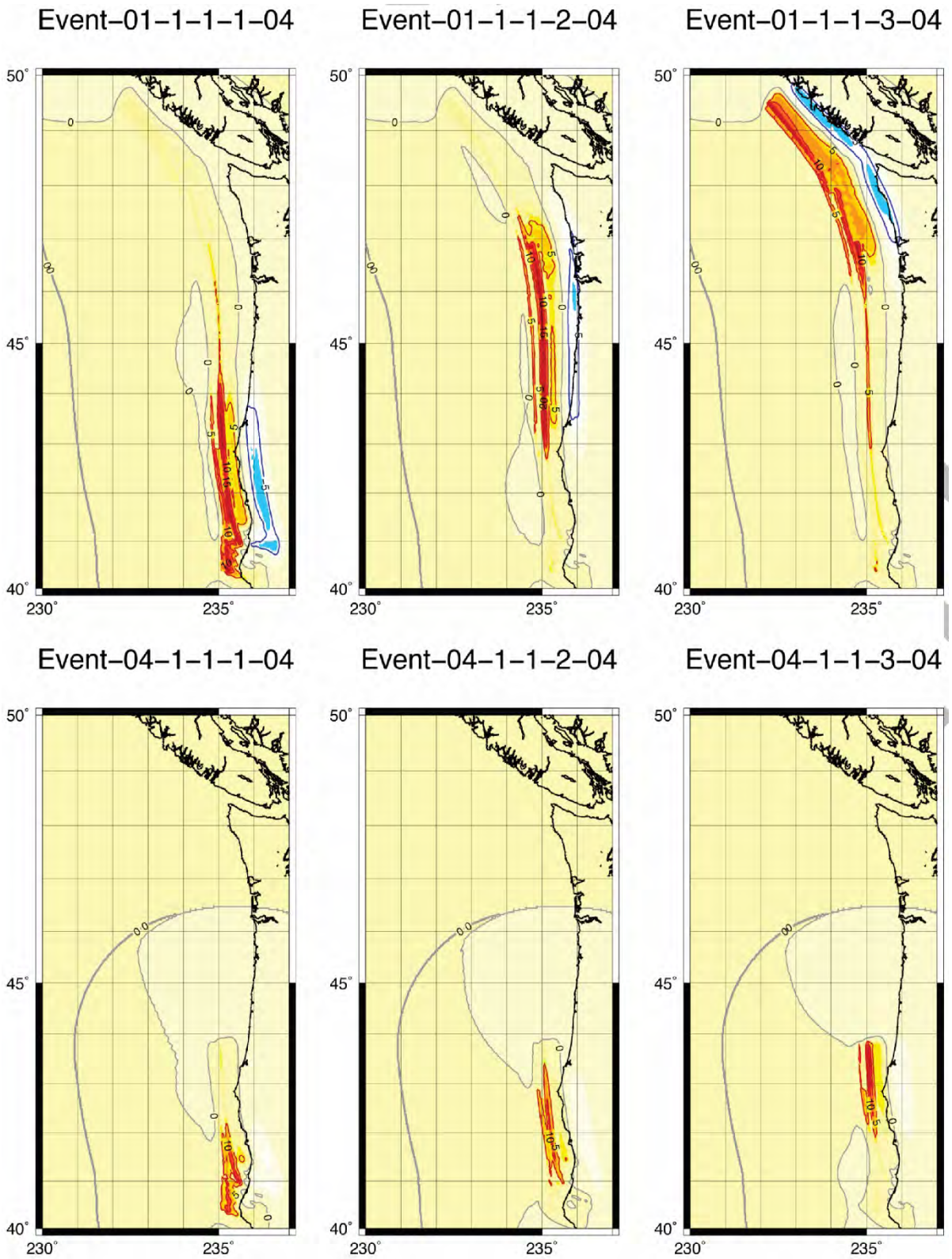

AECOM also departs from DOGAMI by using a limited range of CSZ plate convergence of 20–25 mm/yr rather than the higher, more variable convergence rate (from Euler vectors) for calculation of available seismic slip and slip budget for the CSZ. For example, convergence rate in northern Cascadia is ~40 mm/yr decreasing to ~30 mm/yr in southern Cascadia (McCrory and others, 2012; Appendix D, **Figure D-1**). DOGAMI inferred that available peak slip in their "bell-shaped" slip distribution is some number of years without an earthquake (the slip deficit) times 30–40 mm/yr, with coseismic slip decreasing up and down dip to zero, so the mean slip for an earthquake and tsunami at each latitude would be ~49 percent of this peak slip value. Conversely, AECOM multiplies 20–25 mm/yr (varying from the southern to northern CSZ) by slip deficit years to infer mean coseismic slip available for the earthquake and tsunami. The AECOM peak slip is then be assumed to be concentrated in an asperity occupying 1/3 of the rupture which, based upon global analogues, would have 2.2 times the mean slip. AECOM then subtracts the slip for this asperity from the other 2/3 of the rupture to balance the mean slip for the whole rupture. The AECOM asperity is then moved three times along the length of each rupture to create asperity scenarios for every part of the coast (**Figure 2-9**). Obviously, the DOGAMI sources are all asperity cases in the AECOM framework. As an example, for a slip deficit release of 500 yrs at a convergence rate of ~40 mm/yr in the northern CSZ, AECOM would calculate mean slip by multiplying 25 mm/yr (0.025 m/yr) times 500 yrs, which equals 12.5 m, giving a peak asperity slip of 27.5 m. DOGAMI would multiply 40 mm/yr (0.04 m) times 500 yrs to get a peak slip of 20 m with an approximate mean slip of 0.49 times peak slip, 9.8 m.

DOGAMI does not explore aleatory variabilities from chaotic factors that affect slip distribution and inundation, but source variabilities are addressed by AECOM through use of three asperities in each of the CSZ ruptures. Other factors such as variability in landscape bottom friction during inundation are expressed in terms of distribution functions around a mean and are included in the AECOM PTHA by sampling or integrating over the distribution function. The AECOM approach is to scale up the slip on the fault source to encompass changes of inundation from all variables, including these aleatory factors. According to Thio (2017, p. 13), "the resulting magnitude of the earthquake source can be much larger than the magnitude one would use for a deterministic tsunami scenario."

The two approaches lead to different results for estimates of extreme events and for total slip balance on the CSZ. The deterministic scenarios developed by DOGAMI rigorously balance available slip over the last 10,000 years of paleoseismic record of 40+ CSZ earthquakes. Conversely, the AECOM scenarios do not use this metric to check for slip balance, because those scenarios are not constrained by the 10,000-year record, other than for estimates of recurrence of full-margin (1/526 yrs) and partial ruptures (1/500, 1/1,000, and 1/2,000 yrs in **Figure 2-8**). The AECOM scenarios therefore have the freedom to create slip patches with much larger variation of peak slip than the Witter and others (2011, 2013) patches. For example, mean slip for the AECOM CSZ scenarios varies from 76 to 2 m (Thio, 2017, his Table E-2), whereas mean slip for the DOGAMI scenarios varies from 20 to 5 m (Table 4 of Witter and others, 2011, 2013); likewise, "asperity" slip varies from 167 to 4.4 m (AECOM) and 41 to 10 m (DOGAMI). The largest AECOM asperity patches thus each release CSZ slip deficits at the 30–40 mm/yr convergence rate of 4,175–5,567 years (i.e., about half of the total available slip deficit on the CSZ over the last 10,000 years), whereas the DOGAMI scenarios XL or XXL release no more than 1,200 years of slip deficit (12 percent of the of the last 10,000 years). The largest AECOM asperities probably have quite low effective recurrences, but those recurrences are not tabulated in the AECOM reports. In any case, lack of access to the digital point data on slip and vertical deformation for the 10 AECOM CSZ sources prevents us from making direct comparisons to DOGAMI sources.

Whereas AECOM did not truncate potential slip models at some maximum value, DOGAMI did. DOGAMI judged that the largest time interval on the CSZ without an earthquake in the 10,000-yr record of

turbidites of ~1,150 yrs (revised to 1,190 yrs by Goldfinger and others [2012]; **Figure 2-7**) is a good guide to the largest credible amount of slip deficit that can be released in a single event; they rounded this value up to 1,200 yrs (36–44 m slip) to be conservative. The maximum DOGAMI event was also influenced by maximum slip observed in modern subduction zone earthquakes, ~40 m (e.g., see the Murotani and others [2013] review). From the frequency of this type of gap in the turbidite record, DOGAMI inferred a recurrence of ~1/10,000 yrs for this extreme event. It is also possible to infer a 2/10,000 yrs recurrence for the largest event based on mass of turbidite deposits, because two very large deposits are in the 10,000-yr record (**Figure 2-7**).

3.0 RESULTS

3.1 Comparison of DEMs

Comparing DEMs generated for different computational grids can be challenging, as these differences directly influence the resulting flow depths, current velocities, and momentum flux, making the results somewhat ambiguous. Here, we explore differences in the DEMs used in the AECOM and DOGAMI simulations for the bridge sites. As can be seen in **Table 3-1** and maps of grids and grid differences in Appendix A (**Figure A-1** through **Figure A-21**), the two DEMs differ in many areas but are similar in well-surveyed navigation channels at Astoria, Newport, Bandon, and Gold Beach. In other areas, comparisons could still be made by finding adjacent computational grid points with similar water depths or elevations. In some areas where the mismatch is large this was a challenge. For example, at the Yachats bridge, only a point on dry land came within ~1 m vertical of the AECOM DEM, because elevation data missed much of the river channel.

Dry land and sand bar elevations differ between the two grids in many areas. These differences can generally be attributed to DOGAMI having used detailed lidar elevations. The differences probably contribute to large disparities in simulated inundation between the two approaches in some areas, although it is difficult to separate out this effect from the effect of other factors. In only one locality does the AECOM DEM resolve sand bar and jetty morphology better than the DOGAMI DEMs. At Yaquina Bay in Newport small groins and associated shoals on the south side of the bay are missed by the DOGAMI DEM but are well defined by AECOM (Appendix A, **Figure A-9**). These groins and shoals direct more tsunami flow to the main navigation channel than simulated by DOGAMI, thus amplifying AECOM current velocities and momentum flux there relative to DOGAMI results (see Appendix C, **Figure C-5**).

At Siletz Bay in Lincoln City and Alsea Bay in Waldport neither DEM has accurate bathymetry, owing to lack of surveyed navigation channels (Appendix A, **Figure A-7** and **Figure A-9**, respectively). Alsea Bay sand bars appear somewhat better defined by AECOM, although major channels are generally better captured in the DOGAMI DEM (**Table 3-1**; Appendix A, **Figure A-11** and **Figure A-12**).

Table 3-1. Comparison of digital elevation models (DEMs) of DOGAMI (Witter and others, 2011, 2013; Priest and others, 2013) to AECOM (Thio, 2019) data at adjacent, representative grid points. Obs. Pt. = observation point; Hwy = Highway.

Locality	AECOM Minus DOGAMI Depth (m) at Obs. Pt.	Comments on DEM Accuracy, Correlation, and Effects on Simulation Comparisons
Astoria Hwy 101 Bridge Columbia River	−1.2	AECOM and DOGAMI DEMs are similar.
Seaside Hwy 101 Bridge[1]	0.4	AECOM DEM offset 45 m south and 55 m west (projection error?) but resembles DOGAMI near bridge except creek channel shallower by 3-4 m; no high ground near bridge to judge inundation; AECOM inundates between XL1 and L1 at nearest high ground west; AECOM grid does not extend to high ground east of the bridge.
Cannon Beach Hwy 101 Bridge	−0.3	AECOM channel is poorly defined by too few grid points and generally ~1 m too shallow relative to DOGAMI but DEMS otherwise similar in low-lying areas. AECOM DEM 0–4 m higher on bluff to the north causing inundation to be between L1 and XXL1; probably XXL1 or XL1 inundation are closest to AECOM after erroneously high elevations are removed.
Siletz River Hwy 101 Bridge	0.1	AECOM channel depths ~2-3 m lower than DOGAMI but neither DEM has accurate bathymetry in river or bay; dry land DEMs are similar in low-lying areas but AECOM is higher in highlands and misses the bridge fill at abutments, which are large geomorphic features. Hard to compare inundations.
Yaquina Bay Hwy 101 Bridge, north side	−0.2	AECOM defines groins and associated shoals on the south side of the main channel better than DOGAMI, which could confine and increase AECOM channel flow velocities and tendency to create gyres relative to DOGAMI.
Alsea Bay Hwy 101 Bridge, south side	−0.3	Neither DEM appears to accurately reflect all features of this natural estuary. DOGAMI defines location of channels better than AECOM, but AECOM appears to have more accurate DEM on some sand bars within the estuary; DOGAMI DEM appears to overestimate depths except in middle of channels, so hard to find correspondence between the two DEMs; DOGAMI DEM should yield conservatively high velocities and flow depths relative to AECOM.
Near Yachats Hwy 101 Bridge	−0.1	AECOM DEM misses some deeper channels in Yachats River near mouth and misses the channel at the bridge, placing channel at 2–9.5 m above MHW. Difficult to find matching DEM observation point.
Coquille River Hwy 101 Bridge	0.0	DEMs similar. DOGAMI appears more accurate in shallow water and tide flats but has a default depth of 5.07 m below MHHW in deepest channel (below lidar data coverage) where AECOM has variable depths of unknown quality.
Bandon Mouth	−0.1	DOGAMI and AECOM DEM similar at the mouth of the Coquille River at Bandon.
Gold Beach Hwy 101 Bridge	0.2	DEMs are similar. DOGAMI appears somewhat more accurate in shallow water, on tidal flats, and on dry land but has a default depth of 5.07 m MHHW in deepest channel (below lidar data) where AECOM has variable depths of unknown quality.

[1]Comparison point is on dry land where DOGAMI and AECOM DEM are closest in elevation.

3.2 Comparison of Velocity, Flow Depth, Momentum Flux, and Inundation

Comparison of velocity, flow depth, momentum flux, and inundation at the nine bridges and one open coastal site do not lead to one DOGAMI scenario consistently matching the 1,000-yr exceedance values of AECOM (**Table 3-2** and **Table 3-3;** Appendix B, **Table B-1**, **Figure 3-1** through **Figure 3-3**; Appendix C). Generally larger DOGAMI scenarios match AECOM for more northerly sites relative to southerly sites and for sites closer to the open coast. The latter is caused by most DOGAMI simulations using lower bottom friction (Manning coefficient n = 0) than AECOM (n = 0.025). The former is probably caused by complex modeling factors explored below and in the Discussion section.

Other variations are probably influenced by differences in the DEMs, making direct comparisons difficult. The primary example is the badly mismatched DEM at Yachats (**Table 3-1**, Appendix A, **Figure A-14**). Another is the possible underestimation by DOGAMI of velocities at the Yaquina Bay bridge owing to the computational grid missing groins that might constrict and thus increase current velocity (Appendix A, **Figure A-9** and Appendix C, **Figure C-5**). The latter could potentially be the reason XL1 matches AECOM velocities and momentum flux at the Yaquina Bay bridge observation point even though L1 matches AECOM flow depths (**Table 3-1**; **Figure 3-1** through **Figure 3-3**). Tsunami simulations with the same inputs but with and without the groins would be needed test this.

The Astoria and Bandon-Coquille River sites illustrate the effect of differing values of bottom friction, which strongly affect current velocities. At the Astoria Highway 101 bridge over the Columbia River DOGAMI simulations for the L1 scenario with n = 0 (Priest and others, 2013) and for n = 0.025 and 0.03 (Allan and others, 2018) are available for comparison to AECOM. At Astoria the AECOM flow depth matches L1 with n = 0 and is slightly higher than L1 simulations with friction (**Figure 3-1**), although there is much variation outside of the main shipping channel (Appendix C, **Figure C-1**). In contrast, AECOM velocities and momentum flux at Astoria lie between SM1 and M1 (**Figure 3-2** and **Figure 3-3**). At the much shorter Coquille River estuary at Bandon the AECOM flow depths at the mouth resemble the SM1, SM2, or SM3 scenarios, but velocities and momentum flux are closer to the M1 scenario (**Figure 3-1** through **Figure 3-3**). Friction causes the AECOM velocities and momentum flux to reach SM1, SM2, or SM3 levels 5 km up stream at the Highway 101 bridge over the Coquille River (**Figure 3-2** and **Figure 3-3**).

The north-to-south decrease in AECOM values causes the northern and central coast sites to generally match L1 best, while the most southerly site at Gold Beach generally approximates the M1 or SM1 values. Inundation barely reaches the SM1 scenario at the open coast at Bandon and Gold Beach (**Figure 3-1** through **Figure 3-3**; **Table 3-2** and **Table 3-3**).

An exception to L1 matching the AECOM 1000-yr exceedance in the north occurs at Cannon Beach, where inundation and current velocities for AECOM exceed the XXL1 scenario, while the flow depths closely approximate XL1 results (**Table 3-2** and **Table 3-3**; **Figure 3-1** through **Figure 3-3**). This anomalously large 1,000-yr exceedance tsunami of AECOM may be caused by differences in the earthquake sources and/or in the offshore bathymetry.

Table 3-2. Comparison of velocities and flow depths at coastal sites. n = Manning friction coefficient. ? = uncertain owing to mismatch of AECOM (Thio, 2019) and DOGAMI DEMs at the locality.

Locality	Best Match to AECOM for Velocity	Best Match to AECOM for Flow Depth
Astoria Hwy 101 Bridge Columbia River	M1 for n = 0; L1 for n = 0.025 or 0.03	L1 but also close to L1 with n = 0.025 or 0.03
Seaside Hwy 101 Bridge	M1	L1
Cannon Beach Hwy 101 Bridge	>XXL1	XL1
Siletz River Hwy 101 Bridge	M1?	L1?
Yaquina Bay Hwy 101 Bridge, north side	XL1?	L1
Alsea Bay Hwy 101 Bridge, south side	L1	L1
Near Yachats Hwy 101 Bridge	L1?	XL1?
Coquille River Hwy 101 Bridge, Bandon	SM1, -2, or -3	SM1
Coquille River Mouth, Bandon	M1	SM1, -2, or -3
Gold Beach Bridge	M1	SM1

Table 3-3. Comparison of inundation and momentum flux produced by DOGAMI tsunami scenarios compared with AECOM (Thio, 2019). n = Manning friction coefficient, ? = uncertain owing to mismatch of AECOM and DOGAMI DEMs at the locality, and, in the case of Seaside, lack of AECOM data at the eastern inundation limit.

Locality	Best Match to AECOM for Momentum flux	Best Match to AECOM for Inundation
Astoria Hwy 101 Bridge Columbia River	slightly larger than SM1 in channel but close to L1 with n = 0.25 in shallows[2]	M1
Near Seaside Hwy 101 Bridge	L1	L1
Cannon Beach Hwy 101 Bridge	>XXL1	XXL1
Siletz River Hwy 101 Bridge	L1?	L1?
Yaquina Bay Hwy 101 Bridge, north side	XL1?	M1
Alsea Bay Hwy 101 Bridge, south side	L1	L1
Near Yachats Hwy 101 Bridge	L1?	L1?
Coquille River Hwy 101 Bridge, Bandon	SM1, -2, or -3	SM1, -2, or -3
Coquille River Mouth, Bandon	M1 or L1	SM1
Gold Beach Hwy 101 Bridge[1]	SM1 or M1	SM1

[1]Note that SM1 approximately matches the AECOM inundation at the open coastal bluff too.

[2]See **Figure 6-1**.

Figure 3-1. Maximum tsunami flow depths (m) at observation sites arranged from north (left) to south (right).

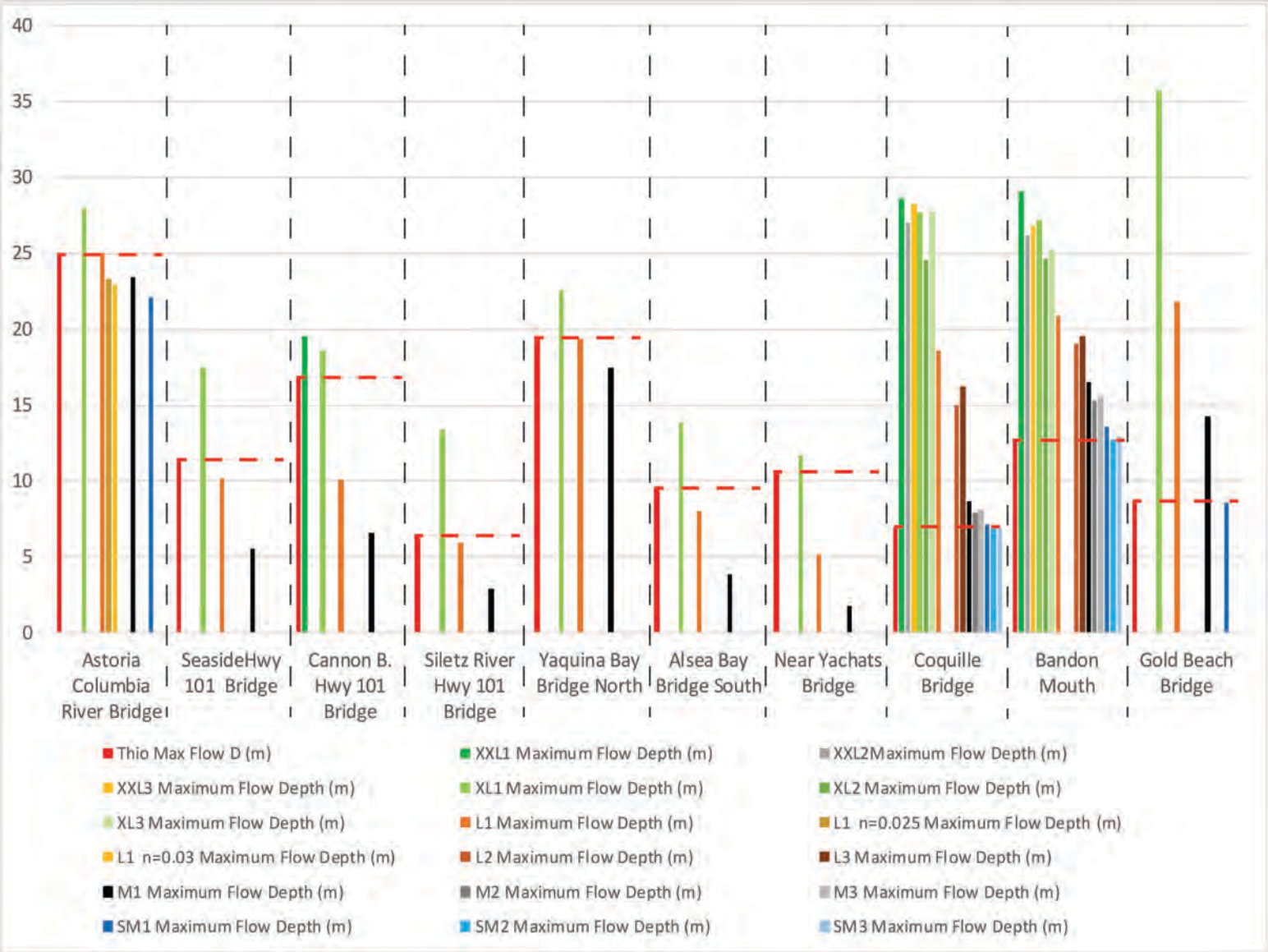

Figure 3-2. Maximum tsunami current velocities (m/s) at observation sites arranged from north (left) to south (right).

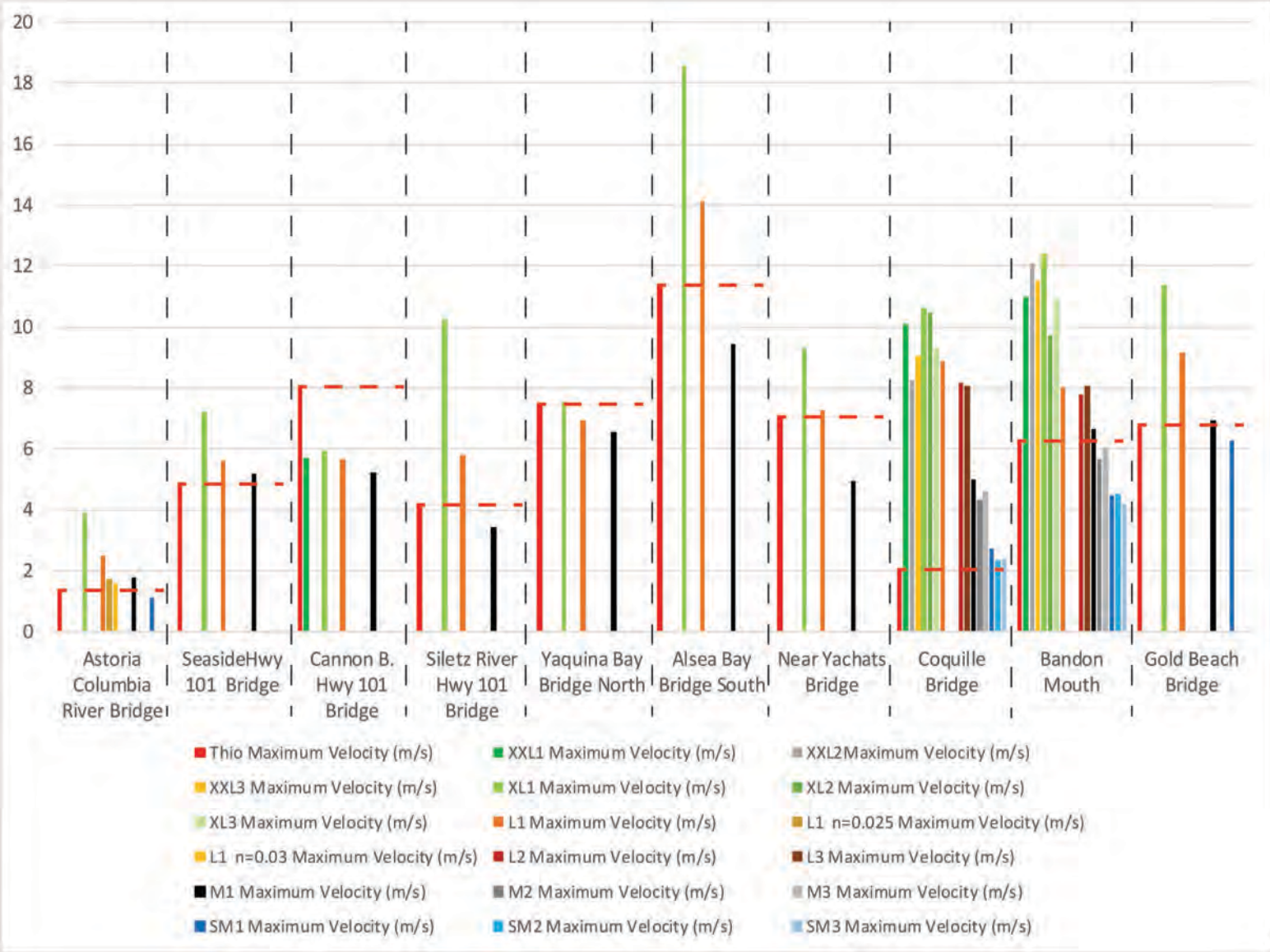

Figure 3-3. Maximum tsunami momentum flux (m^3/s^2) at observation sites arranged from north (left) to south (right). Thio = Thio (2019).

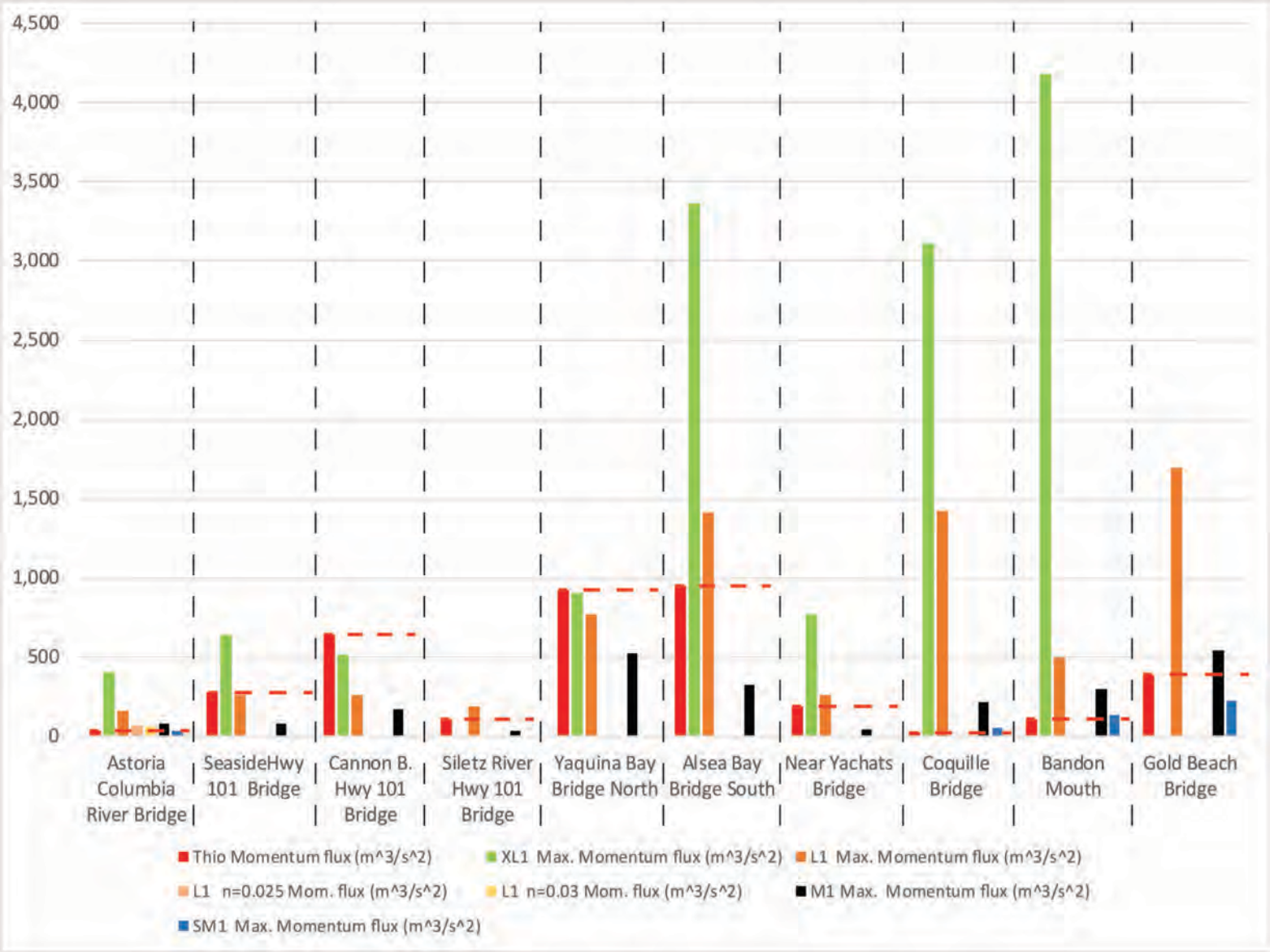

Offshore wave height data follow a pattern somewhat different from the open coast and inland. AECOM wave amplitudes at 100 m depth for a 2,475-yr exceedance scenario (Thio, 2017) closely resemble XL1 (**Figure 3-4**), while the AECOM 1,000-yr exceedances (Thio, 2019) resemble L1 in most of the coast (**Figure 3-5**). Exceptions are where the DOGAMI wave heights are strongly amplified over both AECOM wave heights by Stonewall Bank and Rogue Canyon (**Figure 3-4** and **Figure 3-5**). A submarine bank offshore of Seaside appears to strongly amplify the AECOM 2,475-yr amplitudes relative to DOGAMI scenarios (**Figure 3-4**) but that amplification is absent from AECOM 1,000-yr amplitudes (**Figure 3-5**).

It is hard to understand how 1,000-yr wave heights approximating L1 at 100 m depth (**Figure 3-5**) can produce inundation barely reaching SM1 at the open coast at Gold Beach and Bandon (**Table 3-2**). Unfortunately, analysis of this issue and the obvious effects of Stonewall Bank and Rogue Canyon is hampered by lack of access to the entire offshore DEM of Thio (2019). Analysis of vertical deformation of Thio's CSZ sources, particularly the 10 used for simulations of inundation would also be helpful, but those data are not available at this writing.

Figure 3-4. Tsunami wave amplitudes of AECOM (Thio, 2017) at 100 m water depth for 2,475-yr exceedance (black dash line) compared to the XL1 (blue line) and L1 (red line) tsunami wave heights of DOGAMI. The gray shading defines the ±20 percent criteria of the 2,475-yr amplitudes recommended by the ASCE (American Society of Civil Engineers) as the threshold for adopting an alternative tsunami scenario for estimating inundation and current force levels under ASCE (Chock, 2016) guidance for construction of critical and essential facilities in a tsunami inundation zone.

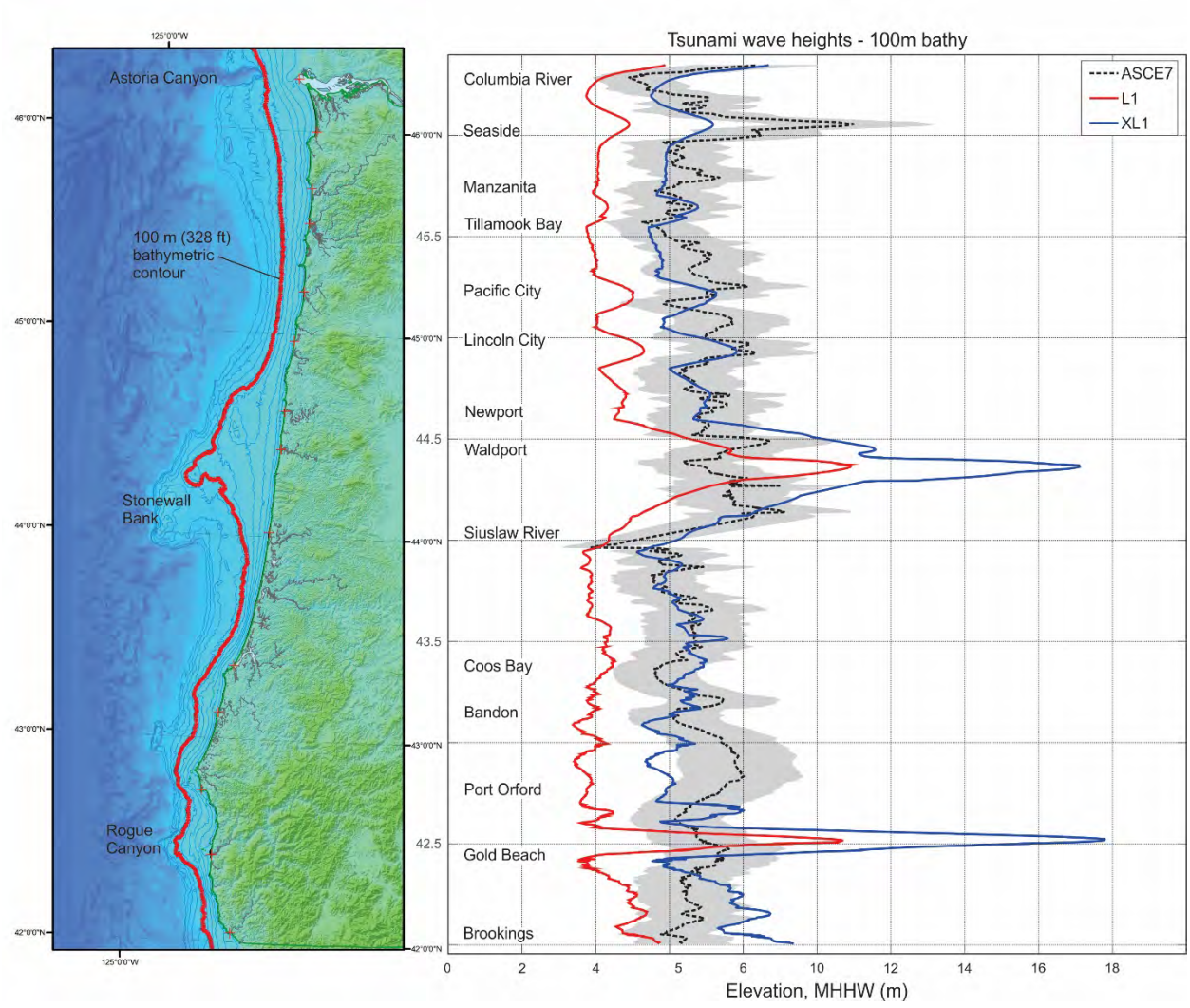

Figure 3-5. Tsunami wave heights above mean higher high water of AECOM (Thio, 2019) at the 100 m water depth for a 1,000-yr exceedance compared to the DOGAMI (Priest and others, 2013) wave heights for XXL1, XL1, L1, and M1 scenarios.

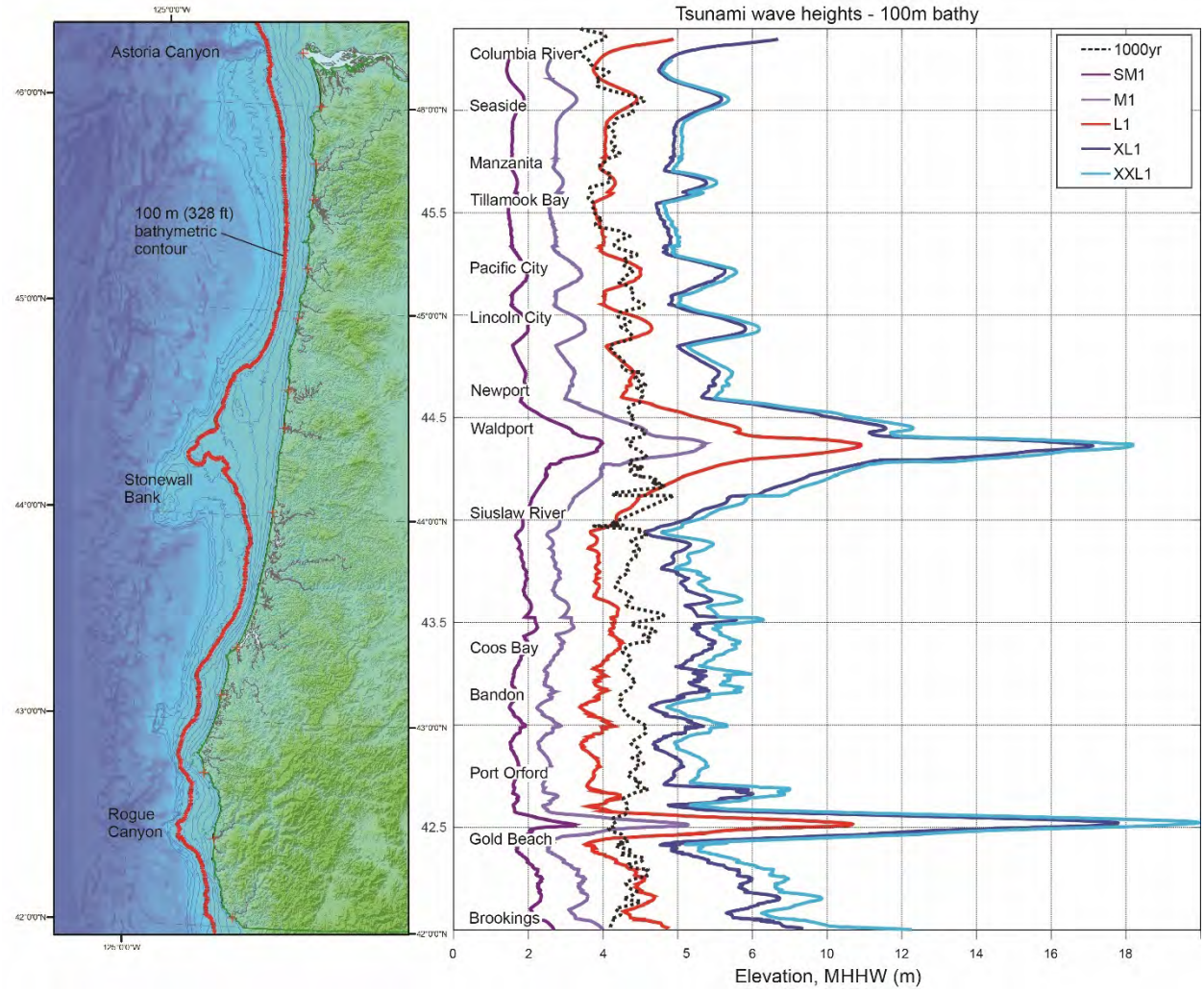

4.0 DISCUSSION

4.1 Probabilistic Expectations for Match of DOGAMI Scenarios to 1,000-yr and 2,475-yr Exceedance Events of AECOM

A useful starting point for comparison of the DOGAMI and AECOM (Thio, 2017, 2019) approaches is to try to understand which DOGAMI tsunami scenarios best correspond to 1,000-yr and 2,475-yr exceedance events in a PTHA. **Table 4-1** illustrates what a Cascadia PTHA might look like using the DOGAMI approach applied to the Coquille Estuary at Bandon. **Table 4-1** should be considered only a quasi-probabilistic PTHA for discussion, because the table is far from a complete analysis that would include all uncertainties. This exercise focuses only on the main source of uncertainty for 1,000-yr and 2,475-yr exceedance, the most critical CSZ earthquake source characteristics, slip magnitude and distribution. In this respect, the approach follows the AECOM PTHA, because both use the Goldfinger and others (2012) CSZ rupture lengths as the most important factor in their PTHAs for the CSZ tsunamis (i.e., at the base of the equivalent logic trees).

The quasi-probabilistic PTHA is modified from the PTHA of González and others (2014) for Crescent City, using slightly different partial rupture scenarios and without incorporation of tidal uncertainties, which have little effect on all but the smallest potential CSZ tsunamis. Momentum flux data are not compared, because these data are not extracted from enough DOGAMI scenarios in the Bandon area to construct meaningful hazard curves. We chose the Bandon area because that is the only region of the Oregon coast where Witter and others (2011, 2013) simulated tsunamis from all scenarios of their logic tree (see **Figure 2-3**). Besides the original 19 events emphasized in **Figure 2-3**, we include in **Table 4-1** partial rupture scenarios to account for the segment B (4 events), C (8 events), and D (10 events) zones defined in Goldfinger and others (2012). For this exercise, the B and C velocity and flow depth data are all set equal to equivalent SM values by assuming that the peak slip deficits released for all are ~300 yrs of plate convergence. This slip deficit approximates slip at this latitude assigned by Scholz (2014) to segments B and C from seismic energy balance considerations. This slip deficit is also near the threshold to cause CSZ tsunamis to reach Bradley Lake, which some of them must have done according to the Witter and others (2012) and Priest and others (2017, 2018) analyses. Peak slip deficit for the D rupture zone of **Figure 2-2** is set equal to 200 years as by González and others (2014) and is referred to as scenario D200 in figures and tables. Maximum values of flow depth and current velocity at Bandon are unpublished data extracted from simulations of scenario D200 by Priest and others (2014).

Addition of the segment B, C, and D events overshoots the available 10,000 yrs of slip deficit, as the Witter and others (2011, 2013) approach balances this 10,000 yrs of potential slip deficit using only the 19 segment A events of **Table 4-1**. Nevertheless, this quasi-probabilistic PTHA is a useful starting point for comparing DOGAMI and AECOM tsunami data. Adaptation of the Witter and others (2011, 2013) slip balance approach to a PTHA would necessitate incorporation of seismic energy balance considerations such as those of Scholz (2014) which demand a much larger southerly decrease of slip in the 19 segment A events than assumed by Witter and others (2011, 2013).

The quasi-probabilistic PTHA is probably least useful at inland sites where comparisons to AECOM are most affected by the lower bottom friction of the DOGAMI simulations and any differences in DEMs. Obviously, DOGAMI values will diverge from AECOM more and more with distance inland, regardless of similarity of the sources and other factors.

With these considerations in mind, we developed new hazard curves (**Figure 4-1** through **Figure 4-4**) for CSZ tsunamis at Bandon. Following the approach of González and others (2009), we assume that the

probability of CSZ earthquakes can be described as a Poisson process with mean annual rates of occurrence small enough that they approximate annual probabilities. This assumption allows us to develop hazard curves by simply adding the annual recurrences. The probability of exceeding a certain flow depth or velocity of any scenario is then just the mean annual recurrence of that scenario added to the cumulative recurrences of all smaller scenarios. The hazard curves of **Figure 4-1** through **Figure 4-4** (based on data defined in **Table 4-2** through **Table 4-5**) illustrate that the 1,000-yr exceedance for maximum flow depth and velocity would approximate the M3 scenario. There is insufficient momentum flux data available to produce similar hazard curves, but because recurrences are the same, the results should be similar, particularly for velocity, as momentum flux is directly proportional to the square of velocity.

The hazard curves (**Figure 4-1** through **Figure 4-4**) for the Bandon area illustrate that the 1,000-yr exceedance velocities and flow depths best match the M3 scenario, while 2,475-yr exceedances approximate the L2 scenario. If one were using only the published coast-wide DOGAMI data of Priest and others (2013) (SM1, M1, L1, XL1, and XXL1) for estimates of tsunami hazard force, velocity, and flow depth, the M1 has values for these parameters quite close to the M3 scenario, so would be a reasonable conservative choice for the 1,000-yr exceedance. The L1 scenario most closely resembles the L2 scenario and would be a conservative choice for the 2,475-exceedance. This finding is not completely consistent with comparisons of DOGAMI to AECOM data for either the 2,475-yr exceedance wave amplitudes offshore (**Figure 3-4**) or the 1,000-yr exceedances on the coast (**Figure 3-1** through **Figure 3-3**, **Table 3-2** and **Table 3-3**). For example, the AECOM 2,475-yr wave amplitudes at 100 m depth offshore most closely resemble the XL1 scenario rather than the L1 or M1 scenarios. There are numerous exceptions most likely caused by bathymetric data differing between the two (**Figure 3-4**).

Another example of this mismatch is the anomalously low AECOM (Thio, 2019) 1,000-yr flow depths and resulting inundation on the south coast relative to DOGAMI. AECOM 1,000-yr exceedance flow depths and velocities should decrease relative to 1,000-yr DOGAMI values inland because of the incorporation of bottom friction in the AECOM simulations, and this is consistent with displacement of AECOM values below the M1 values or hazard curves for the bridge site 5 km upstream from the mouth of the Coquille River (**Figure 4-1** and **Figure 4-2)**. However, open coastal values of AECOM should not be as strongly displaced below the DOGAMI M1 values, because at the open coast frictional effects on tsunami flow are much lower compared with inland sites. Nevertheless, at the Coquille River mouth (**Figure 4-3** and **Figure 4-4**) and at Gold Beach the AECOM 1,000-yr flow depths closely resemble SM1, even though velocities resemble the M1 scenario (**Figure 3-1** through **Figure 3-3**, **Table 3-2** and **Table 3-3**).

Resolving why the AECOM flow depths seem anomalously low relative to the DOGAMI PTHA on the south coast is difficult without more information on the 10 CSZ sources of Thio (2019), particularly spatial data on slip and vertical coseismic deformation patterns. We can speculate that at the 1,000-yr exceedance probability the AECOM PTHA is more heavily influenced by the small partial CSZ ruptures that become a progressively larger part of the model space (and the paleoseismic record of **Figure 2-2**) the farther south one goes on the CSZ. Seismic energy balance calculations of Scholz (2014) account for the partial ruptures by north-to-south taper of full-margin slip by 60 percent from Washington to the southern Oregon, whereas Witter and others (2011, 2013) taper XL, L, and M scenarios by only 8, 12, and 14 percent, respectively. Because flow depths at the open coast are directly proportional to peak slip for any given slip distribution (Priest and others, 2009, 2010), incorporating the Scholz taper would shift the DOGAMI flow depth hazard curves toward the Thio (2019) values in **Figure 4-1** and **Figure 4-3**, but not in any simple fashion. Reducing slip on the full-margin rupture scenarios at Bandon with the Scholz taper would also necessitate adding slip to the B, C, and D rupture scenarios of **Table 4-1**, fundamentally changing the

hazard curves. An entirely new PTHA incorporating this modification would be needed to fully explore the issue.

AECOM (Thio, 2019) 1,000-yr velocities and flow depths at the open coast and offshore are generally larger on the central and north coast than the ~M1 values predicted by the quasi-probabilistic PTHA. At bridge sites nearest the coastal shoreline on the north coast, Yachats, Cannon Beach, and Seaside, DOGAMI flow depths resembling the AECOM 1,000-yr values are XL1, XL1, an L1, respectively (**Figure 3-1** through **Figure 3-3**, **Table 3-2** and **Table 3-3**). Velocity matches are M1 for Seaside, L1 for Yachats, and XXL1 for Cannon Beach, although the Yachats comparisons are problematic owing to the poor DEM of the AECOM simulations in that locality.

Finally, we do not fully understand how the incorporation of Thio's (2019) estimates of aleatory error into the offshore wave heights might contribute to the anomalously low south coast flow depths or generally higher than expected wave heights offshore. In his words from a 2019 written communication,

> When we determine the offshore exceedance amplitudes using the Green's function summation, we apply an aleatory term to every offshore amplitude. So rather than use the maximum amplitude of every scenario at face value, we regard them as the mean of a normal distribution, which represent the error in the model (algorithm, bathymetry, etc.). The contribution of this term to the hazard increases as the probability level decreases (or the return period increases). In fact, at return periods beyond the longest return period considered in the analysis, the hazard will keep growing because there is always a small chance that the observed wave amplitude is larger than the modeled wave amplitude. This is an integral and desirable element of the probabilistic analysis. Another reason may be the higher sigma-magnitude scenarios, although the largest ones are well beyond the 2500-year return period.

Furthermore, the increase in aleatory error apparently accounts for inherently large errors in inundation models, which are probably due to mismatches to natural bottom friction as well as uncertainty in the DEMs (Thio, 2019, written communication).

Table 4-1. Quasi-probabilistic PTHA for Bandon area based on DOGAMI flow depths, velocities, and momentum flux. Data are from Witter and others (2011), Priest and others (2013), and unpublished data of Priest and others (2014) for their D200 scenario. This approach adds B, C, and D ruptures (22 events) to logic tree of Figure 4. Nc/10 ka = annual probability of any CSZ event; No. = number; No./10 ka = annual probability each segment; rec. = recurrence; cond. prob. = conditional probability (logic tree weight); max. = maximum; vel. = velocity.

Total No. of CSZ Events in 10 ka	Nc/ 10 ka	Rec. (yrs)	Segment	Size	No.	No./ 10 ka	Rec. (yrs)	Scenario	Rupture Model	Cond. Prob. P	Mean Scenario Rate	Mean Rec. (yrs)	Max. Vel. (m/s) Bridge	Max. Flow Depth (m) Bridge	Max. Vel. (m/s) Mouth	Max. Flow Depth (m) Mouth
41	0.0041	244	A	XXL	0.5	0.00005	20 ka	XXL1	Splay	0.8	0.00004	25,000	10.1	28.6	11.0	29.1
								XXL2	Shallow	0.1	0.000005	200,000	8.3	27.1	12.1	26.2
								XXL3	Deep	0.1	0.000005	200,000	9.1	28.3	11.5	26.8
			A	XL	0.5	0.00005	20 ka	XL1	Splay	0.8	0.00004	25,000	10.6	27.7	12.4	27.2
								XL2	Shallow	0.1	0.000005	200,000	10.5	24.5	9.7	24.7
								XL3	Deep	0.1	0.000005	200,000	9.3	27.7	10.9	25.2
			A	L	3	0.0003	3.3 ka	L1	Splay	0.8	0.00024	4,167	8.9	18.6	8.0	20.9
								L2	Shallow	0.1	0.00003	33,333	8.2	15.0	7.8	19.1
								L3	Deep	0.1	0.00003	33,333	8.1	16.2	8.1	19.5
			A	M	10	0.0010	1 ka	M1	Splay	0.6	0.00060	1,667	5.0	8.7	6.6	16.5
								M2	Shallow	0.2	0.00020	5,000	4.3	7.9	5.7	15.3
								M3	Deep	0.2	0.00020	5,000	4.6	8.1	6.1	15.6
			A	SM	5	0.0005	2 ka	SM1	Splay	0.4	0.00020	5,000	2.7	7.1	4.5	13.6
								SM2	Shallow	0.3	0.00015	6,667	2.4	7.0	4.5	12.7
								SM3	Deep	0.3	0.00015	6,667	2.4	6.9	4.2	12.9
			B	B*	4	0.0004	2.5 ka	B1	Splay	0.5	0.0002	5,000	2.7	7.1	4.5	13.6
								B2	Shallow	0.2	0.00008	12,500	2.4	7.0	4.5	12.7
								B3	Deep	0.3	0.00012	8,333	2.4	6.9	4.2	12.9
			C	C*	8	0.0008	1.125 ka	C1	Splay	0.4	0.00032	3,125	2.7	7.1	4.5	13.6
								C2	Shallow	0.3	0.00024	4,167	2.4	7.0	4.5	12.7
								C3	Deep	0.3	0.00024	4,167	2.4	6.9	4.2	12.9
			D	D*	10	0.001	1.0 ka	D200	Shallow	1.0	1.0000	1,000	0.1	5.6	0.6	9.0

*Flow depths and velocities for B, C, and D ruptures calculated by assuming that they will have the mean slip deficit release Scholz (2014) at this latitude of the CSZ, ~300 yrs which equals the slip deficit of the SM scenario of Witter and others (2011, 2013).

Figure 4-1. Hazard curve for maximum flow depth data of DOGAMI at the Coquille River bridge, Bandon. Red triangle labeled Thio = 1,000-yr exceedance value of AECOM (Thio, 2019). Labels on data points are scenarios of Table 4-1.

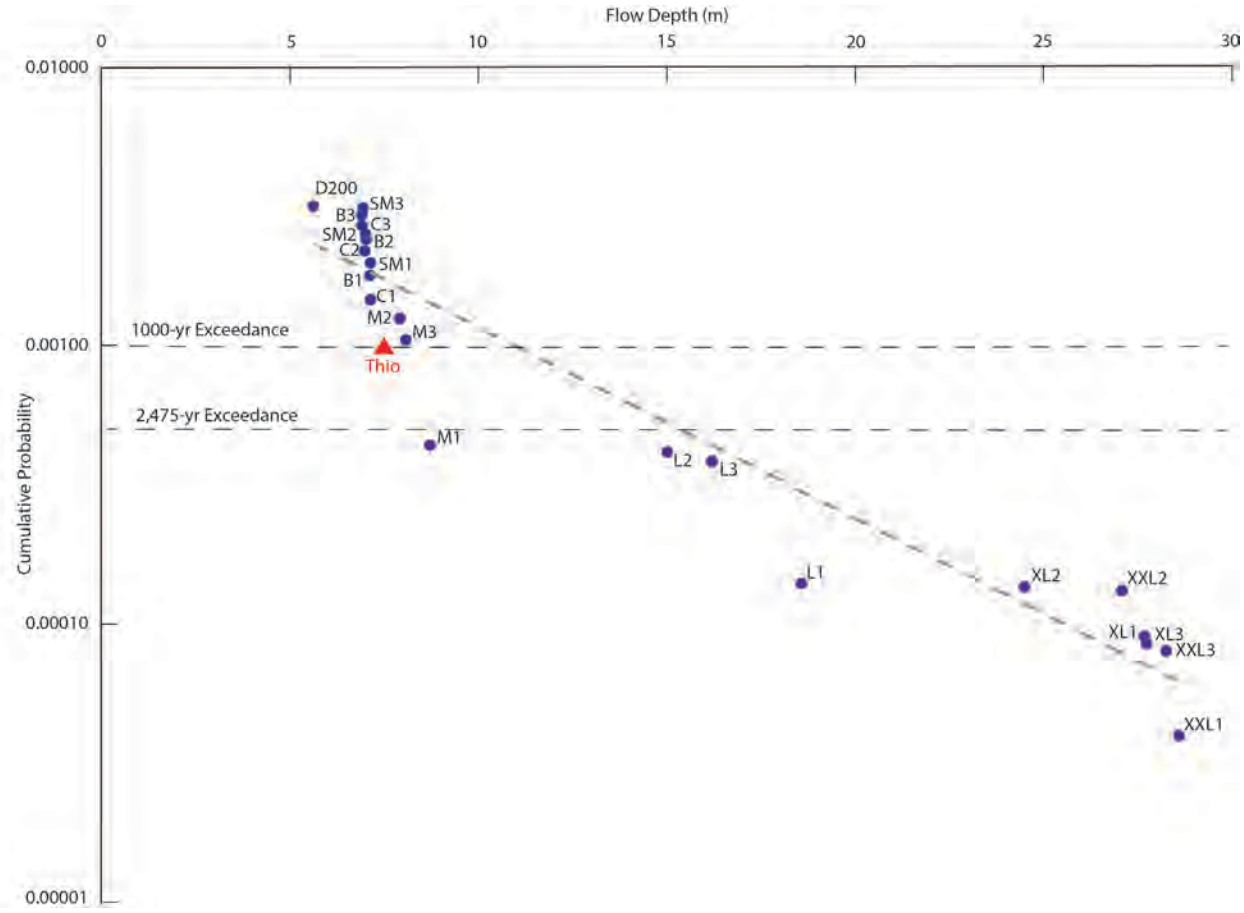

Table 4-2. Cumulative probability data for maximum flow depth hazard curve of Figure 4-1 for the Coquille River bridge, Bandon, based on DOGAMI data from scenarios of Table 4-1. DOGAMI scenarios with coast-wide data are in boldface. Max. = maximum; yrs = years; Recurr. = recurrence; Ann. = annual; Cum. P = cumulative probability.

Scenario	Max. Flow Depth (m)	P = 1/Ann. Recurr.	Ann. Recurr. (yrs)	Cum. P	Exceedance (yrs)
D200	5.6	0.00100	1,000	0.00314	318
SM3	6.9	0.00015	6,667	0.00299	334
B3	6.9	0.00012	8,333	0.00287	348
C3	6.9	0.00024	4,167	0.00263	380
SM2	7	0.00015	6,667	0.00248	403
B2	7	0.00008	12,500	0.00240	417
C2	7	0.00024	4,167	0.00216	463
SM1	**7.1**	**0.00020**	**5,000**	**0.00196**	**510**
B1	7.1	0.00020	5,000	0.00176	568
C1	7.1	0.00032	3,125	0.00144	694
M2	7.9	0.00020	5,000	0.00124	806
M3	8.1	0.00020	5,000	0.00104	962
M1	**8.7**	**0.00060**	**1,667**	**0.00044**	**2,273**
L2	15	0.00003	33,333	0.00041	2,439
L3	16.2	0.00003	33,333	0.00038	2,632
L1	**18.6**	**0.00024**	**4,167**	**0.00014**	**7,143**
XL2	24.5	0.00001	200,000	0.00014	7,407
XXL2	27.1	0.00001	200,000	0.00013	7,692
XL1	**27.7**	**0.00004**	**25,000**	**0.00009**	**11,111**
XL3	27.7	0.00001	200,000	0.00009	11,765
XXL3	28.3	0.00001	200,000	0.00008	12,500
XXL1	**28.6**	**0.00004**	**25,000**	**0.00004**	**25,000**

Figure 4-2. Hazard curve for maximum velocity data of DOGAMI at Coquille River bridge, Bandon. Red triangle labeled Thio = 1,000-yr exceedance value of AECOM (Thio, 2019). Labels on data points are scenarios of Table 4-1.

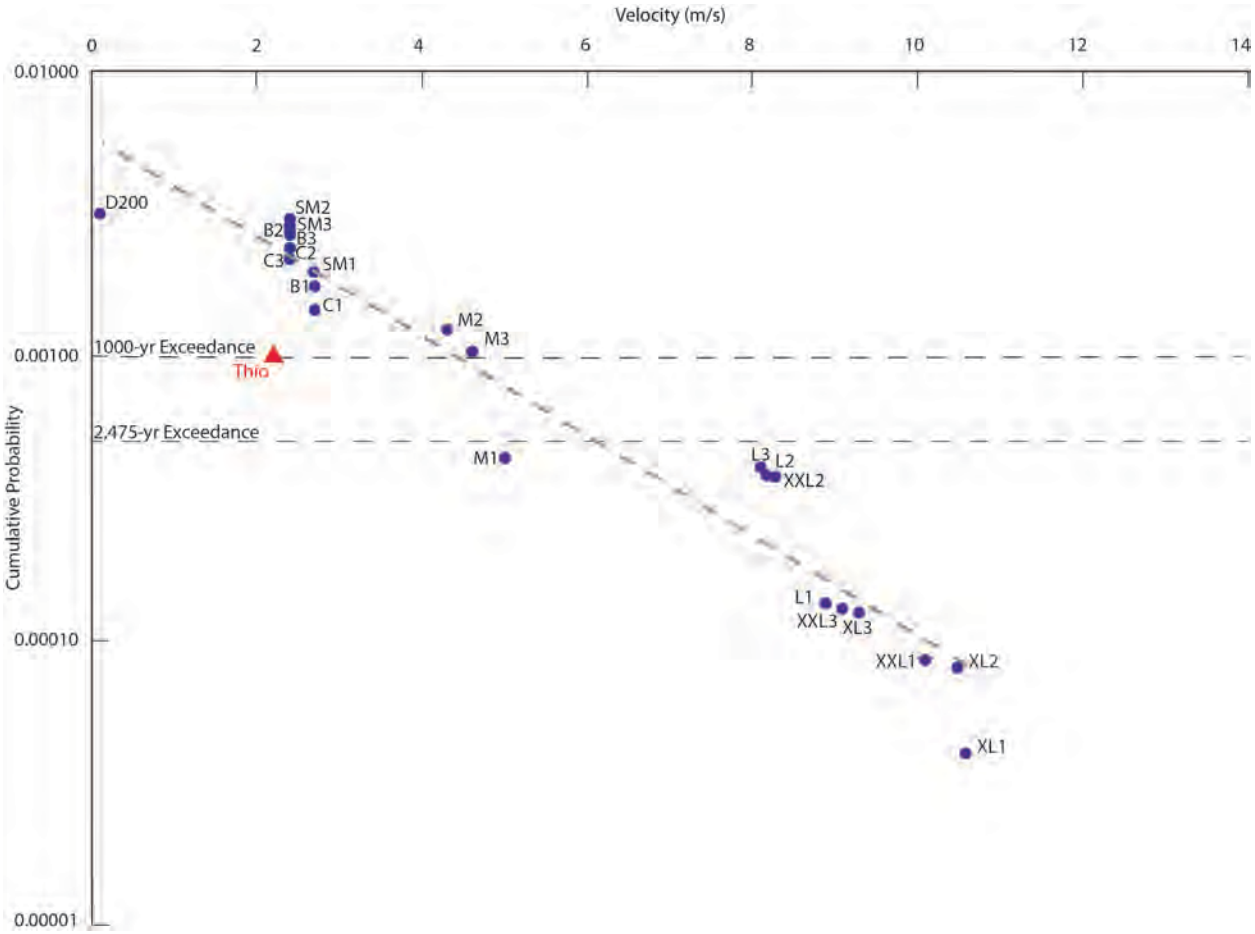

Table 4-3. Cumulative probability data for maximum velocity hazard curve of Figure 4-2 for the Coquille River bridge, Bandon, based on DOGAMI data from scenarios of Table 4-1 and Appendix B, Table B-1. DOGAMI scenarios with coast-wide data are in boldface. Max. = maximum; yrs = years; Recurr. = recurrence; Ann. = annual; Cum. P = cumulative probability.

Scenario	Max. Velocity (m/s)	P = 1/Ann. Recurr.	Ann. Recurr. (yrs)	Cum. P	Exceedance (yrs)
D200	0.1	0.00100	1,000	0.00314	318
SM2	2.4	0.00015	6,667	0.00299	334
SM3	2.4	0.00015	6,667	0.00284	352
B2	2.4	0.00008	12,500	0.00276	362
B3	2.4	0.00012	8,333	0.00264	379
C2	2.4	0.00024	4,167	0.00240	417
C3	2.4	0.00024	4,167	0.00216	463
SM1	**2.7**	**0.00020**	**5,000**	**0.00196**	**510**
B1	2.7	0.00020	5,000	0.00176	568
C1	2.7	0.00032	3,125	0.00144	694
M2	4.3	0.00020	5,000	0.00124	806
M3	4.6	0.00020	5,000	0.00104	962
M1	**5**	**0.00060**	**1,667**	**0.00044**	**2,273**
L3	8.1	0.00003	33,333	0.00041	2,439
L2	8.2	0.00003	33,333	0.00038	2,632
XXL2	8.3	0.00001	200,000	0.00038	2,667
L1	**8.9**	**0.00024**	**4,167**	**0.00014**	**7,407**
XXL3	9.1	0.00001	200,000	0.00013	7,692
XL3	9.3	0.00001	200,000	0.00013	8,000
XXL1	**10.1**	**0.00004**	**25,000**	**0.00009**	**11,765**
XL2	10.5	0.00001	200,000	0.00008	12,500
XL1	**10.6**	**0.00004**	**25,000**	**0.00004**	**25,000**

Figure 4-3. Hazard curve for maximum flow depth data of DOGAMI at Coquille River mouth, Bandon. Red triangle labeled Thio = 1,000-yr exceedance value of AECOM (Thio, 2019). Labels on data points are scenarios of Table 4-1.

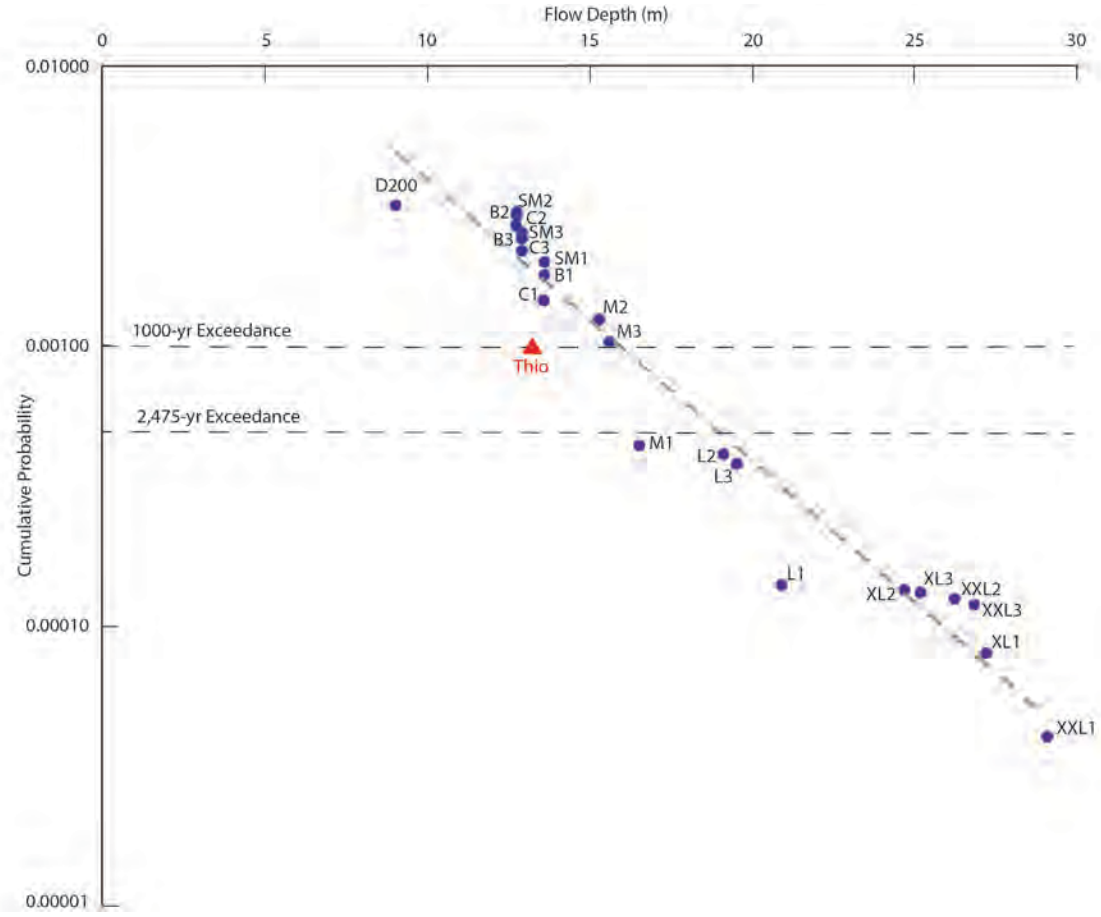

Table 4-4. Cumulative probability data for maximum flow depth hazard curve of Figure 4-3 for the Coquille River mouth, Bandon, based on DOGAMI data from scenarios of Table 4-1 and Appendix B, Table B-1. DOGAMI scenarios with coast-wide data are in boldface. Max. = maximum; yrs = years; Recurr. = recurrence; Ann. = annual; Cum. P = cumulative probability.

Scenario	Flow Depth (m)	P = 1/Ann. Recurr.	Ann. Recurr. (yrs)	Cum. P	Exceedance (yrs)
D200	9.0	0.001000	1,000	0.00314	318
SM2	12.7	0.00015	6,667	0.00299	334
B2	12.7	0.00008	12,500	0.00291	344
C2	12.7	0.000240	4,167	0.00267	375
SM3	12.9	0.00015	6,667	0.00252	397
B3	12.9	0.00012	8,333	0.00240	417
C3	12.9	0.000240	4,167	0.00216	463
SM1	**13.6**	**0.0002**	**5,000**	**0.00196**	**510**
B1	13.6	0.0002	5,000	0.00176	568
C1	13.6	0.000320	3,125	0.00144	694
M2	15.3	0.0002	5,000	0.00124	806
M3	15.6	0.0002	5,000	0.00104	962
M1	**16.5**	**0.0006**	**1,667**	**0.00044**	**2,273**
L2	19.1	0.00003	33,333	0.00041	2,439
L3	19.5	0.00003	33,333	0.00038	2,632
L1	**20.9**	**0.00024**	**4,167**	**0.00014**	**7,143**
XL2	24.7	0.000005	200,000	0.00014	7,407
XL3	25.2	0.000005	200,000	0.00013	7,692
XXL2	26.2	0.000005	200,000	0.00013	8,000
XXL3	26.8	0.000005	200,000	0.00012	8,333
XL1	**27.2**	**0.00004**	**25,000**	**0.00008**	**12,500**
XXL1	**29.1**	**0.00004**	**25,000**	**0.00004**	**25,000**

Figure 4-4. Hazard curve for DOGAMI maximum velocity data at Coquille River mouth, Bandon. Red triangle labeled Thio = 1,000-yr exceedance value of AECOM (Thio, 2019). Labels on data points are scenarios of Table 4-1.

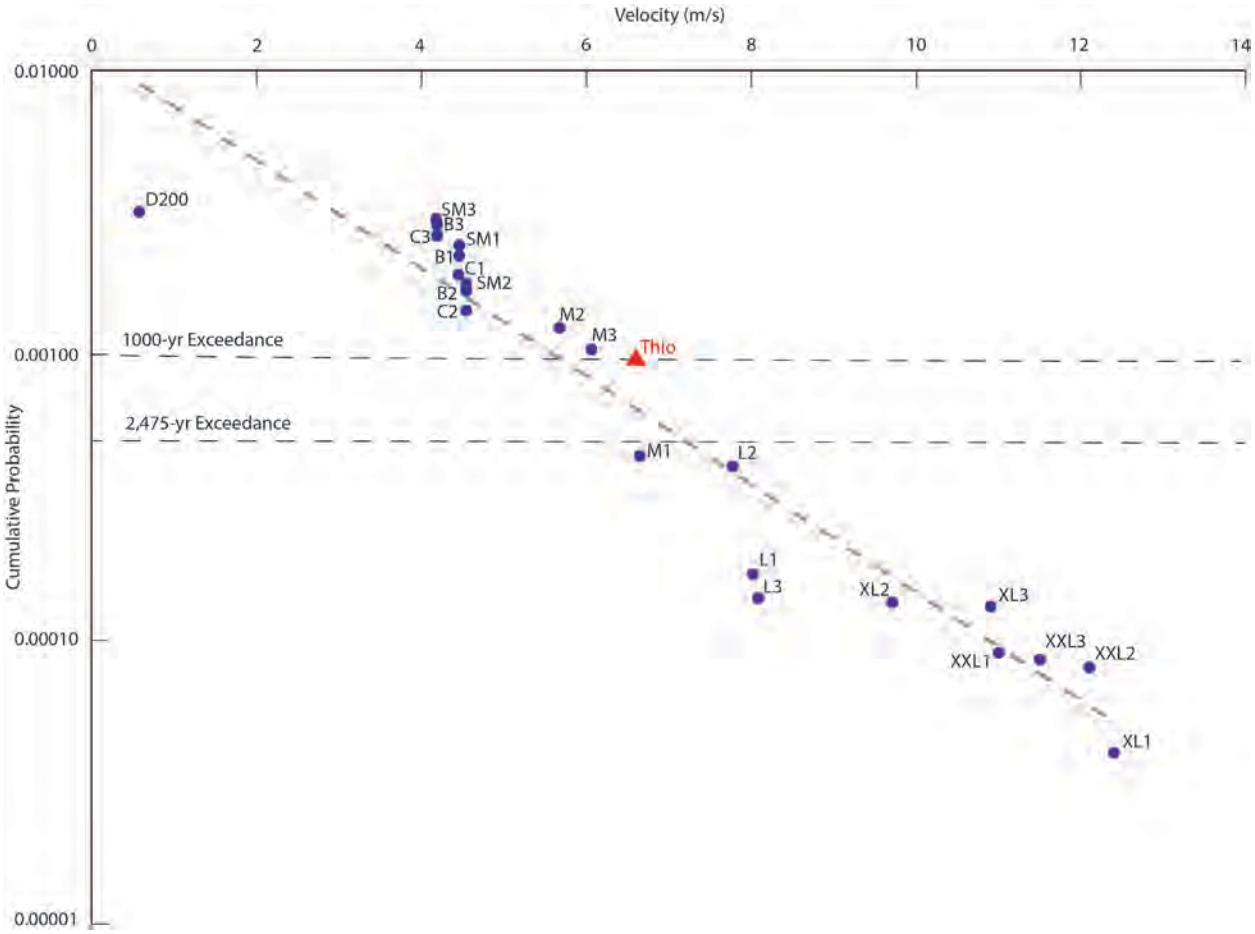

Table 4-5. Cumulative probability data for maximum velocity hazard curve of Figure 4-4 for the Coquille River mouth, Bandon, based on DOGAMI data from scenarios of Table 4-1 and Appendix B, Table B-1. DOGAMI scenarios with coast-wide data are in boldface. Max. = maximum; yrs = years; Recurr. = recurrence; Ann. = annual; Cum. P = cumulative probability.

Scenario	Max. Velocity (m/s)	P = 1/Ann. Recurr.	Ann. Recurr. (yrs)	Cum. P	Exceedance (yrs)
D200	0.6	0.001000	1,000	0.00314	318
SM3	4.2	0.00015	6,667	0.00299	334
B3	4.2	0.00012	8,333	0.00287	348
C3	4.2	0.000240	4,167	0.00263	380
SM1	**4.5**	**0.0002**	**5,000**	**0.00243**	**412**
B1	4.5	0.0002	5,000	0.00223	448
C1	4.5	0.000320	3,125	0.00191	524
SM2	4.5	0.00015	6,667	0.00176	568
B2	4.5	0.00008	12,500	0.00168	595
C2	4.5	0.000240	4,167	0.00144	694
M2	5.7	0.0002	5,000	0.00124	806
M3	6.1	0.0002	5,000	0.00104	962
M1	**6.6**	**0.0006**	**1,667**	**0.00044**	**2,273**
L2	7.8	0.00003	33,333	0.00041	2,439
L1	**8.0**	**0.00024**	**4,167**	**0.00017**	**5,882**
L3	8.1	0.00003	33,333	0.00014	7,143
XL2	9.7	0.000005	200,000	0.00014	7,407
XL3	10.9	0.000005	200,000	0.00013	7,692
XXL1	**11.0**	**0.00004**	**25,000**	**0.00009**	**11,111**
XXL3	11.5	0.000005	200,000	0.00009	11,765
XXL2	12.1	0.000005	200,000	0.00008	12,500
XL1	**12.4**	**0.00004**	**25,000**	**0.00004**	**25,000**

4.2 Extreme CSZ Earthquake Sources of AECOM Relative to DOGAMI

One possible reason for larger than expected amplitudes offshore and, for the northern and central coast, flow depths and velocities onshore of AECOM (Thio, 2017, 2019) may be choosing anomalously large CSZ earthquakes relative to what is thought reasonable by the DOGAMI (Witter and others, 2011, 2013). For example, CSZ events developed by Thio (2017, his Table E-2) include 36 events (out of 86, i.e. 42 percent) having mean slip greater than the 22-m maximum allowed by DOGAMI. The largest 18 (21 percent) of AECOM events have mean slip between 59 and 76 m, as large or larger than the largest known asperity slip of ~60 m identified in the Tohoku-oki earthquake of 2011 (Wang and others, 2018). These large mean slip values are amplified by a factor of 2.2 in the asperity slip patches used in the AECOM approach. This means that 42 percent of the sources have individual asperities releasing between ~1,500 and 4,500 yrs of convergence on the CSZ, assuming a typical convergence rate of 37 mm/yr in central Oregon. Assuming an area of the CSZ megathrust is fully locked and accumulating strain in an "asperity," the total available asperity slip deficit over the last 10,000 yrs is 370 m at 37 mm/yr, Therefore, 42 percent of the AECOM asperities are each releasing 15 to 45 percent of the last 10,000 yrs of CSZ convergence. However, it is difficult to say whether these large events have any influence on the AECOM 1,000-yr or 2,475-yr exceedances, because recurrences are not listed in the reports. Obviously, if these large events have recurrence greatly exceeding 1,000–2,475 yrs, they would have no effect.

We can assess how reasonable the extreme AECOM (Thio, 2017, 2019) asperity sources are by estimating the available slip for large events after subtracting the minimum slip to account for turbidites and paleotsunami deposits over the last 10,000 yrs. We know from the 10,000 yrs of turbidite data of Goldfinger and others (2012) that there have been 19 full-margin and ~22 partial CSZ ruptures that must be accounted for with the ~370 m of CSZ convergence. In the last ~5,000 yrs, twelve of these events required a minimum of 8–13 m of peak slip to overtop a barrier at Bradley Lake, a total of >96–156 m, with the larger value being more likely than the smaller (Witter and others, 2012; Priest and others, 2017, 2018). We know less about the history between 5,000 and 10,000 yrs, but relative turbidite mass data of **Figure 2-7** give us some clues: (1) there were two outsized earthquakes with slip likely much greater than the 8–13 m of Bradley, and (2) there were four smaller margin-wide ruptures similar in mass to nine margin-wide events that caused tsunamis to overtop the barrier at Bradley Lake (total of ≥32–52 m). One must also find enough slip for 22 partial ruptures in 10,000 yrs and the three full-margin ruptures prior to 5,000 yrs that may have been smaller than the Bradley minima. We know from Priest and others (2017) that at least 1.7–2.7 m of slip is needed to leave a turbidite record, so these events must have total slip >42.5–67.5 m. The sum of all minima for the last 10,000 yrs is 170.5–275.5 m, leaving a maximum of ~84.5 to 189.5 m of slip for the two outsized events. At 37 mm/yr, this would amount to an absolute upper limit of ~2,300 to 5,000 yrs of slip deficit for these two largest events (5 percent of the 41 total events) in southernmost Cascadia (segment D of **Figure 2-2**), or a mean of ~1,150–2,500 yrs per event, much less than the significantly larger number of outsized CSZ events of AECOM. Nevertheless, these extreme AECOM slip events cannot be entirely ruled out based on slip budget over the 10,000 years of turbidite events, because it is unlikely that any subduction zone is 100 percent efficient at releasing slip, even in large earthquakes. Thus, it is likely that there is always repository of unreleased slip for any given time interval that could be released in such extreme events.

4.3 Problems with Use by AECOM of Global Seismic Data to Estimate CSZ Earthquake Size and Slip

It is possible that the AECOM (Thio, 2017, 2019) use of regressions through global seismic data to estimate CSZ earthquake size and slip may contribute to the mismatch with the quasi-probabilistic PTHA. In Tréhu's (2016) review of CSZ earthquake size estimates using seismic energy balance over the last 10,000 yrs of CSZ events, she concluded that these methods do not match global data unless the estimates are modified. The unmodified CSZ data of Tréhu (2016) and Scholz (2014) correlating total rupture area and mean slip to seismic moment matched global predictions for asperities rather than global data for total rupture area and mean slip. The most successful modification in her analysis was to expand the geologically estimated CSZ rupture areas of Scholz (2014) and Tréhu (2016) by the global ratio of 4.17 for mean slip area to asperity area from Skarlatoudis and others (2016). Tréhu (2016, p. 910) noted that this artificial expansion of her CSZ widths "leads to fault widths that may be incompatible with physical controls on the depth extent of seismogenic rupture. Including possible biases in the modern [global] estimates due to smoothing and allowing a few percent creep, however, could mitigate this width problem."

The root of the problem is probably the fact that global earthquake observations are dominated by data from subduction zones unlike the CSZ. The CSZ has a much younger, hotter subducting oceanic plate with a correspondingly narrower locked zone compared to most other subduction zones. The seismic slip is therefore concentrated in a zone with width more akin to the asperities in other subduction zones.

We conclude that if global seismic data are used for estimates of mean CSZ slip from CSZ rupture areas, the regression equations of Skarlatoudis and others (2016) for asperity data are more appropriate than regressions for mean slip. The AECOM analyses were likely affected by this mismatch, causing mean slip to be systematically underestimated from rupture area data of the CSZ. This underestimate is largest for the narrowest widths of AECOM CSZ sources that account for 75 percent of the AECOM logic tree weight for full-length ruptures and 100 percent of partial ruptures (i.e., 1 cm/yr locking zone and midpoint of fully locked zone and 1 cm/yr locking, **Figure 2-8**).

This underestimation of mean slip by AECOM would be particularly severe for the small, narrow ruptures like those of segments C and D (**Figure 2-2**). This factor might be part of the reason that the Thio (2019) flow depths and inundations are so much smaller than expected in southern Cascadia, where segments C and D are frequent events in any PTHA.

4.4 Effect of Excluding Distant Tsunami Scenarios from the Quasi-probabilistic PTHA

It is also worth asking whether the quasi-probabilistic PTHA and associated hazard curves (**Table 4-2** and **Table 4-3**) would lead to different 1,000-yr or 2,475-yr events (i.e., M1 or L1) if distant tsunami sources or very rare extreme sources (e.g., with slip deficits >>1,200 yrs) were added, since these are included in the AECOM analyses. The largest distant tsunami would likely be from the Gulf of Alaska and would have flow depths generally somewhat lower than the SM scenario according to simulations of Priest and others (2009, 2010) and Witter and others (2011). Recurrence of such extreme Gulf of Alaska tsunamis is on the order of several centuries (Nishenko, 1991), so adding these data would not significantly alter the hazard curves. Likewise, adding very rare events larger than XXL would not change the 1,000-yr or 2,475-yr exceedance results.

4.5 Using a PTHA Versus Individual Tsunami Simulations for Engineering Design

Finally, we ask whether, for engineering purposes, obtaining a precise probabilistic answer to velocity, flow depth, and momentum flux is a better approach than simply picking a single tsunami scenario that approximates the target exceedance level. For example, in the hazard curve of **Figure 4-4**, the regression (dashed gray line) can provide a precise value of velocity for any exceedance level; however, picking a single scenario can provide not only the velocity but also a time history of velocity magnitude, direction, and duration at all computational points. Each time history or maximum value extracted from such a simulation is physically connected to adjacent computational points, whereas, in a typical PTHA with numerous tsunami sources, maxima from adjacent points can be from completely different scenarios. In our opinion, using a single scenario has obvious advantages provided it is sufficiently conservative to encompass uncertainties revealed in the PTHA. That said, it is quite possible to extract time history data from a PTHA by disaggregating individual simulations and picking one appropriate for the target exceedance. This option would be expedited by collecting time history data at each computational point as each simulation is run.

4.6 Tsunami Sources Not Evaluated

Some relatively rare tsunami sources were not evaluated in either the AECOM or DOGAMI studies. For example, submarine landslide tsunamis can be quite large in local areas near the slides. However, estimating the likelihood of such events is difficult. Three large submarine landslides have been mapped on the southern Oregon continental slope with estimated ages (from north to south) of 110,000 yrs, 450,000 yrs, and 1.2 million yrs (Goldfinger, and others, 2000). Events this old imply recurrence in the hundreds of thousands of years, so such sources would be irrelevant to 1,000-yr or 2.475-yr exceedances. One exception might be a probable incipient rotational slump offshore from Brookings (~42°07 N) on the continental slope measuring 20 × 20 km (Goldfinger, and others, 2000). This slump might well create a very localized tsunami threat to the Gold Beach-Brookings area, if triggered to further movement by a CSZ earthquake. Placing a probability on this event would, however, be a challenge. Other low-probability sources not considered are meteorites and volcanic eruptions.

Another source not explicitly considered by either DOGAMI or AECOM is a CSZ earthquake that causes large amounts of slip in the outermost part of the accretionary wedge, a “slip-to-the-trench” event like the 2011 Tohoku-oki earthquake in Japan (Tsuji and others, 2013). Priest and others (2014) noted that the continental slope of the southern Cascadia margin has a slope as steep as the slope in the Tohoku area and could be prone to such events. As noted previously, extreme slip events like the ~50–60 m characteristic of a Tohoku-type earthquake (Tsuji and others, 2013) would be difficult to accommodate in the 10,000-yr record without overshooting available slip deficit from convergence. Such an event would likely be very rare and unlikely to affect a 1,000-yr or 2,475-yr exceedance tsunami.

5.0 CONCLUSIONS

In a quasi-probabilistic PTHA based only on the most important control on 1,000-yr and 2,475-yr exceedance events, the CSZ sources, none of the DOGAMI (Witter and others, 2011, 2013; Priest and others, 2013) tsunami scenarios with published coast-wide data exactly match these exceedances, although two scenarios available only for the Bandon area do match (M3 for 1,000-yr and L2 for 2,475-yr exceedance). For coast-wide scenarios, the DOGAMI M1 scenario should approximate a conservative 1,000-yr exceedance and the L1 scenario a conservative 2,475-yr exceedance. The AECOM (Thio, 2017, 2019) PTHA does not generally match these expectations. Tsunami wave heights at 100 m offshore derived from the AECOM PTHA approximated L1 at the 1,000-yr exceedance and XL1 at the 2,475-yr exceedance. Wave heights or flow depths for both studies generally show the same disparity for open coastal sites in northern and central Oregon. Velocity and momentum flux data for the 1,000-yr exceedance of AECOM are more variable for the northern and central coast and estuaries but generally follow this same pattern. The exception to these generalizations is at Cannon Beach where AECOM 1,000-yr flow depths resemble XL1 at the Highway 101 bridge but velocities, momentum fluxes, and open coastal flow depths exceed XXL1. The reason for this anomaly is not known but could be either a function of AECOM earthquake sources or bathymetry, neither of which are available for detailed inspection.

The reason for the generally higher than expected AECOM tsunamis relative to DOGAMI results at the same probability offshore everywhere and onshore in northern and central Cascadia may be caused in part by 42 percent of the AECOM CSZ sources having seismic slip exceeding the largest slip deemed reasonable from CSZ slip budget considerations in the DOGAMI analysis, but it is hard to say without knowing the recurrences of AECOM's extreme events. The extreme slip on AECOM sources is probably caused in part by using variations in slip on sources to account for the aleatory uncertainties in not only earthquake sources but other modeling parameters as well.

AECOM 1,000-yr exceedance flow depths and inundation on the southern Oregon coastal and estuarine sites (Bandon to Gold Beach) appear to fall at or below the SM1 DOGAMI scenario, much lower than the observed L1 match at 100 m depth or the conservative M1 match predicted by the quasi-probabilistic PTHA. Potential bias of global scaling data toward underestimation of slip for narrow seismic ruptures like the inferred partial ruptures of the CSZ on the south coast or other factors such as the lower CSZ convergence rates of AECOM relative to the DOGAMI models may be contributing factors to the lower AECOM values. Lower values may also be caused by the AECOM PTHA being more influenced than the quasi-probabilistic PTHA by partial CSZ ruptures known from paleoseismic data to have occurred on the south coast. Theoretical energy balance considerations of Scholz (2014) can be interpreted to favor a larger north to south decrease of slip in the full-margin XL1, L1, and M1 fault rupture sources than used by DOGAMI to account for these partial ruptures; it remains to be seen whether incorporating this decrease is warranted or prudent until further analysis is undertaken to fully explore how it would affect a PTHA.

Aside from earthquake source issues, it was difficult to compare DOGAMI and AECOM inundation, flow depths, velocities, and momentum flux at inland bridge sites because of sometimes large differences in the underlying DEMs (digital elevation models) and differences in assumed bottom friction (Manning coefficient, n). Aside from some recent Columbia River simulations, all DOGAMI tsunami simulations use n = 0 to maximize inundation for hazard maps, whereas AECOM (Thio, 2019) used the more realistic value of n = 0.025, causing AECOM current velocities, flow depths, and momentum flux to decrease more quickly inland relative to DOGAMI simulations. The most serious differences in DEMs arose because the AECOM DEMs missed small estuarine channels like the Yachats River at Yachats. At Seaside the AECOM

computational grid did not extend far enough landward to reach the maximum inundation for comparison with DOGAMI results.

6.0 RECOMMENDATIONS

A new PTHA, incorporating lessons learned in the AECOM work and this review would be useful to more accurately place the DOGAMI tsunami scenarios in a probabilistic framework and to possibly develop new scenarios for engineering applications in areas near the CSZ. A new PTHA should involve a team of experts in hydrodynamic modeling of tsunamis, fault mechanics, seismology, paleoseismology, and creation of tsunami hazard assessment products for various user groups (i.e., engineers, planners, and the public). While workshops are useful for kicking off a PTHA, and sampling scientific and engineering expertise, they are no substitute for long-term participation of a team of experts who write the documentation, preferably in the form of peer-reviewed reports adequate for publication in professional journals.

If a new PTHA is not feasible, it may be possible to use DOGAMI source scenarios to do new tsunami simulations to approximate 1,000-yr or 2,475-yr exceedance tsunamis. We recommend that the scenarios be conservatively large to reflect the relatively large uncertainties revealed by comparison of DOGAMI and AECOM approaches, and that the new simulations be run with improved inputs. For example, the tsunami amplitudes of AECOM at 100 m depth approximate the DOGAMI scenario L1 at 1,000-yr exceedance and XL1 at 2,475-yr exceedance (**Figure 3-4** and **Figure 3-5**), so use of these two DOGAMI scenarios for these exceedances should encompass hazard estimates of both approaches. Simulations of inundation from the L1 and XL1 source scenarios should use a scientifically valid friction coefficient, either a standard value of 0.025 or, preferably, values varying with the type of landscape as adopted by Allan and others (2018) for the Columbia River. An example at the Columbia River of momentum flux estimates from this approach relative to that of AECOM is illustrated in **Figure 6-1**. The figure is constructed from a simulation of the L1 source with n = 0.025 from Allan and others (2018) and demonstrates that the resulting DOGAMI forces generally exceed the AECOM values, thus adding a safety factor. **Figure C-1** of Appendix C illustrates similar maps for the L1 scenario with n = 0.

Figure 6-1. Comparison of momentum flux from DOGAMI scenario L1 with friction (n = 0.025) relative to AECOM (Thio, 2019). Maps show (A) L1 minus AECOM, (B) L1, and (C) AECOM.

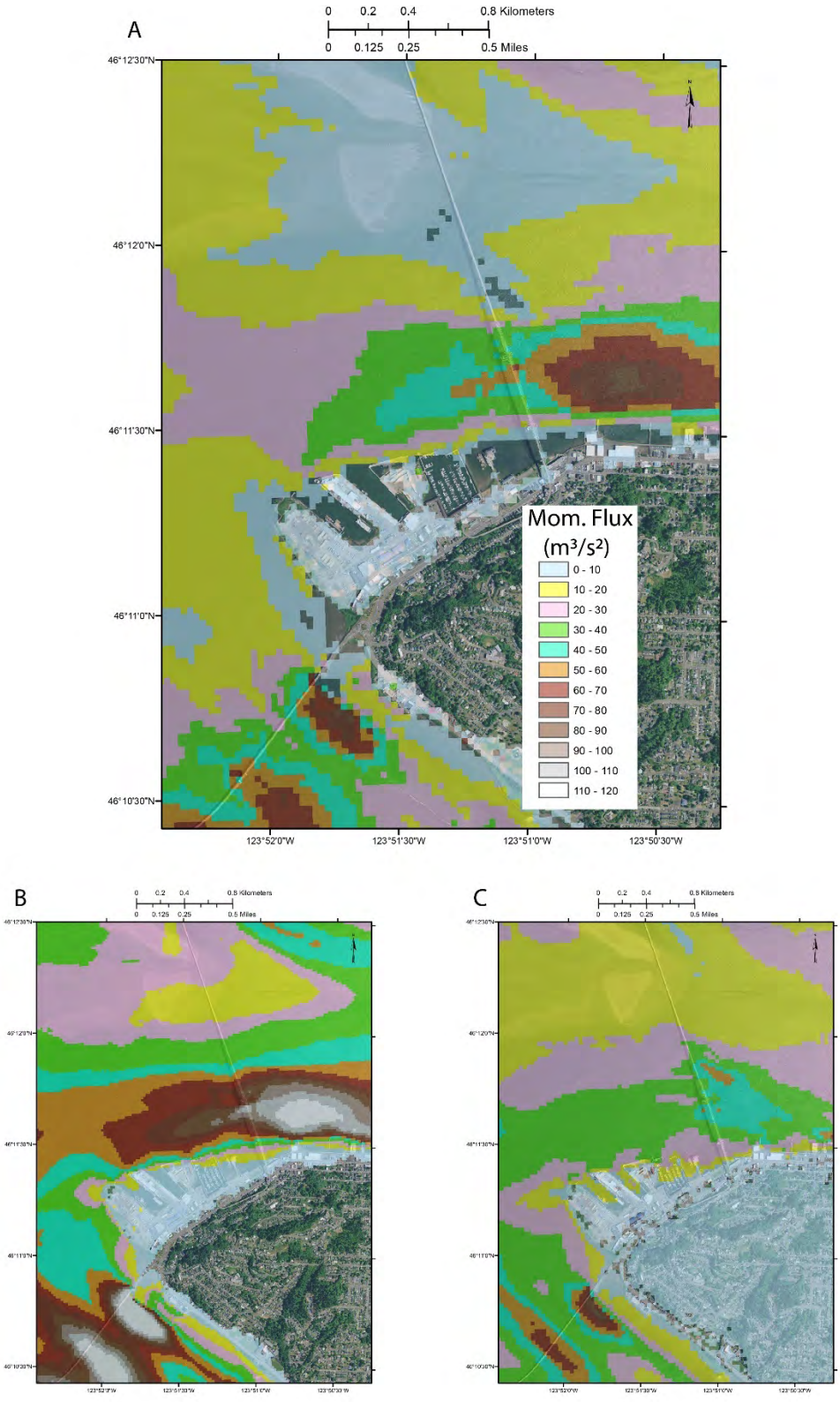

Any new site-specific simulations using the L1 source should incorporate improved computational grids and simulation approaches that fully describe the tsunami forces acting on the site. There should be a rigorous quality assessment of existing DOGAMI computational grids to remove errors and add needed bathymetric or topographic data. Furthermore, the grids should be refined at each site so that at least 10 computational points cover critical geomorphic influences and structural features of the engineering design. It is also possible to run the SCHISM finite element model (or some other model) in 3D mode for a local grid at the site to provide precise force data at varying depths in the water column. Time histories of wave arrivals can be extracted from each simulation to obtain vector directions, magnitudes, and durations of hydraulic forces.

Resolving the underlying reasons for differences between the DOGAMI and AECOM analyses was hampered by the limited amount of information available about the overall AECOM approach, particularly the CSZ sources and detailed procedures. Future comparisons of deterministic tsunami scenarios to PTHAs would be facilitated by providing enough documentation that both can be duplicated by other workers, including the following:

- Hydrodynamic simulation parameters (model type, Manning friction coefficients, etc.),
- Fault dislocation model (e.g., Okada point source or other) and procedure (grid density, method of specifying depth to the fault in submarine settings, etc.),
- Point data output from the fault dislocation model for vertical coseismic deformation and fault slip for all tsunami sources,
- Seismic source parameters (i.e., moment constraints such as uncertainties in rupture length, width, slip distributions, convergence vectors, and method of taking into account slip budget from convergence),
- All tsunami simulation grids for comparison of DEMs and for evaluation of how well earthquake source deformation and geomorphic features are simulated,
- Logic tree with full explanation of all branches, weights, and basis,
- Step-by-step examples of how a single probabilistic tsunami flow depth, velocity, or momentum flux is generated down key paths in the logic tree,
- Recurrences of all seismic or other tsunami sources, including effective recurrence at the end of each logic tree pathway,
- Probability density functions used for incorporation of uncertainties, including explanation of the basis for each function, how it is incorporated into the PTHA, and to what degree each influences the flow depths, velocities, and momentum flux estimates, and
- Examples in a few representative areas of disaggregation of PTHA sources to reveal degree of influence of each on tsunami flow depth, velocity, and momentum flux for target exceedances.

7.0 ACKNOWLEDGMENTS

This project was funded under Interagency Agreement #33063 between DOGAMI and ODOT.

We thank Hong Kie Thio of AECOM, Rick Wilson from the California Geological Survey, Patrick Lynett of the University of Southern California, and Ian Madin of the Oregon Department of Geology and Mineral Industries for comprehensive reviews and advice. Anne Tréhu of Oregon State University (OSU) and Kelin Wang of the Pacific Geoscience Centre provided reviews on specific issues in their fields of expertise. Chris Goldfinger of OSU provided the number of segment C and D events in the quasi-probabilistic PTHA.

8.0 REFERENCES

Adam, J., Klaeschen, D., Kukowski, N., and Flueh, E., 2004, Upward delamination of Cascadia Basin sediment infill with landward frontal accretion thrusting caused by rapid glacial age material flux: Tectonics, v. 23, p. TC3009. https://doi.org/10.1029/2002TC001475

Allan, J. C., Zhang, J., O'Brien, F. E., and Gabel, L. L., 2018, Columbia River tsunami modeling: toward improved maritime planning response: Oregon Department of Geology and Mineral Industries Special Paper 51, 77 p. https://www.oregongeology.org/pubs/sp/p-SP-51.htm

Atwater, B. F., Musumi, S., Satake, K., Tsuji, Y., Ueda, K., and Yamaguchi, D. K., 2005, The Orphan Tsunami of 1700: Japanese clues of a parent earthquake in North America: Seattle, Wash., University of Washington Press. 133 p. [2nd ed. available at https://doi.org/10.3133/pp1707]

Chock, G. Y. K., 2016, Design for tsunami loads and effects in the ASCE 7-16 standard: Journal of Structural Engineering, v. 142, no. 11. https://ascelibrary.org/doi/10.1061/%28ASCE%29ST.1943-541X.0001565.

Eakins B. W., and Taylor L. A., 2010, Seamlessly integrating bathymetric and topographic data to support tsunami modeling and forecasting efforts, chap. 2 *of* Breman, J., ed., Ocean Globe: Redlands, Calif., ESRI Press, p. 37–56.

Frankel, A., Chen, R., Peterson, M., Moschettti, M., and Sherrod, B., 2015, 2014 update of the Pacific Northwest portion of the U.S. National Seismic Hazard Maps: Earthquake Spectra, v. 31, no. S1, p. S131–S148. https://doi.org/10.1193/111314EQS193M

Gao, D., Wang, K., Insua, T. L., Sypus, M., Riedel, M., and Sun, T., 2018, Defining megathrust tsunami source scenarios for northernmost Cascadia: Natural Hazards, v. 94, no. 1, p. 445–469. https://doi.org/10.1007/s11069-018-3397-6

Geist, E. L., 1998, Local tsunamis and earthquake source parameters, *in* Dmowska, and R. Saltzman, B., eds., Tsunamigenic earthquakes and their consequences: Advances in Geophysics, v. 39, p. 2-1–2-16. https://doi.org/10.1016/S0065-2687(08)60276-9

Goldfinger, C., 1994, Active deformation of the Cascadia forearc: implications for great earthquake potential in Oregon and Washington: Corvallis, Oreg., Oregon State University, Ph.D. disserataion. https://ir.library.oregonstate.edu/concern/graduate_thesis_or_dissertations/w37639397

Goldfinger, C., Kulm, L. D., McNeill, L. C., and Watts, P., 2000, Super-scale failure of the southern Oregon Cascadia margin: Pure and Applied Geophysics, v. 157, no. 6-8, 1189–1226. https://doi.org/10.1007/s000240050

Goldfinger, C., Nelson, C. H., Morey, A. E., Johnson, J. E., Patton, J. R., Karabanov, E., Gutiérrez-Pastor, J., Eriksson, A. T., Gràcia, E., Dunhill, G., Enkin, R. J., Dallimore, A., and Vallier, T., 2012, Turbidite event history—Methods and implications for Holocene paleoseismicity of the Cascadia subduction zone: U.S. Geological Survey Professional Paper 1661–F, 170 p. https://pubs.usgs.gov/pp/pp1661f/

González, F. I., Geist, E. L., Jaffe, B., and others, 2009, Probabilistic tsunami hazard assessment at Seaside, Oregon, for near- and far-field seismic sources. Journal of Geophysical Research, v. 114, no. C11, https://doi.org/10.1029/2008JC005132

González, F. I., LeVeque, R. J., Adams, L. M., Goldfinger, C., Priest, G. R., and Wang, K., 2014, Probabilistic tsunami hazard assessment (PTHA) for Crescent City, CA: Final report. Accessed March 19, 2019 at https://digital.lib.washington.edu/researchworks/handle/1773/25916

Gutscher, M. A., Klaeschen, D., Flueh, E., and Malavieille, J., 2001, Non-Coulomb wedges, wrong-way thrusting, and natural hazards in Cascadia: Geology, v. 29, no. 5, p. 379–382. https://doi.org/10.1130/0091-7613(2001)029<0379:NCWWWT>2.0.CO;2

IRIS (Incorporated, Research Institutions for Seismology), [n.d.], Cascadia subduction zone [image; original source: U.S. Geological Survey]. https://www.iris.edu/hq/ssn/special_content/files/usgs_plateboundary.jpg. Accessed February 19, 2019.

Lynett, P. J., and others, 2017, Inter-model analysis of tsunami-induced coastal currents: Ocean Modelling, v. 114, p. 14–32. https://doi.org/10.1016/j.ocemod.2017.04.003

Mann, D. M., and Snavely, P. D., Jr., 1984, Multichannel seismic-reflection profiles collected in 1977 in the eastern Pacific Ocean off of the Washington/Oregon coast: U.S. Geological Survey Open-File Report 84-5, 3 p., 1 pl. https://doi.org/10.3133/ofr845

Martin, K., 2017, Schematic cross section of a subduction zone with an accretionary prism [image uploaded May 22, 2017]: Wikimedia Commons. Image licensed under the Creative Commons Attribution-Share Alike 4.0 International license (CC BY-SA 4.0). https://commons.wikimedia.org/wiki/File:Subduction_accretionary2.jpg. Accessed February 19, 2019.

McCrory, P. A., Blair, J. L., Oppenheimer, D. H., and Walter, S. R., 2004, Depth to the Juan de Fuca slab beneath the Cascadia subduction margin—a 3-D model for sorting earthquakes: USGS Data Series DS-91, ver. 1 [replaced by ver. 1.2, 2006]. http://pubs.usgs.gov/ds/91/

McCrory, P. A., Blair, J. L., Waldhauser, F., and Oppenheimer, D. H., 2012, Juan de Fuca slab geometry and its relation to Wadati-Benioff zone seismicity: Journal of Geophysical Research: Solid Earth, v. 117, no. B9, B09306. https://doi.org/10.1029/2012JB009407

Murotani, S., Satake, K., and Fujii, Y., 2013, Scaling relations of seismic moment, rupture area, average slip, and asperity size for $M{\sim}9$ subduction-zone earthquakes: Geophysical Research Letters, v. 40, no. 19, p. 5070–5074. https://doi.org/10.1002/grl.50976

Nishenko, S. P., 1991, Circum-Pacific seismic potential: 1989–1999: Pure and Applied Geophysics, v. 135, no. 2, p. 169-259. https://doi.org/10.1007/BF00880240

Papazachos, B., Scordilis, E., Panagiotopoulos, D., Papazachos, C. B., and Karakaisis, G. F., 2004, Global relations between seismic fault parameters and moment magnitude of earthquakes: Bulletin of the Geological Society of Greece, v. 36, no. 3, p. 1482–1489. http://dx.doi.org/10.12681/bgsg.16538

Petersen, M.D., Moschetti, M.P., Powers, P.M., Mueller, C. S., Haller, K. M., Frankel, A. D., Zeng, Yuehua, Rezaeian, Sanaz, Harmsen, S. C., Boyd, O. S., Field, Ned, Chen, Rui, Rukstales, K. S., Luco, Nico, Wheeler, R. L., Williams, R. A., and Olsen, A. H., 2014, Documentation for the 2014 update of the United States national seismic hazard maps: U.S. Geological Survey Open-File Report 2014–1091, 243 p., https://dx.doi.org/10.3133/ofr20141091

Priest, G. R., Goldfinger, C., Wang, K., Witter, R., Zhang, Y., and Baptista, A. M., 2009, Tsunami hazard assessment of the northern Oregon coast: a multi-deterministic approach tested at Cannon Beach, Clatsop County, Oregon: Oregon Department of Geology Mineral Industries Special Paper 41, 87 p. https://www.oregongeology.org/pubs/sp/SP-41.zip

Priest, G. R., Goldfinger, C., Wang, K., Witter, R., Zhang, Y., and Baptista, A. M., 2010, Confidence levels for tsunami-inundation limits in northern Oregon inferred from a 10,000-year history of great earthquakes at the Cascadia subduction zone: Natural Hazards, v. 54, no. 1, 27–73. https://doi.org/10.1007/s11069-009-9453-5

Priest, G. R., Witter, R. C., Zhang, Y. J., Wang, K., Goldfinger, C., Stimely, L. L., English, J. T., Pickner, S. G., Hughes, K. L. B., Willie, T. E., and Smith, R. L., 2013, Tsunami inundation scenarios for Oregon: Oregon Department of Geology and Mineral Industries Open-File Report O-13-19. https://www.oregongeology.org/pubs/ofr/p-O-13-19.htm

Priest, G. R.., Zhang, Y., Witter, R.C., Wang, K., Goldfinger, C., Stimely, L., 2014, Tsunami impact to Washington and northern Oregon from segment ruptures on the southern Cascadia subduction zone: Natural Hazards, v. 72, no. 2, 849-870. https://doi.org/10.1007/s11069-014-1041-7

Priest, G. R., Witter, R. C., Zhang, Y. J., Goldfinger, C., Wang, K., and Allan, J.C., 2017, New constraints on coseismic slip during southern Cascadia subduction zone earthquakes over the past 4600 years implied by tsunami deposits and marine turbidites: Natural Hazards, v. 88, no. 1, 285–313. https://doi.org/10.1007/s11069-017-2864-9

Priest, G. R., Witter, R. C., Zhang, Y. J., Goldfinger, C., Wang, K., and Allan, J. C., 2018, Correction to: New constraints on coseismic slip during southern Cascadia subduction zone earthquakes over the past 4600 years implied by tsunami deposits and marine turbidites: Natural Hazards, v. 93, no. 2, 1109–1111. https://doi.org/10.1007/s11069-018-3405-x

Scholz, C. H., 2014, Holocene earthquake history of Cascadia: a quantitative test: Bulletin of the Seismological Society of America, v. 104, no. 4, p. 2120–2124. https://doi.org/10.1785/0120140002

Skarlatoudis, A. A., Somerville, P. G., and Thio, H. K., 2016, Source-scaling relations of interface subduction earthquakes for strong ground motion and tsunami simulation: Bulletin of the Seismological Society of America, v. 106, no. 4, p. 1652-1662. https://doi.org/10.1785/0120150320

Strasser, F. O., Arango, M. C., and Bommer, J. J., 2010, Scaling of the source dimensions of interface and intraslab subduction-zone earthquakes with moment magnitude: Seismological Research Letters, v. 81, no. 6, p. 941–950.

Thio, H. K., 2017, Probabilistic tsunami hazard maps for the State of California (phase 2): draft report (in review) by AECOM to the California Geological Survey.

Thio, H. K., 2019, Notes on the production of the 1,000 year probabilistic tsunami hazard maps for the Western United States: draft report (in review) by AECOM to the California Geological Survey.

Tréhu, A. M., 2016, Source parameter scaling and the Cascadia paleoseismic record: Bulletin of the Seismological Society of America, v. 106, no. 3, p. 904-911. https://doi.org/10.1785/0120150272

Tsuji, T., Kawamura, K., Kanamatsu, T., Kasaya, T., Fujikura, K., Ito, Y., Tsuru, T., Kinoshita, M., 2013, Extension of continental crust by anelastic deformation during the 2011 Tohoku-oki earthquake: the role of extensional faulting in the generation of a great tsunami: Earth Planetary Science Letters, v. 364, p. 44-58. https://doi.org/10.1016/j.epsl.2012.12.038

Wang, K., and He, J., 2008, Effects of frictional behavior and geometry of subduction fault on coseismic seafloor deformation: Bulletin of the Seismological Society of America, v. 98, no. 2, p. 571–579. https://doi.org/10.1785/0120070097

Wang, K., and Hu, Y., 2006, Accretionary prisms in subduction earthquake cycles: the theory of dynamic Coulomb wedge: Journal of Geophysical Research, v. 111, no. B6, B06410. https://doi.org/10.1029/2005JB004094

Wang, K., Wells, R., Mazzotti, S., Hyndman, R.D., and Sagiya T., 2003, A revised dislocation model of interseismic deformation of the Cascadia subduction zone: Journal of Geophysical Research, v. 108, no. B1. https://doi.org/10.1029/2001JB001227

Wang, K., Sun, T., Brown, L., Hino, R., Tomita, F., Kido, M., Linuma, R., Kodaira, S., and Fujiwara, T., 2018, Learning from crustal deformation associated with the M9 2011 Tohoku-oki earthquake: Geosphere, v. 14, no. 2, 552-571. https://doi.org/10.1130/GES01531.1

Witter, R. C., Zhang, Y. J., Wang, K., Priest, G. R., Goldfinger, C., Stimely, L., English, J. T., and Ferro, P. A., 2011, Simulating tsunami inundation at Bandon, Coos County, Oregon, using hypothetical Cascadia and Alaska earthquake scenarios: Oregon Department of Geology Mineral Industries Special Paper 43, 57 p. https://www.oregongeology.org/pubs/sp/p-SP-43.htm

Witter, R. C., Zhang, Y., Wang, K., Goldfinger, C., Priest, G. R., and Allan, J. C., 2012, Coseismic slip on the southern Cascadia megathrust implied by tsunami deposits in an Oregon lake and earthquake-triggered marine turbidites: Journal of Geophysical Research v. 117, no. B10303. https://doi.org/10.1029/2012JB009404

Witter, R. C., Zhang, Y. J., Wang, K., Priest, G. R., Goldfinger, C., Stimely, L., English J. T., and Ferro P. A., 2013, Simulated tsunami inundation for a range of Cascadia megathrust earthquake scenarios at Bandon, Oregon, USA: Geosphere, v. 9, no. 6, 1783–1803. https://doi.org/10.1130/GES00899.1

Zhang, Y., and Baptista, A. M., 2008, An efficient and robust tsunami model on unstructured grids; Part I, inundation benchmarks: Pure and Applied Geophysics, v. 165, no. 11-12, p. 2229–2248. https://doi.org/10.1007/s00024-008-0424-7

Zhang, Y., Witter, R. W., and Priest, G. R., 2011, Tsunami-tide interaction in 1964 Prince William Sound tsunami: Ocean Modelling, v. 40, no. 3-4, 246–259. https://doi.org/10.1016/j.ocemod.2011.09.005

Zhang, Y. J., Stanev, E. V., Ye, F., and Grashorn, S., 2016a, Seamless cross-scale modelling with SCHISM: Ocean Modelling, v. 102, p. 64–81. https://doi.org/10.1016/j.ocemod.2016.05.002

Zhang, Y. J., Priest, G. R., Allan, J. C., and Gabel, L., 2016b, Benchmarking an unstructured-grid model for tsunami current modeling: Pure and Applied Geophysics, v. 173, no. 12, p. 4075–4087. https://doi.org/10.1007/s00024-016-1328-6

APPENDIX A. MAP VIEWS OF COMPUTATIONAL GRIDS AT EACH SITE

The following map views (**Figure A-1** through **Figure A-21**) for each observation site illustrate differences in the grid spacing and underlying DEMs between AECOM (Thio, 2019) and DOGAMI (Witter and others, 2011, 2013; Priest and others, 2013) simulations. AECOM lists elevations above MHW, whereas DOGAMI lists bathymetric depths below MHHW; thus water depths are negative for AECOM and positive for DOGAMI. There is only ~0.2 m difference between MHW and MHHW. DOGAMI-AECOM difference maps are generated by summing DOGAMI and AECOM raster maps after subtracting 0.2 m from the AECOM DEM. The difference map is followed by a detailed view of the computational grid where comparison points were chosen for **Table B-1**. Comparison points are circled. Base maps are 2009 orthophotographs. Red triangles are AECOM grid points and yellow dots are DOGAMI grid points; all DEM values are in meters. **Figure A-12** also includes gray-scale raster maps to more clearly illustrate differences in the ways AECOM and DOGAMI DEMs depict channels in Alsea Bay, Waldport.

Figure A-1. DOGAMI-AECOM DEM difference at the Highway 101 bridge over the Columbia River at Astoria. Box is the locality of a detailed view of the computational grids in the next figure.

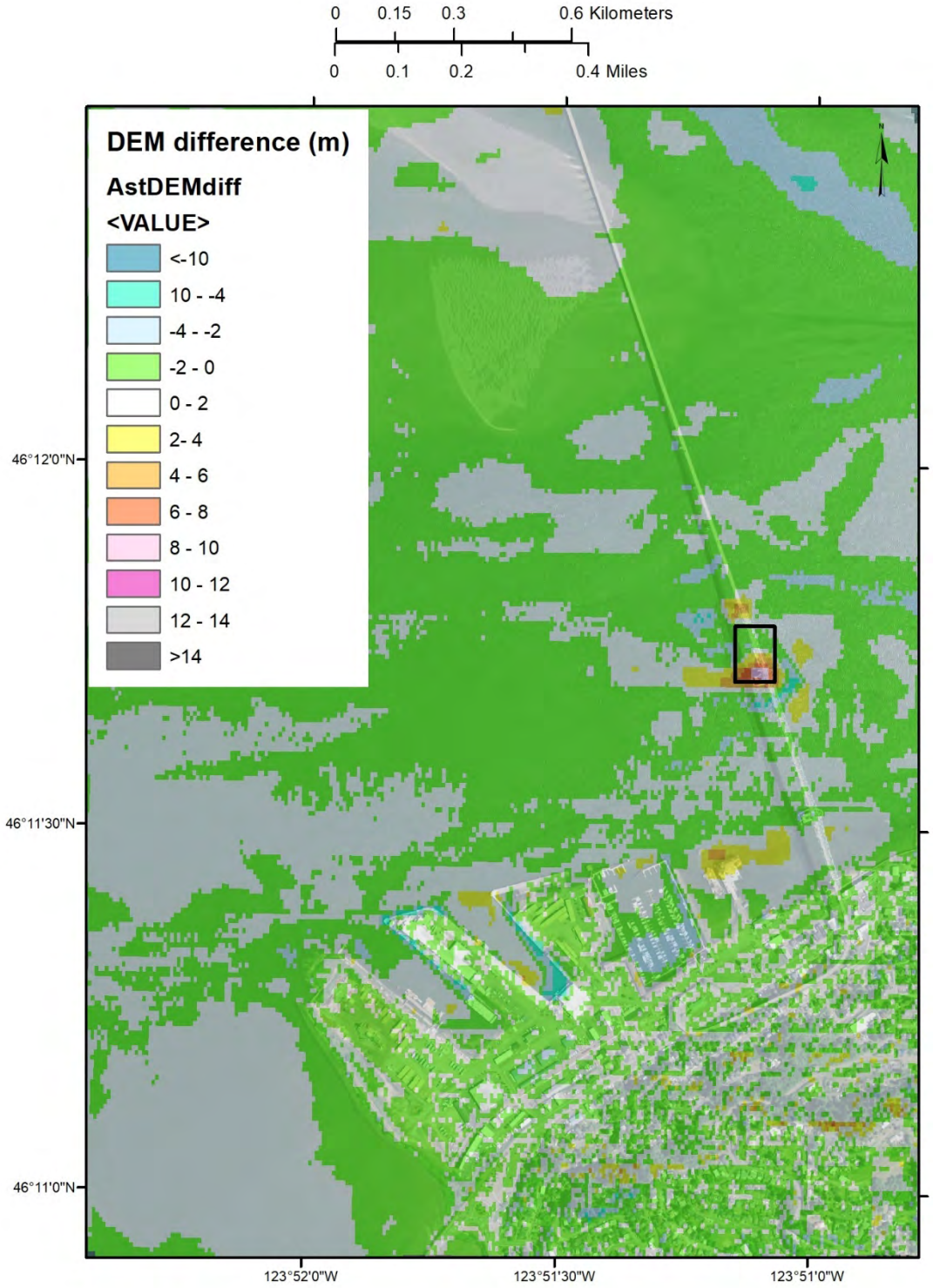

Figure A-2. DEMs at the Highway 101 bridge over the Columbia River at Astoria. Observation point is circled.

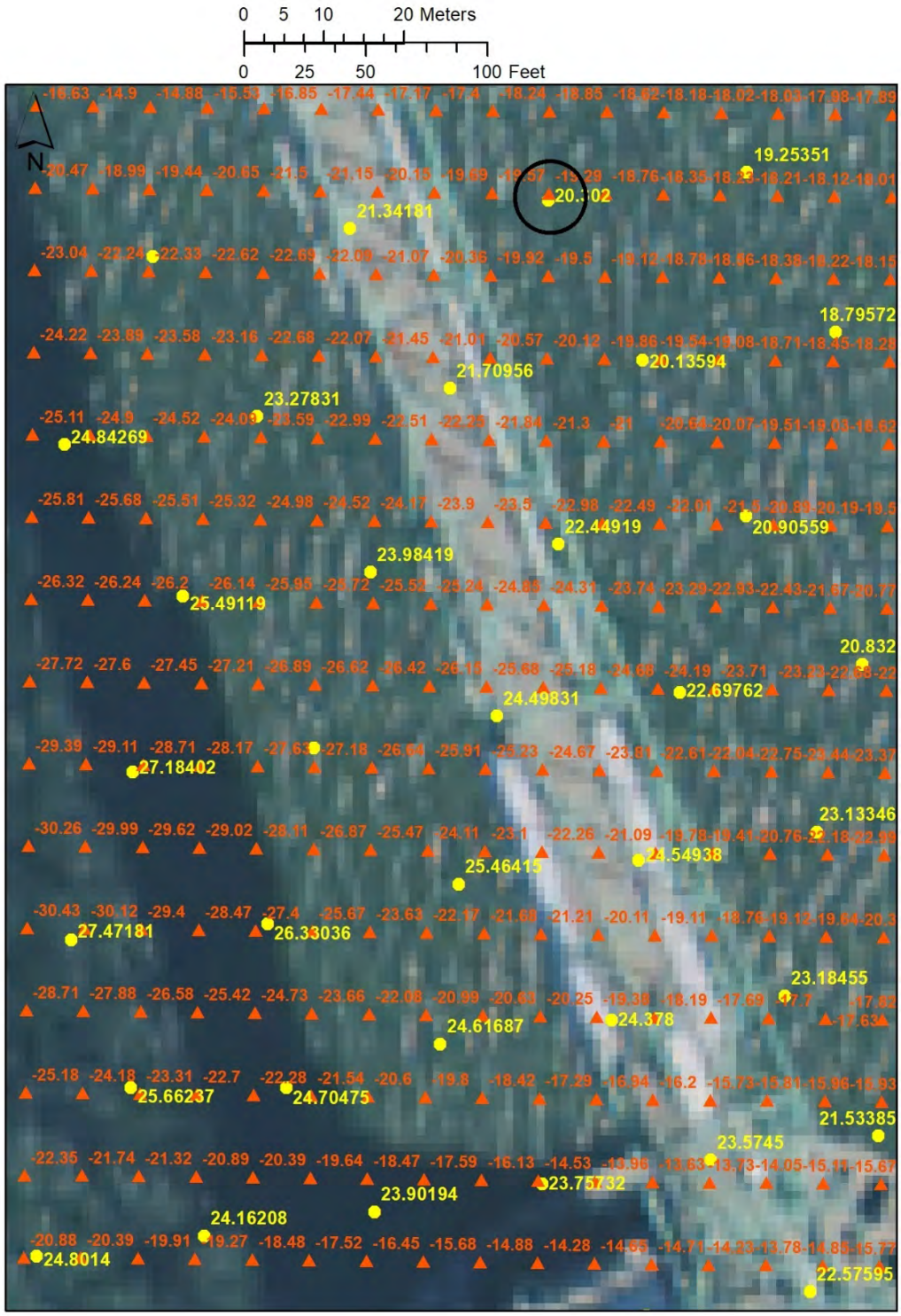

Figure A-3. DOGAMI-AECOM DEM difference at the Highway 101 bridge over Neawanna Creek at Seaside. Box is the locality of a detailed view of the computational grids in the next figure.

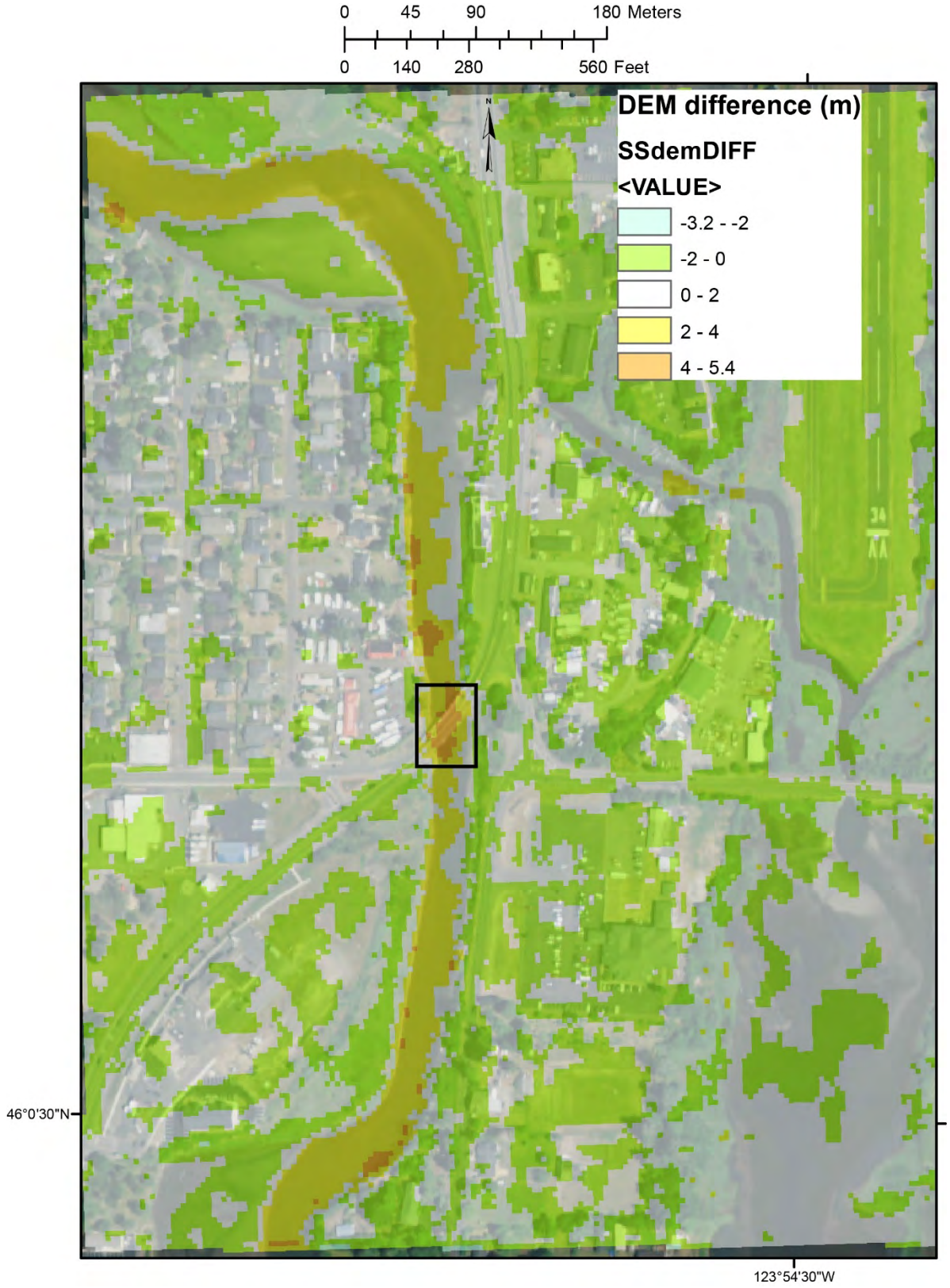

Figure A-4. DEMs at the Highway 101 bridge over Neawanna Creek at Seaside. Observation point is circled.

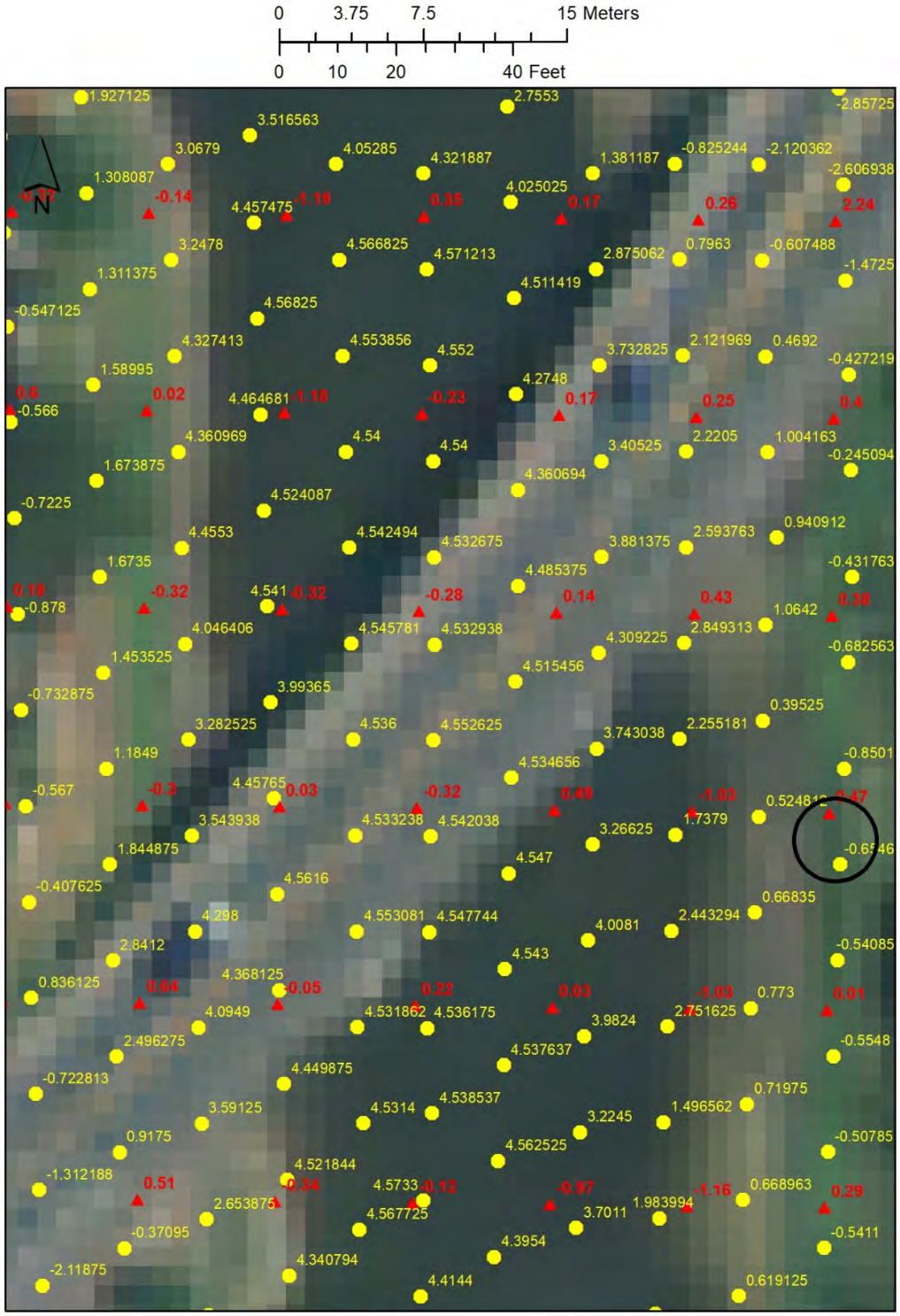

Figure A-5. DOGAMI-AECOM DEM difference at the Highway 101 bridge over Ecola Creek at Cannon Beach. Box is the locality of a detailed view of the computational grids in the next figure.

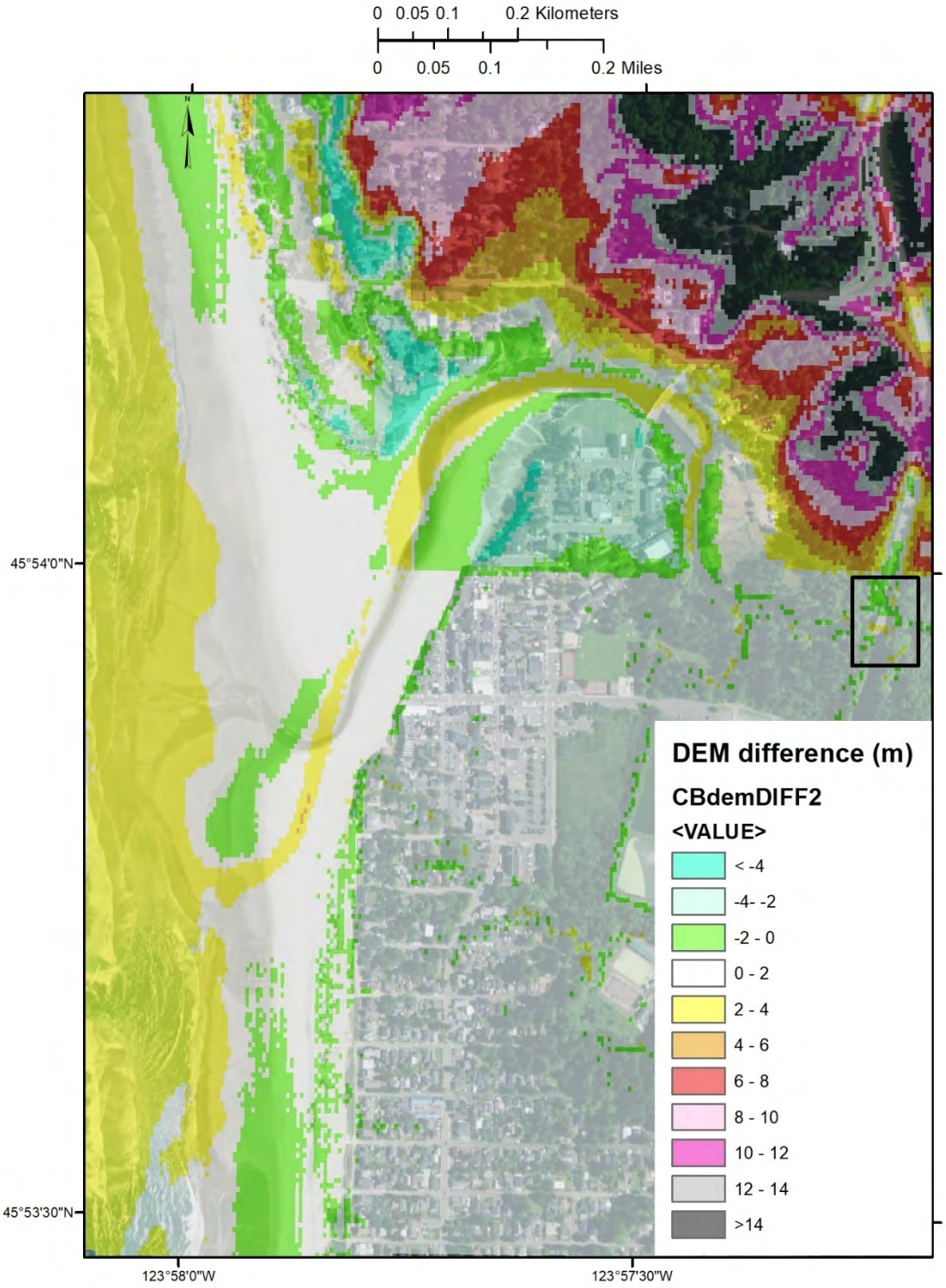

Figure A-6. DEMs at the Highway 101 bridge over Ecola Creek at Cannon Beach. Observation point is circled.

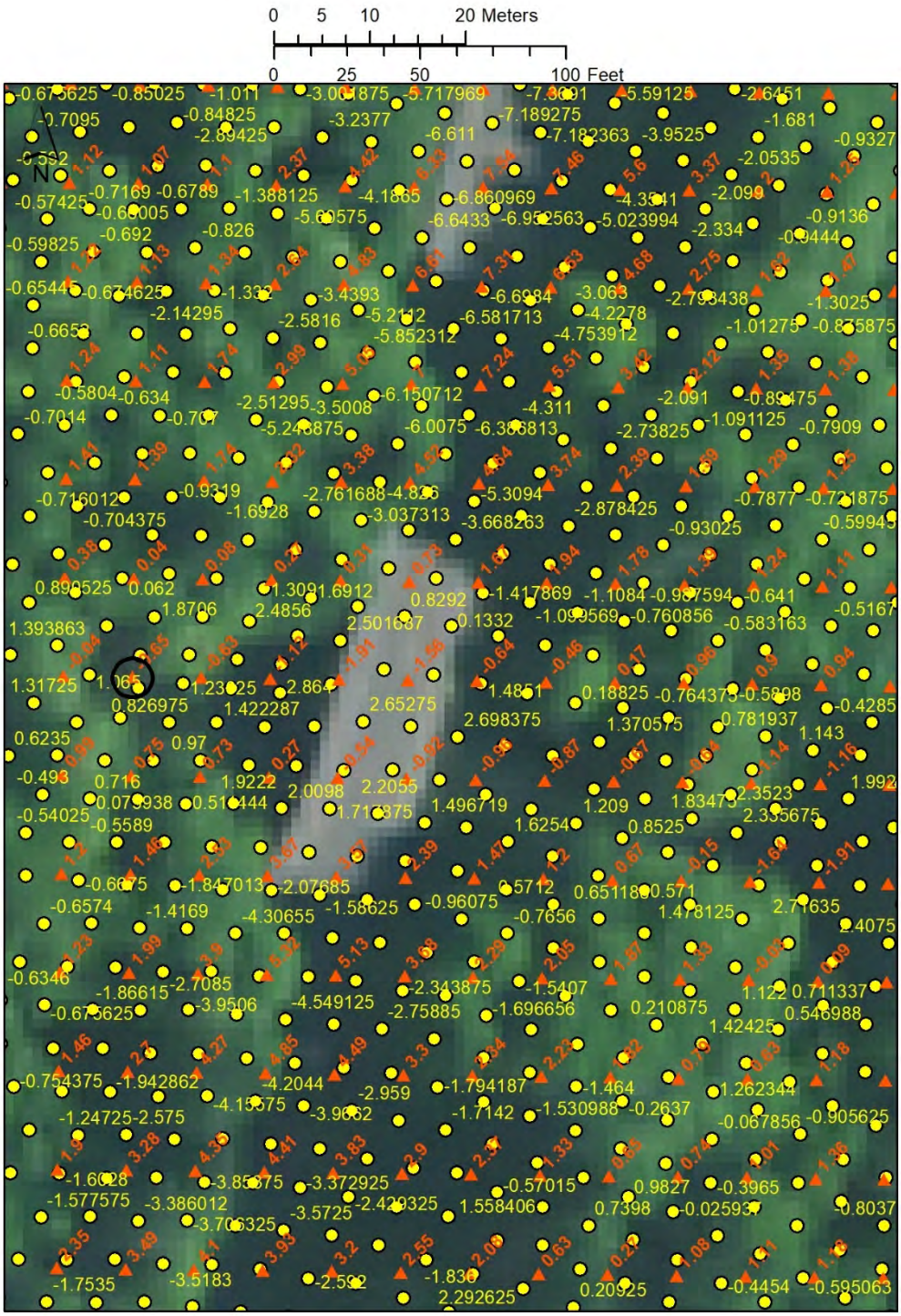

Figure A-7. DOGAMI-AECOM DEM difference at the Highway 101 bridge over the Siletz River at Lincoln City. Box is the locality of a detailed view of the computational grids in the next figure.

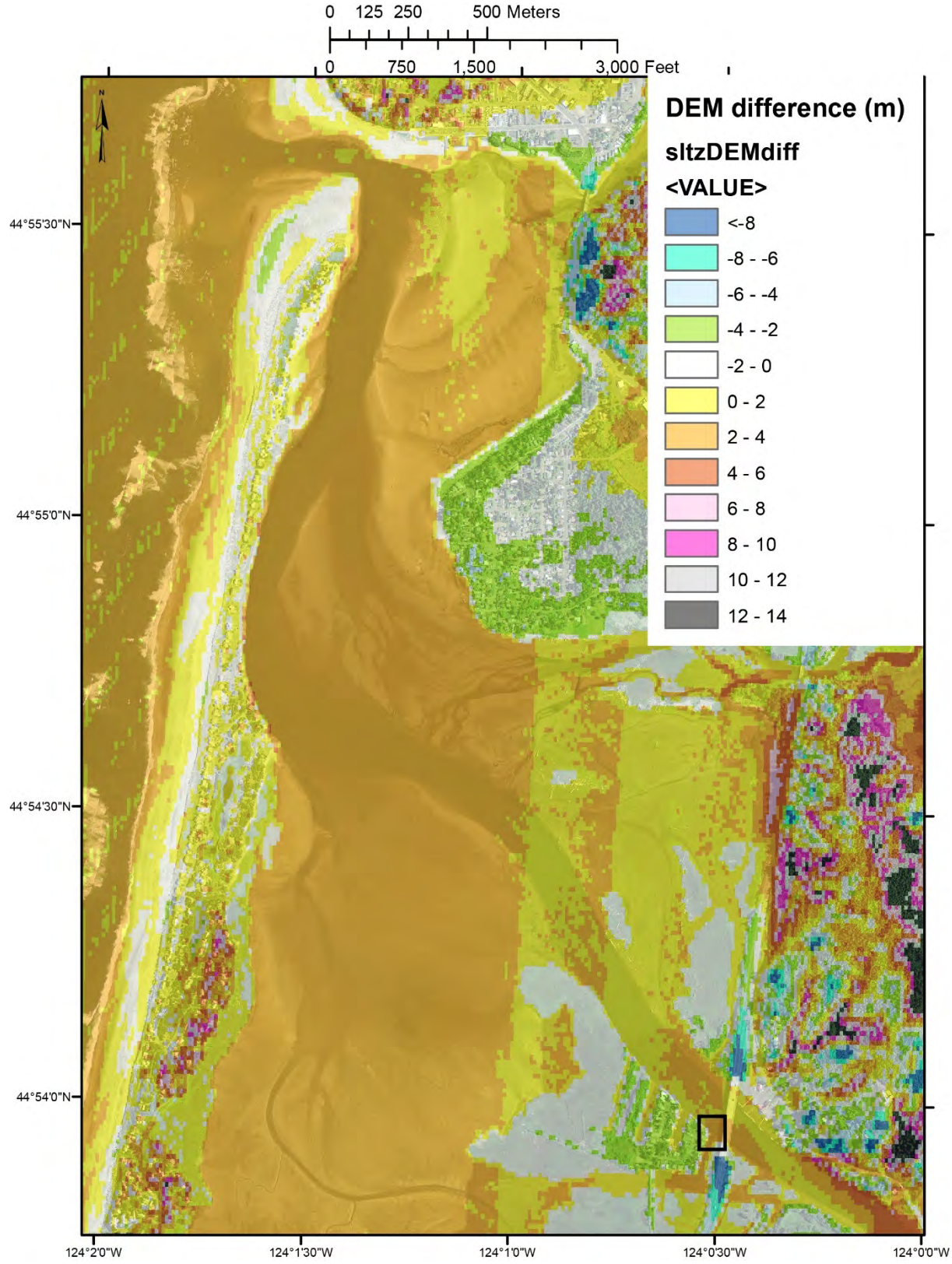

Figure A-8. DEMs at the Highway 101 bridge over the Siletz River at Lincoln City. Observation point is circled.

Figure A-9. DOGAMI-AECOM DEM difference at the Highway 101 bridge over Yaquina Bay at Newport. Box is the locality of a detailed view of the computational grids in the next figure.

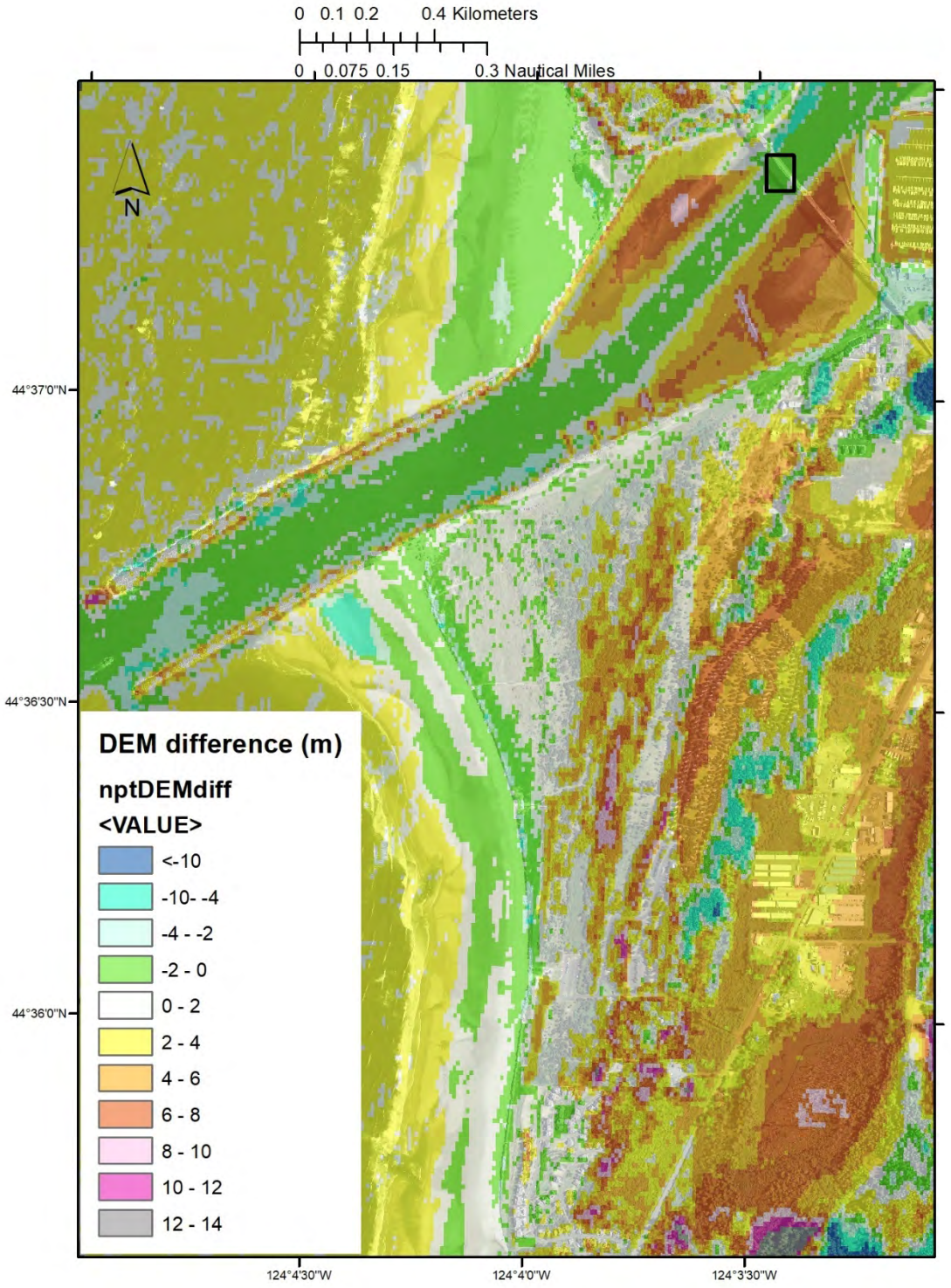

Figure A-10. DEMs at the Highway 101 bridge (north side) over Yaquina Bay at Newport. Observation point is circled.

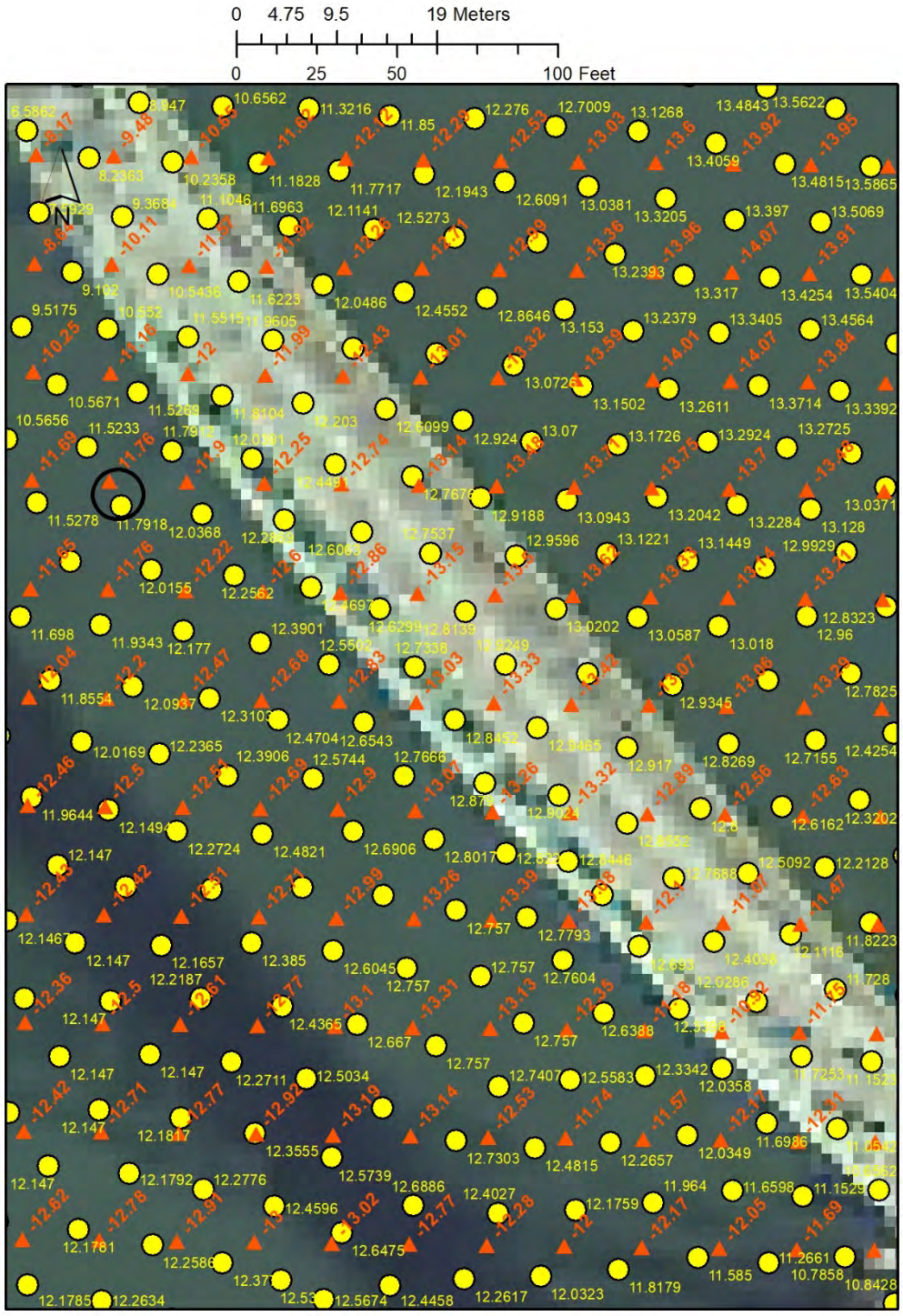

Figure A-11. DOGAMI-AECOM DEM difference at the Highway 101 bridge over Alsea Bay, Waldport. Box is the locality of a detailed view of the computational grids in Figure A-13.

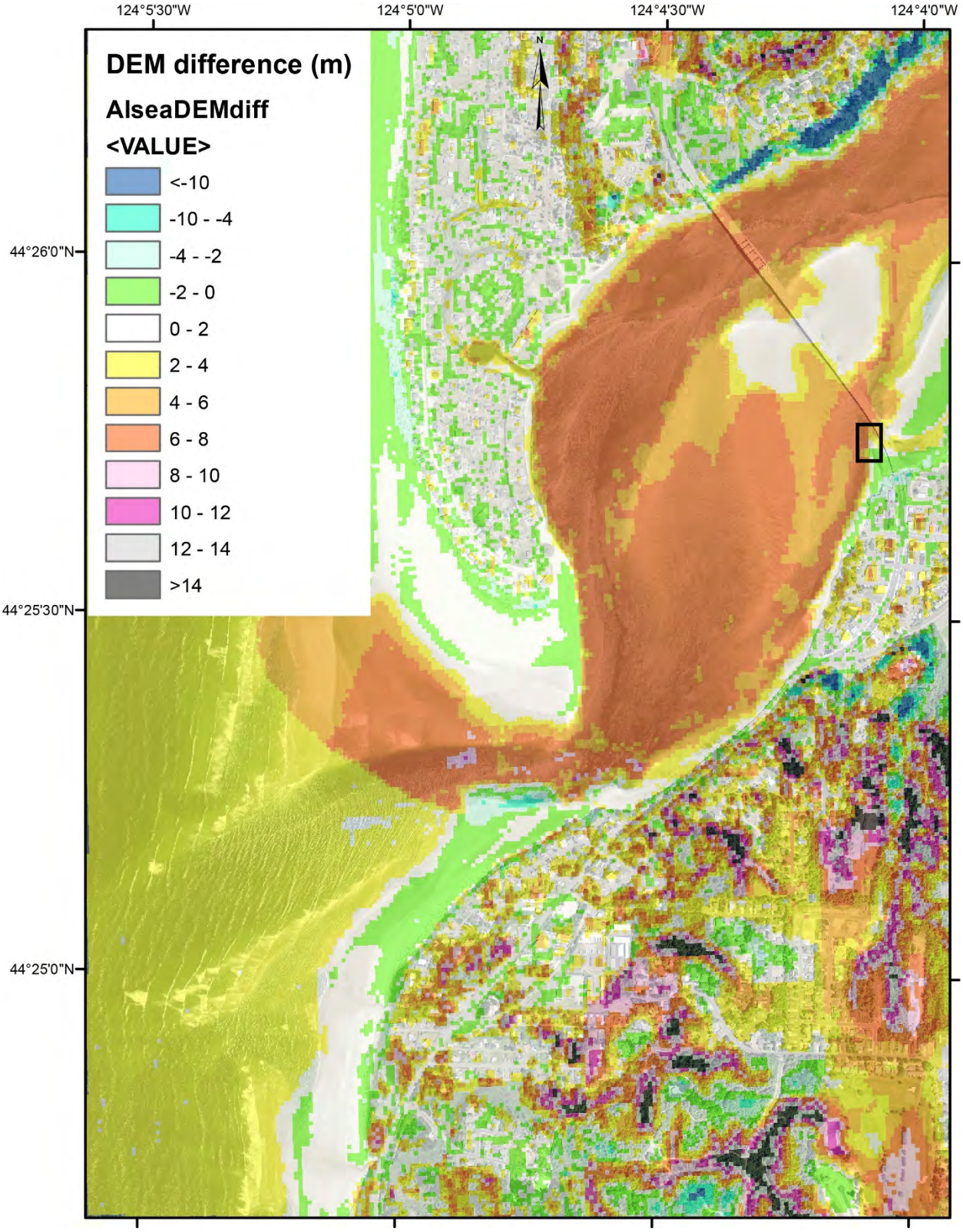

Figure A-12. Comparison at Alsea Bay, Waldport of (A) a 2009 orthophotograph to gray-shaded views of the DEMs of (B) AECOM, and (C) DOGAMI. Shades of gray in B and C darken from -10 m to +10 m depth below the sea level datum at MHHW (mean higher high water). Box is the locality of a detailed view of the computational grids in the next figure.

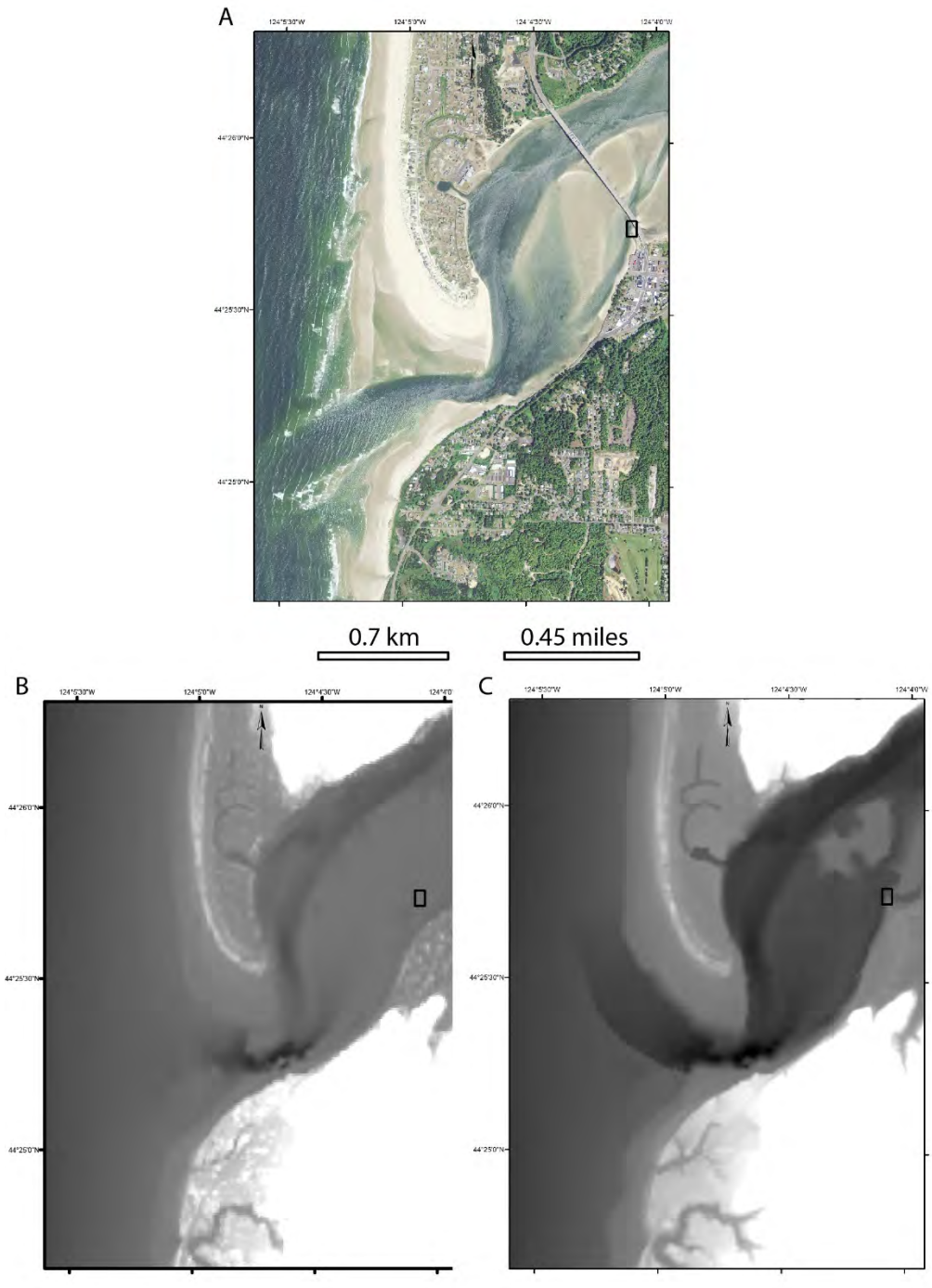

Figure A-13. DEMs at the Highway 101 bridge, Alsea Bay (south side) at Waldport. Observation point is circled.

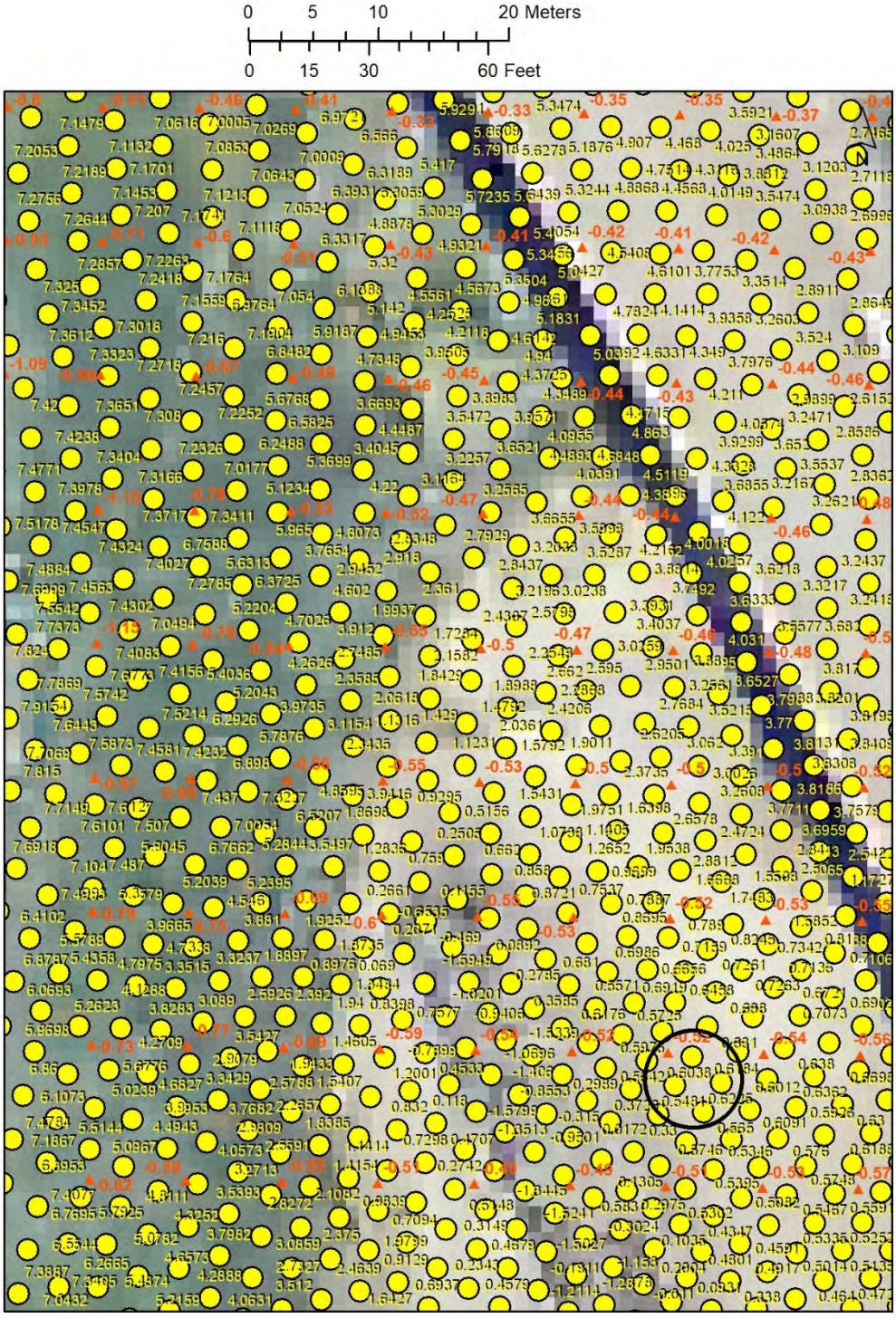

Figure A-14. DOGAMI-AECOM DEM difference at the Highway 101 bridge over the Yachats River at Yachats. Box is the locality of a detailed view of the computational grids in the next figure.

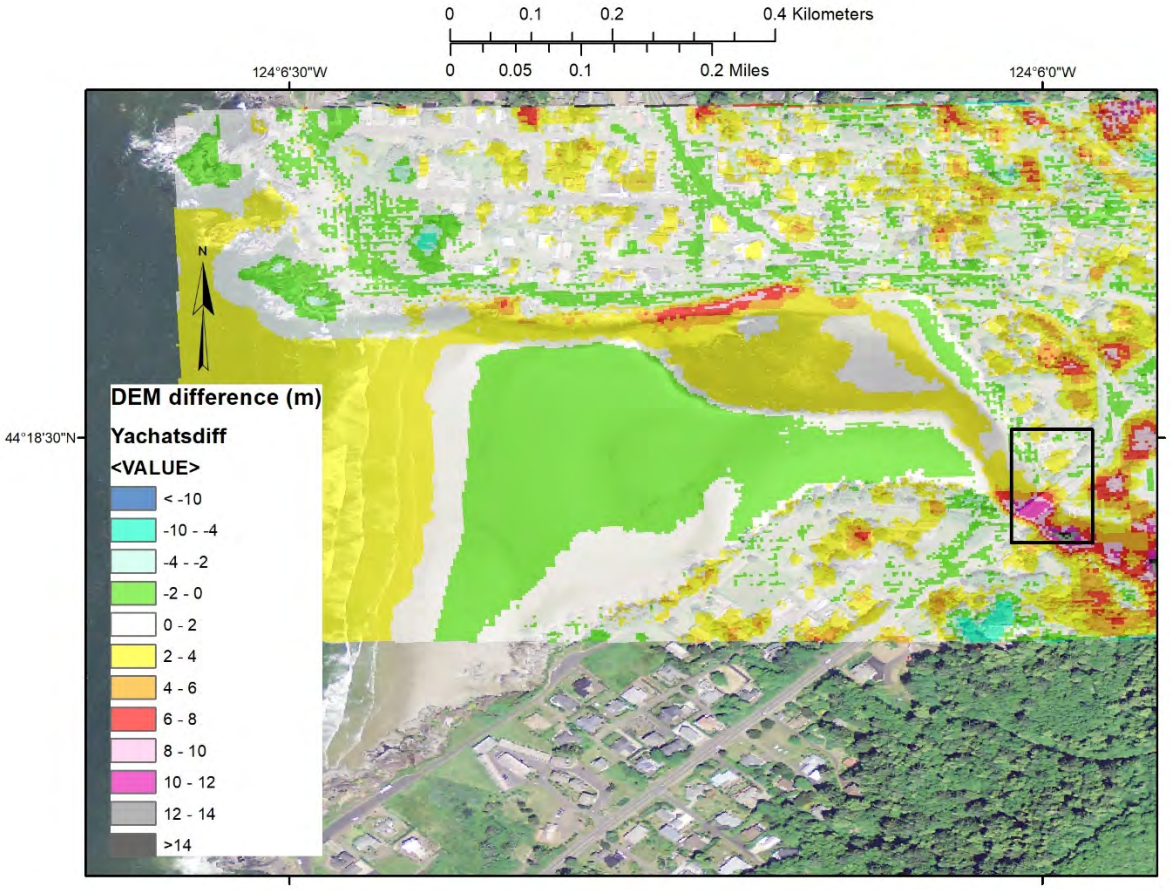

Figure A-15. DEMs at the Highway 101 Bridge over the Yachats River at Yachats. Observation point is circled.

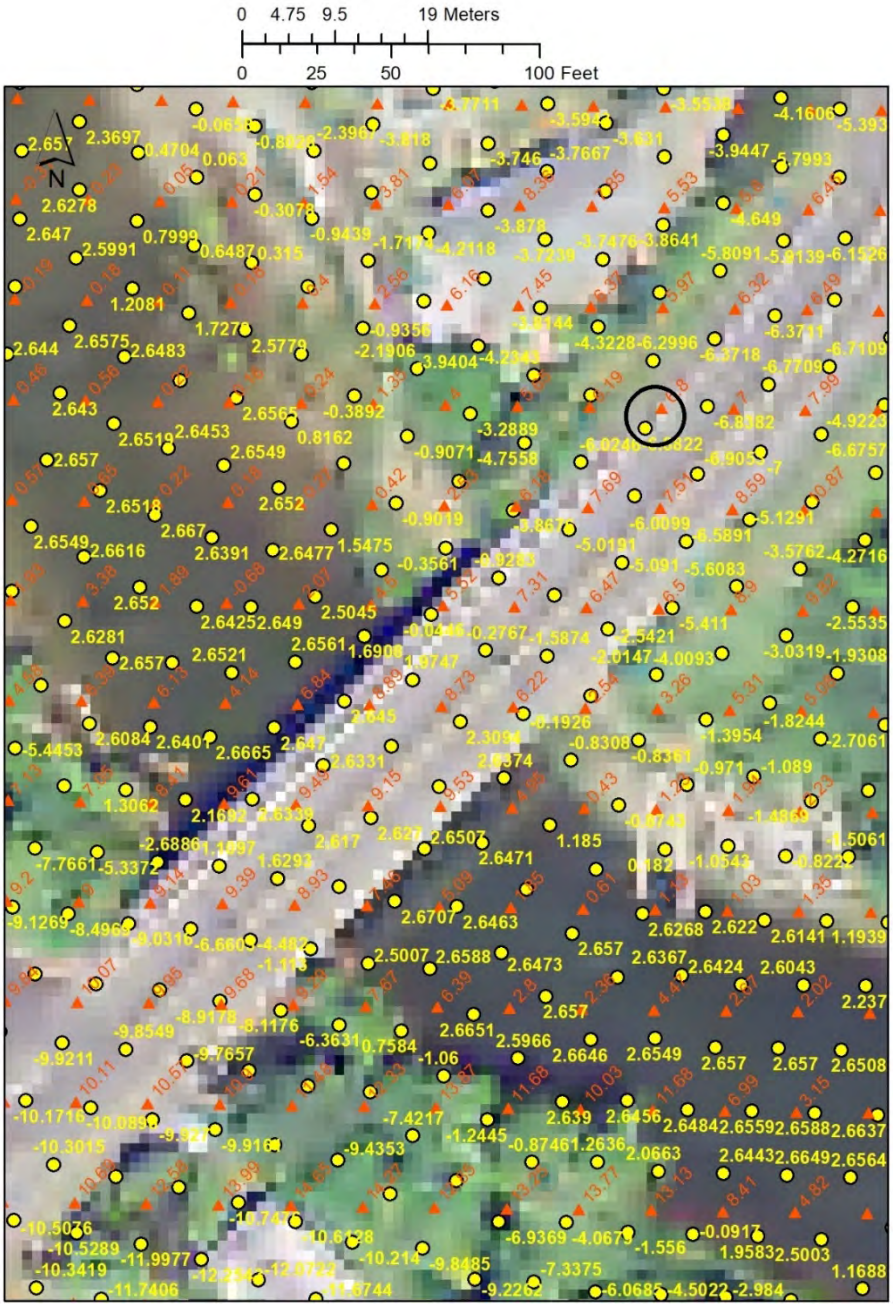

Figure A-16. DOGAMI-AECOM DEM difference at the Highway 101 bridge over the Coquille River at Bandon. Box is the locality of a detailed view of the computational grids in the next figure.

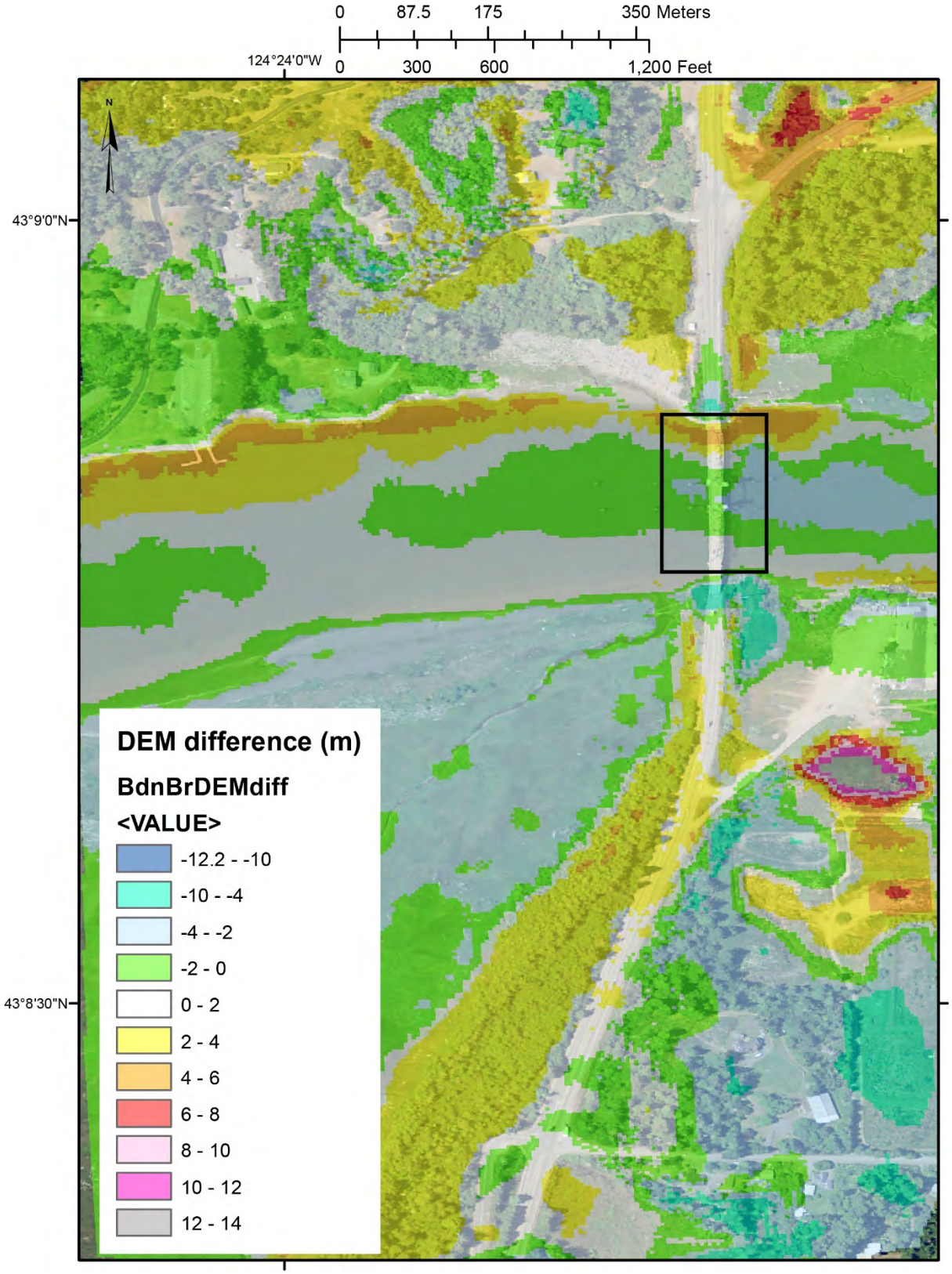

Figure A-17. DEMs at the Highway 101 bridge over the Coquille River at Bandon. Observation point is circled.

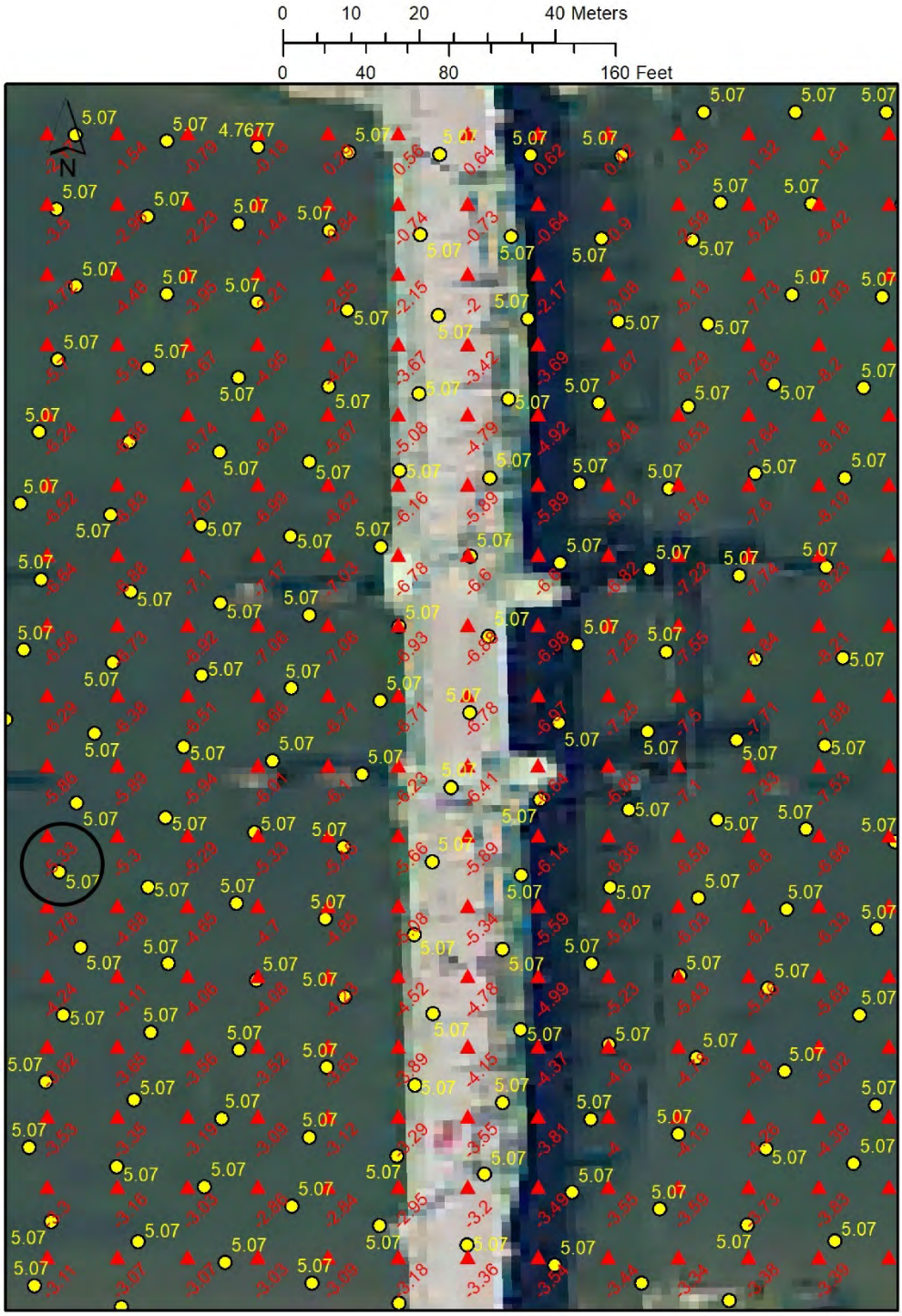

Figure A-18. DOGAMI-AECOM DEM difference at the Coquille estuary mouth at Bandon. Box is the locality of a detailed view of the computational grids in the next figure.

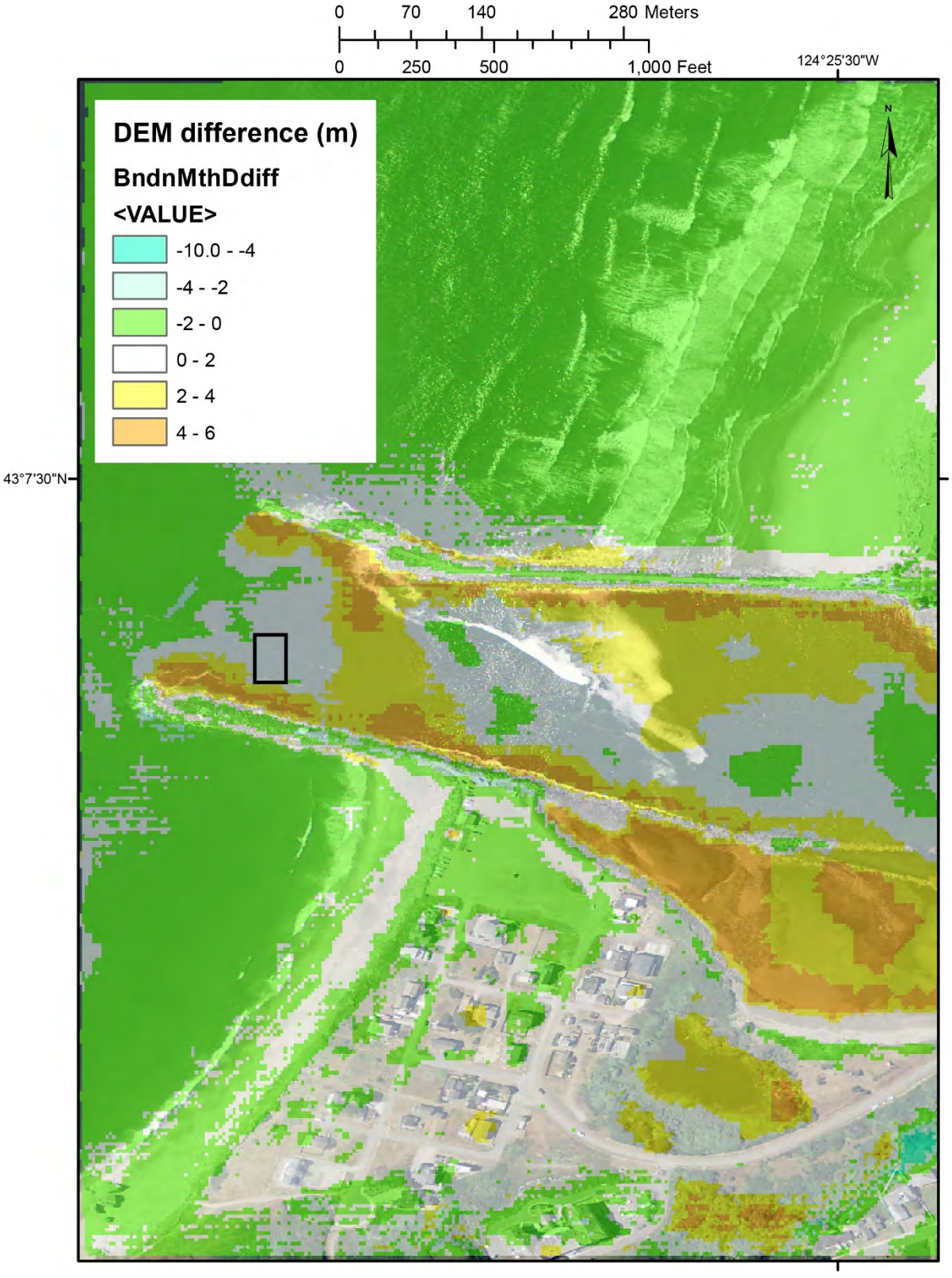

Figure A-19. DEMs at the Coquille estuary mouth at Bandon. Observation point is circled.

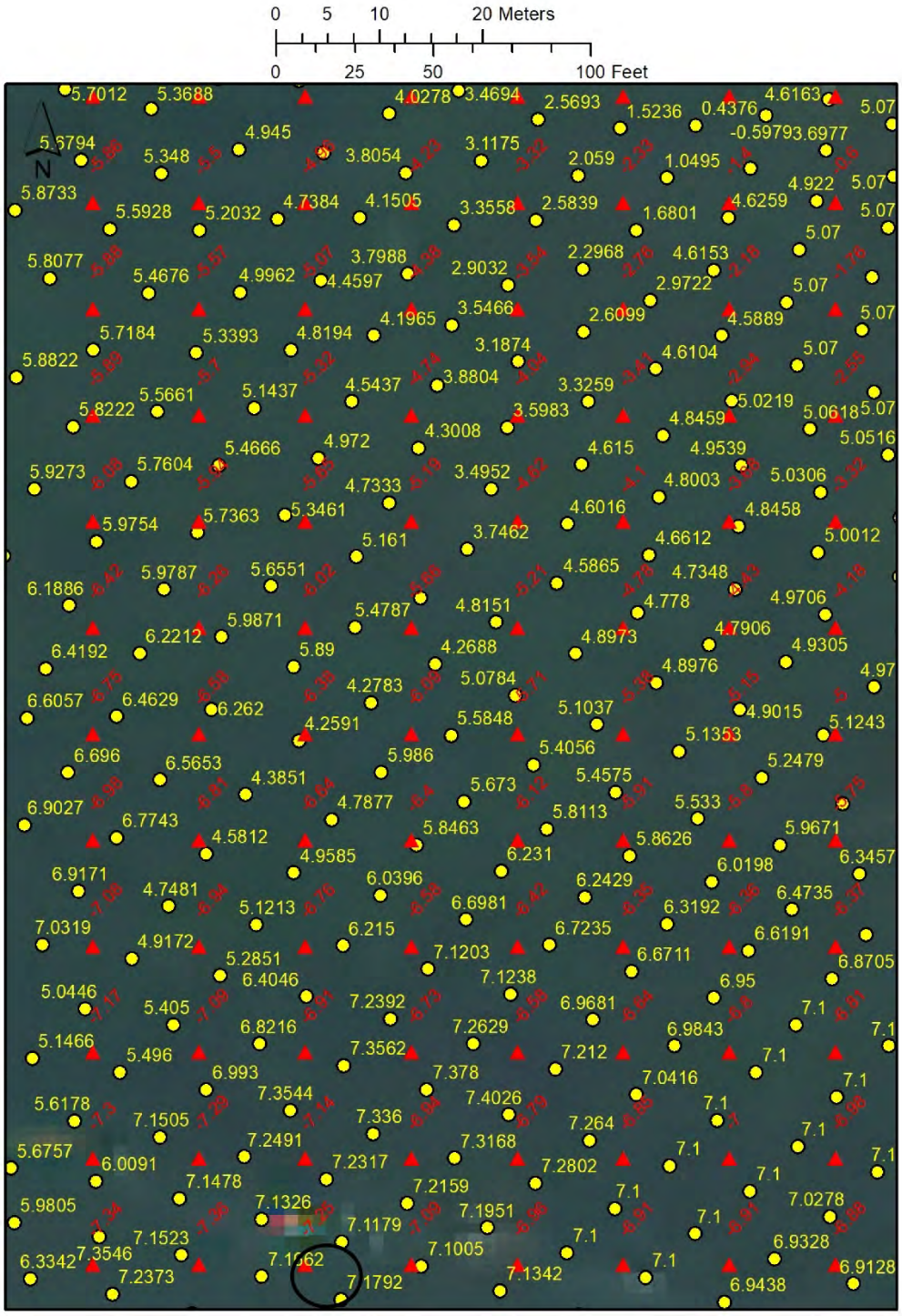

Figure A-20. DOGAMI-AECOM DEM difference at the Highway 101 bridge over the Rogue River at Gold Beach. Box is the locality of a detailed view of the computational grids in the next figure.

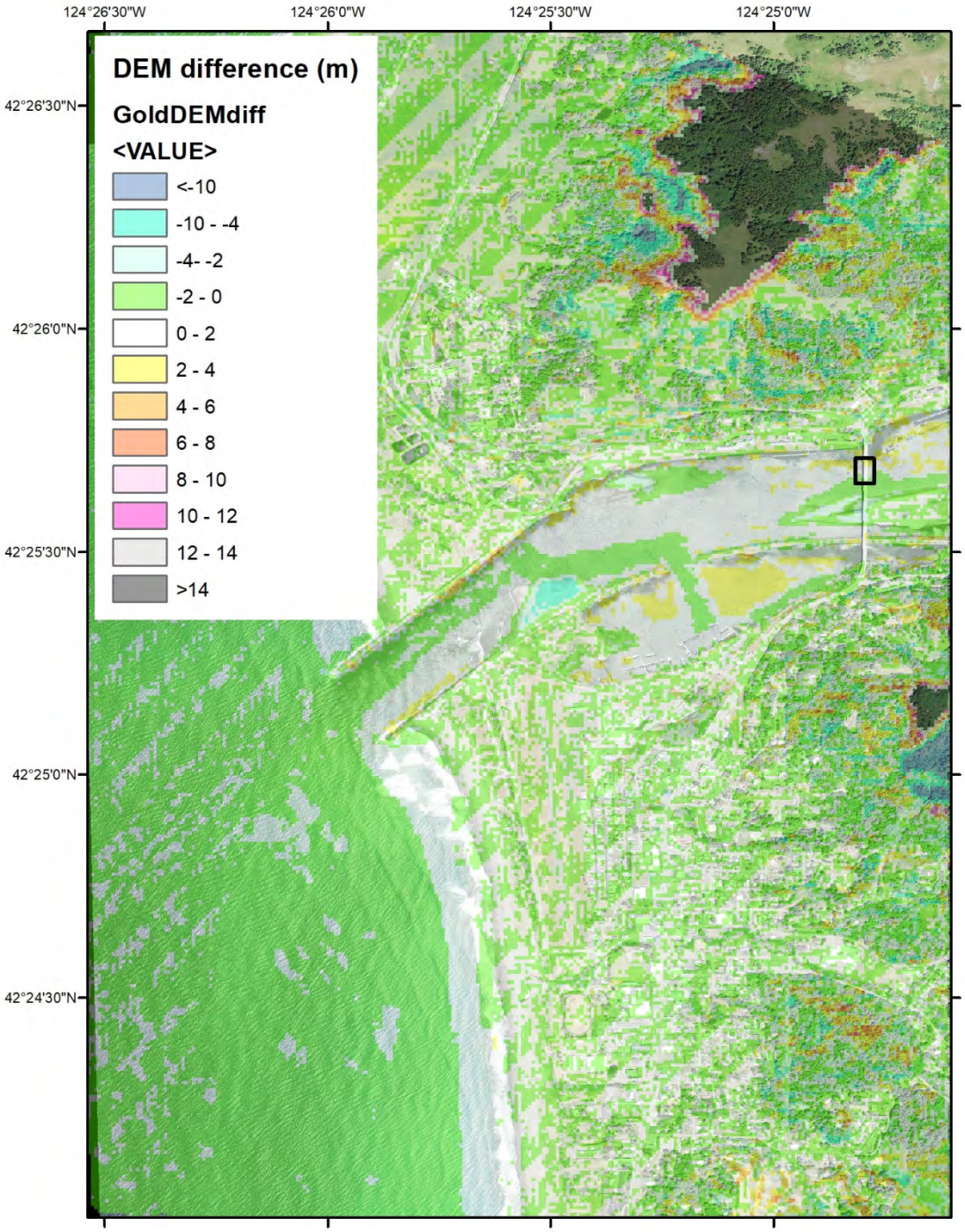

Figure A-21. DEMs at the Highway 101 bridge over the Rogue River at Gold Beach. Observation point is circled.

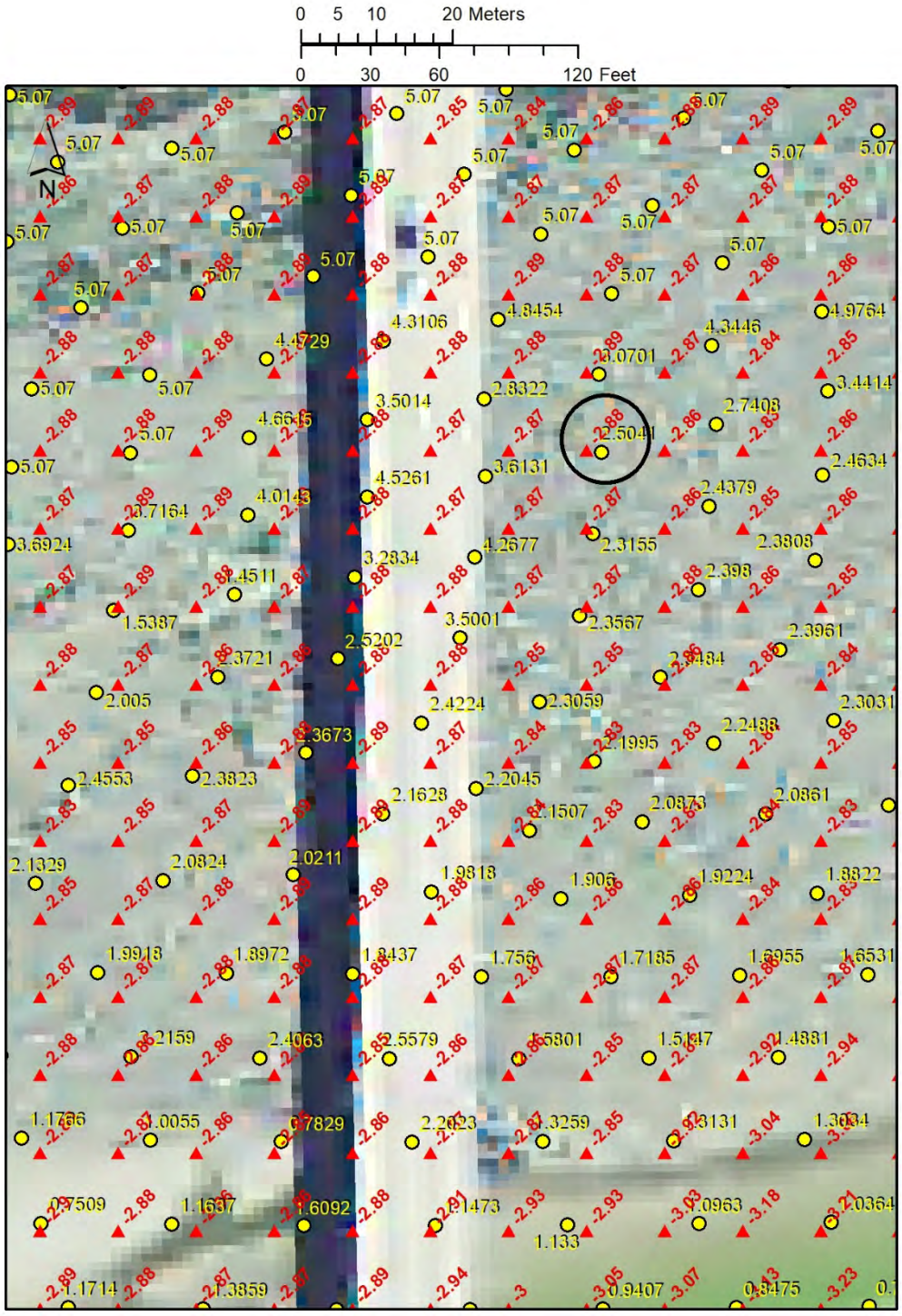

APPENDIX B. COMPARISON DATA

Table B-1 provides representative comparisons at each site depicted in Appendix A (circled AECOM and DOGAMI grid points) of maximum tsunami current velocity, flow depth, momentum flux, and initial ground elevation. In each case the two grid points were picked to be closely adjacent with the closest DEM match between AECOM (Thio, 2019) and DOGAMI (Witter and others, 2011; Priest and others, 2013; Allan and others, 2018). All AECOM simulations use a Manning friction coefficient, n = 0.025; All DOGAMI simulations use n = 0 unless otherwise specified in the Tsunami Simulation Parameter column (i.e., the two Columbia River simulations of the DOGAMI L1 scenario with n = 0.025 and n = 0.03 by Allan and others [2018]).

Table B-1. Velocity and flow depth match of DOGAMI tsunami scenarios to AECOM (boldface red numbers). Hwy = highway; n = Manning friction coefficient, DEM = digital elevation model; ? = uncertain owing to mismatch of AECOM and DOGAMI DEMs at the locality; est. = estimated; defm = coseismic vertical deformation; max. = maximum.

Tsunami Simulation Parameter	Astoria Col R Hwy 101 Bridge	Seaside Near Hwy 101 Bridge	Cannon Beach Hwy 101 Bridge	Siletz River Hwy 101 Bridge	Yaquina Bay Hwy 101 Bridge North	Alsea Bay Hwy 101 Bridge South	Near Yachats Hwy 101 Bridge[1]	Coquille River Hwy 101 Bridge, Bandon[2]	Coquille River Mouth at Bandon[2]	Gold Beach Hwy 101 Bridge
AECOM Maximum Velocity (m/s)	**1.4**	**4.8**	**8.1**	**4.2**	**7.5**	**11.5**	**7.1**	**2.1**	**6.3**	**6.9**
XXL1 Maximum Velocity (m/s)			5.7					10.1	11.0	
XXL2 Maximum Velocity (m/s)								8.3	12.1	
XXL3 Maximum Velocity (m/s)								9.1	11.5	
XL1 Maximum Velocity (m/s)	3.9	7.2	5.9	10.2	7.6	18.6	9.3	10.6	12.4	11.4
XL2 Maximum Velocity (m/s)								10.5	9.7	
XL3 Maximum Velocity (m/s)								9.3	10.9	
L1 Maximum Velocity (m/s)	2.5	5.6	5.7	5.8	7.0	14.1	7.3	8.9	8.0	9.2
L1 n = 0.025 Maximum Velocity (m/s)	1.7									
L1 n = 0.03 Maximum Velocity (m/s)	1.6									
L2 Maximum Velocity (m/s)								8.2	7.8	
L3 Maximum Velocity (m/s)								8.1	8.1	
M1 Maximum Velocity (m/s)	1.8	5.2	5.2	3.5	6.5	9.4	5.0	5.0	6.6	6.9
M2 Maximum Velocity (m/s)								4.3	5.7	
M3 Maximum Velocity (m/s)								4.6	6.1	

[1]Point is located outside of estuary channel to match the ground elevation of Thio (2019), which misses the channel in this locality.

[2]Bandon momentum flux data for DOGAMI scenarios XXL2, XXL3, L2, L3, M2, M3, SM2, and SM3 are available but not processed for analysis at this time.

(table continued on next page)

Tsunami Simulation Parameter	Astoria Col R Hwy 101 Bridge	Seaside Near Hwy 101 Bridge	Cannon Beach Hwy 101 Bridge	Siletz River Hwy 101 Bridge	Yaquina Bay Hwy 101 Bridge North	Alsea Bay Hwy 101 Bridge South	Near Yachats Hwy 101 Bridge[1]	Coquille River Hwy 101 Bridge, Bandon[2]	Coquille River Mouth at Bandon[2]	Gold Beach Hwy 101 Bridge
SM1 Maximum Velocity (m/s)	1.1							2.7	4.46	6.3
SM2 Maximum Velocity (m/s)								2.4	4.54	
SM3 Maximum Velocity (m/s)								2.4	4.19	
D200 Maximum Velocity (m/s)								0.1	0.557	
AECOM Maximum Flow Depth (m)	**24.2**	**11.9**	**17.0**	**6.8**	**19.7**	**9.6**	**10.9**	**7.5**	**13.1**	**9.2**
AECOM Max. Flow Depth adjusted to DOGAMI DEM (m)	**25.4**	**11.5**	**17.3**	**6.7**	**20.0**	**9.6**	**11.1**	**7.4**	**13.2**	**9.1**
XXL1 Maximum Flow Depth (m)			19.5					28.6	29.1	
XXL2 Maximum Flow Depth (m)								27.1	26.2	
XXL3 Maximum Flow Depth (m)								28.3	26.8	
XL1 Maximum Flow Depth (m)	28	17.4	18.6	13.4	22.5	13.9	11.7	27.7	27.2	35.7
XL2 Maximum Flow Depth (m)								24.5	24.7	
XL3 Maximum Flow Depth (m)								27.7	25.2	
L1 Maximum Flow Depth (m)	25.0	10.1	10.1	6.0	19.4	8.0	5.2	18.6	20.9	21.8
L1 n = 0.025 Maximum Flow Depth (m)	23.3									
L1 n = 0.03 Maximum Flow Depth (m)	23.0									
L2 Maximum Flow Depth (m)								15.0	19.1	
L3 Maximum Flow Depth (m)								16.2	19.5	
M1 Maximum Flow Depth (m)	23.4	5.6	6.6	2.9	17.5	3.9	1.8	8.7	16.5	14.2
M2 Maximum Flow Depth (m)								7.9	15.3	
M3 Maximum Flow Depth (m)								8.1	15.6	
SM1 Maximum Flow Depth (m)	22.1							7.1	13.6	8.6
SM2 Maximum Flow Depth (m)								7.0	12.7	
SM3 Maximum Flow Depth (m)								6.9	12.9	
D200 Maximum Flow Depth (m)								5.6	9.0	

[1]Point is located outside of estuary channel to match the ground elevation of Thio (2019), which misses the channel in this locality.

[2]Bandon momentum flux data for DOGAMI scenarios XXL2, XXL3, L2, L3, M2, M3, SM2, and SM3 are available but not processed for analysis at this time.

(table continued on next page)

Tsunami Simulation Parameter	Astoria Col R Hwy 101 Bridge	Seaside Near Hwy 101 Bridge	Cannon Beach Hwy 101 Bridge	Siletz River Hwy 101 Bridge	Yaquina Bay Hwy 101 Bridge North	Alsea Bay Hwy 101 Bridge South	Near Yachats Hwy 101 Bridge[1]	Coquille River Hwy 101 Bridge, Bandon[2]	Coquille River Mouth at Bandon[2]	Gold Beach Hwy 101 Bridge
AECOM Momentum Flux (m^3/s^2)	**36**	**273**	**644**	**107**	**921**	**950**	**188**	**22**	**103**	**382**
XXL1 Max. Momentum Flux (m^3/s^2)	437		553		1,228					
XL1 Max. Momentum Flux (m^3/s^2)	405	635	513		907	3,358	771	3,107	4,178	
L1 Max. Momentum Flux (m^3/s^2)	159	262	257	189	763	1,411	259	1,422	494	1,694
L1 n = 0.025 Momentum Flux (m^3/s^2)	71									
L1 n = 0.03 Momentum Flux (m^3/s^2)	57									
M1 Max. Momentum Flux (m^3/s^2)	74	76	166	27	525	326	38	218	291	540
SM1 Max. Momentum Flux (m^3/s^2)	28							54		222
Pre-defm DEM AECOM-DOGAMI at MHW	−0.8	0.4	0.1	0.3	0.2	0.2	0.3	0.5	0.3	0.6
Pre-defm? DEM AECOM (m MHW)[3]	**19.3**	**−0.47**	**0.65**	**1**	**11.8**	**0.5**	**−6.8**	**5.33**	**7.25**	**2.88**
Pre-defm DEM DOGAMI (m MHW)	20.1	−0.9	0.6	0.7	11.6	0.4	−7.1	4.9	7.0	2.3
Pre-defm DEM DOGAMI (m MHHW)	20.3	−0.7	0.8	0.9	11.8	0.6	−6.9	5.1	7.2	2.5
Pre-defm DEM DOGAMI D200 grid (MHW)								4.9	6.7	
Pre-defm DEM DOGAMI D200 grid (MHHW)								5.1	6.9	

[1]Point is located outside of estuary channel to match the ground elevation of Thio (2019) which misses the channel in this locality.

[2]Bandon momentum flux data for DOGAMI scenarios XXL2, XXL3, L2, L3, M2, M3, SM2, and SM3 are available but not processed for analysis at this time.

[3]Depths below sea level = negative numbers for the original AECOM grid; positive for DOGAMI grids, but all are shown positive here.

APPENDIX C. MOMENTUM FLUX MAP COMPARISONS

Figure C-1 through **Figure C-10** illustrate raster maps of momentum flux for the DOGAMI (Priest and others, 2013) L1 tsunami simulation with zero friction compared to the AECOM (Thio, 2019) simulations at the same areas as raster maps illustrating DEM differences in Appendix A. The L1 scenario is chosen because it has the best overall match to the 1,000-yr exceedance wave heights of AECOM at 100 m depth offshore (**Figure 3-5**). In each case a map of the L1 minus the AECOM values is above a map of L1 on the left and AECOM on the right. Each map has a rectangle illustrating the map area of the corresponding detailed views of the computational grids of Appendix A.

Figure C-1. Comparison of momentum flux from DOGAMI scenario L1 with zero friction (n = 0) relative to AECOM at Astoria. Maps show (A) L1 minus AECOM, (B) L1, and (C) AECOM. Box is locality of computational grid map in Appendix A.

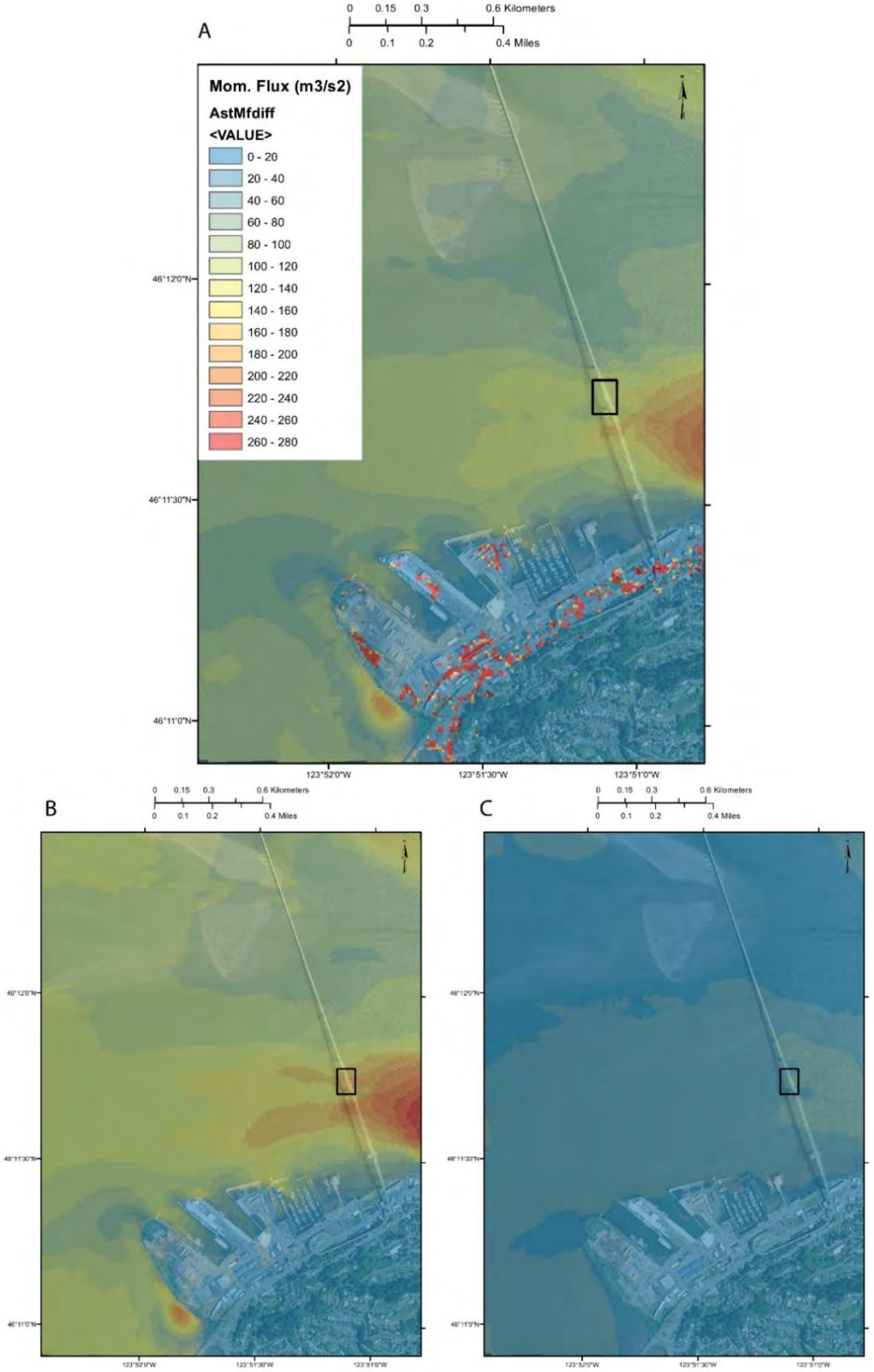

Figure C-2. Comparison of momentum flux from DOGAMI scenario L1 with zero friction (n = 0) relative to AECOM at Seaside. Maps show (A) L1 minus AECOM, (B) L1, and (C) AECOM. Box is locality of computational grid map in Appendix A.

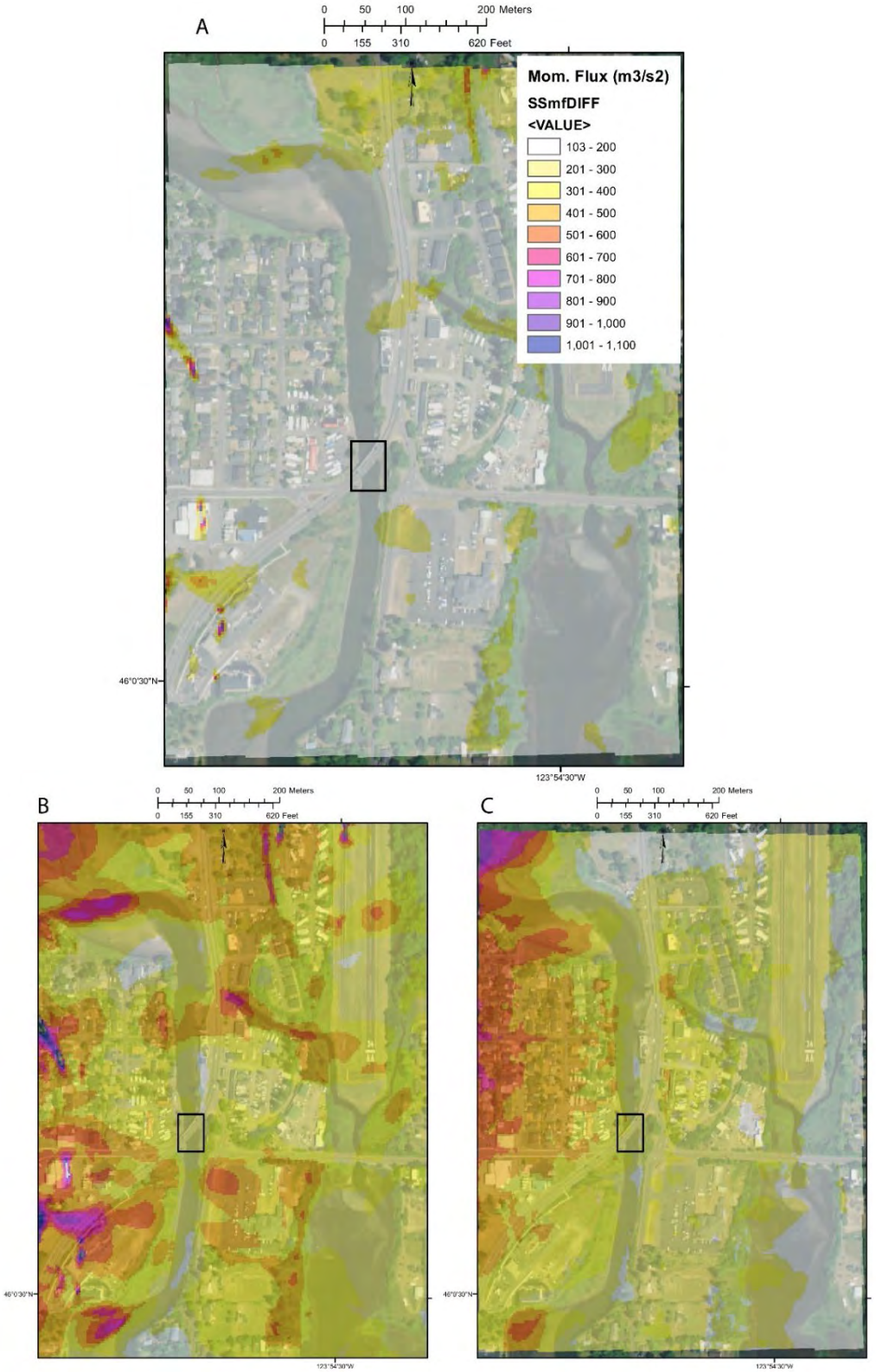

Figure C-3. Comparison of momentum flux from DOGAMI scenario L1 with zero friction (n = 0) relative to AECOM at Cannon Beach. Maps show (A) L1 minus AECOM, (B) L1, and (C) AECOM. Note that the legend color ramp for map A differs from the others owing to negative values. Box is locality of computational grid map in Appendix A.

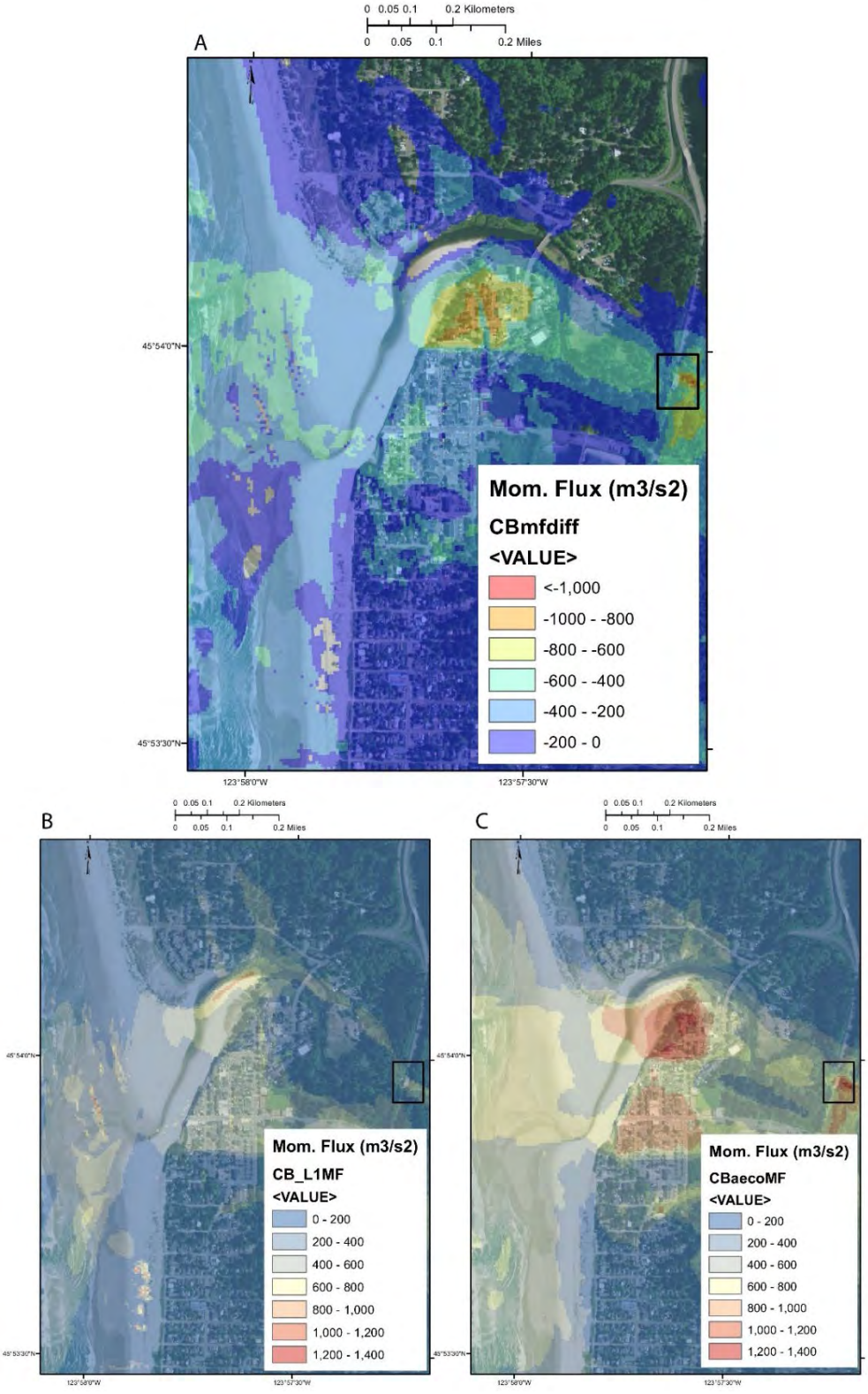

Figure C-4. Comparison of momentum flux from DOGAMI scenario L1 with zero friction (n = 0) relative to AECOM at Siletz Bay, Lincoln City. Maps show (A) L1 minus AECOM, (B) L1, and (C) AECOM. Box is locality of computational grid map in Appendix A.

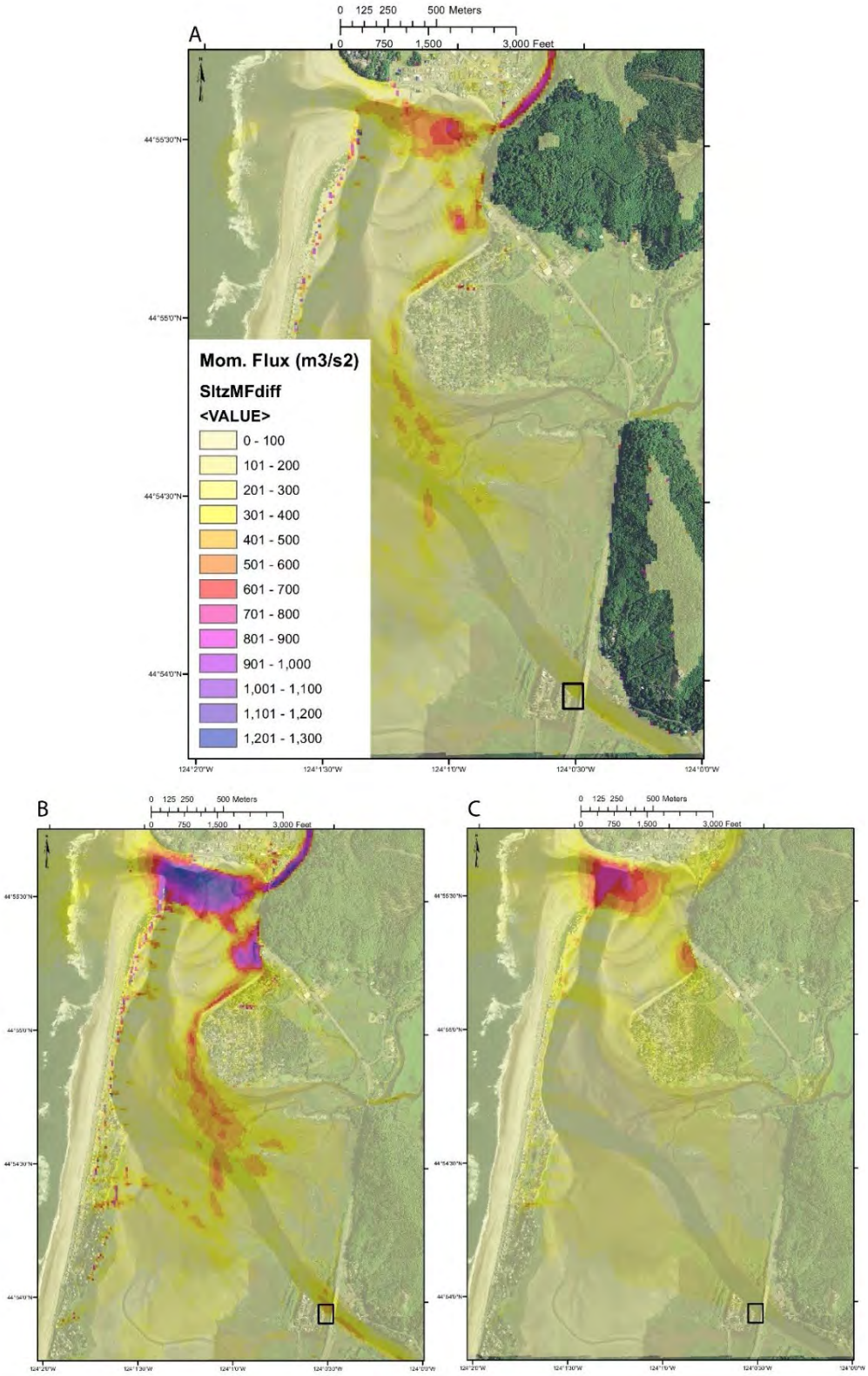

Figure C-5. Comparison of momentum flux from DOGAMI scenario L1 with zero friction (n = 0) relative to AECOM at Yaquina Bay, Newport. Maps show (A) L1 minus AECOM, (B) L1, and (C) AECOM. Box is locality of computational grid map in Appendix A.

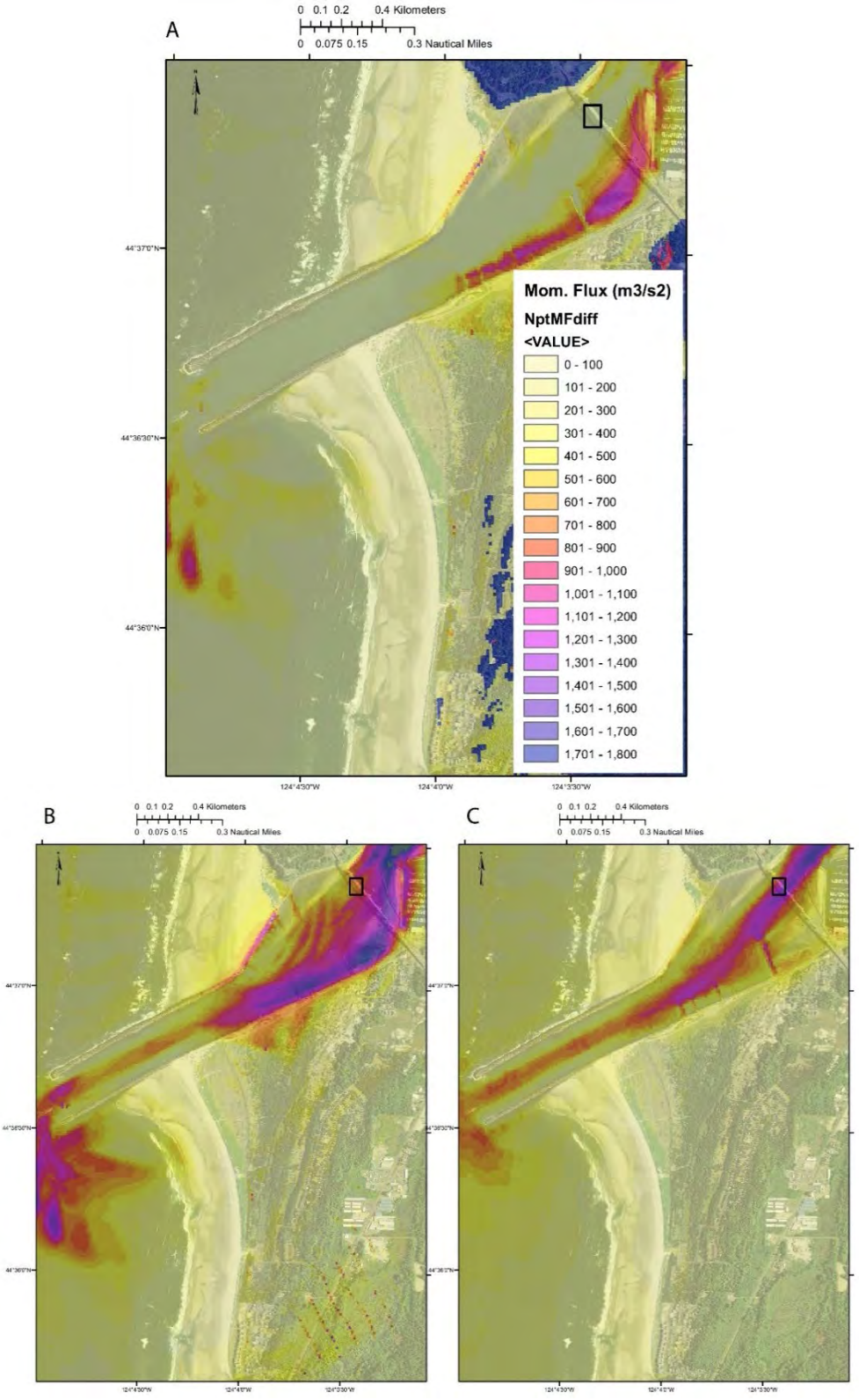

Figure C-6. Comparison of momentum flux from DOGAMI scenario L1 with zero friction (n = 0) relative to AECOM at Alsea Bay, Waldport. Maps show (A) L1 minus AECOM, (B) L1, and (C) AECOM. Box is locality of computational grid map in Appendix A.

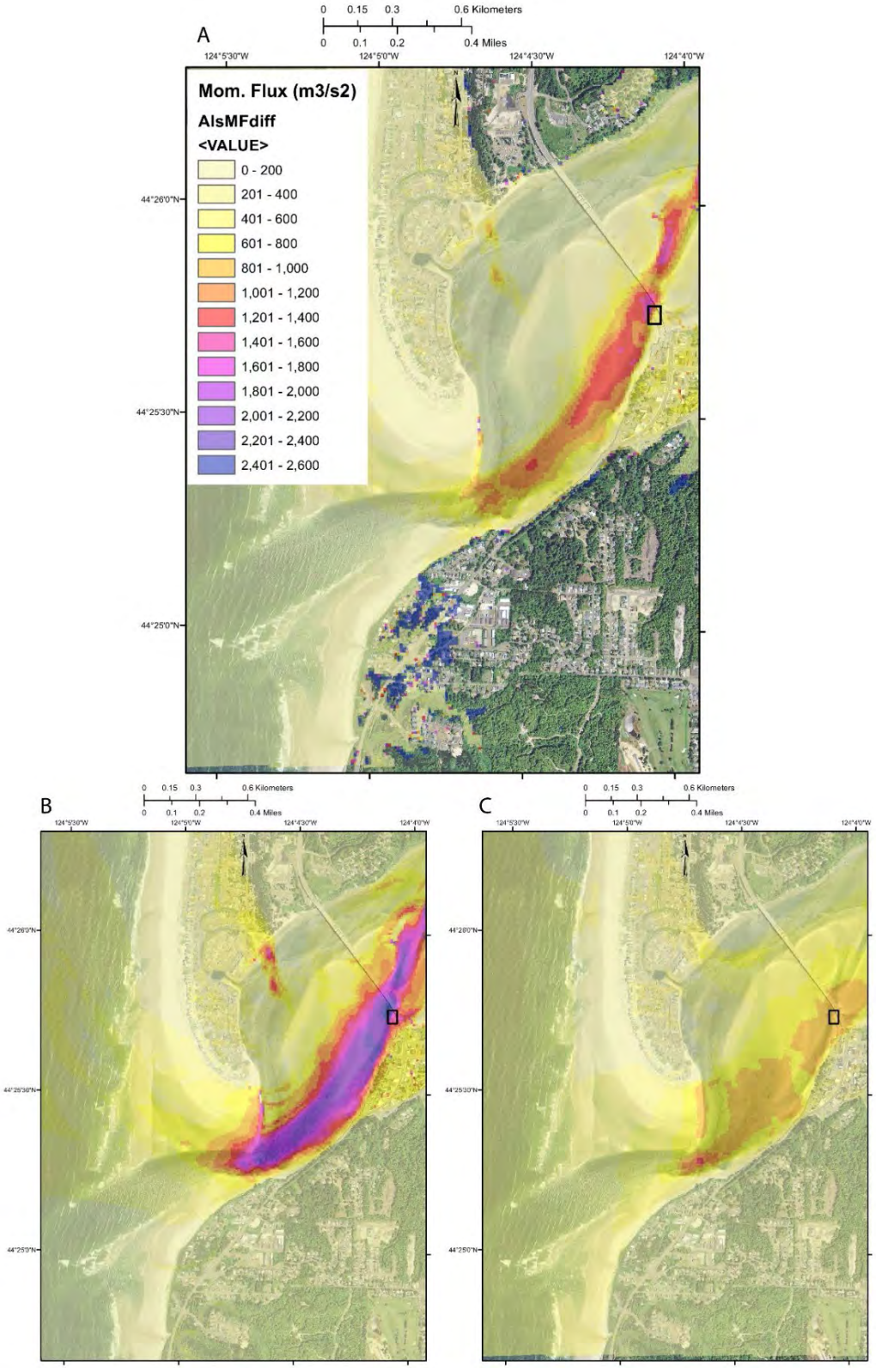

Figure C-7. Comparison of momentum flux from DOGAMI scenario L1 with zero friction (n = 0) relative to AECOM at Yachats. Maps show (A) L1 minus AECOM, (B) L1, and (C) AECOM. Note that map A has negative numbers and thus additional colors. Box is locality of computational grid map in Appendix A.

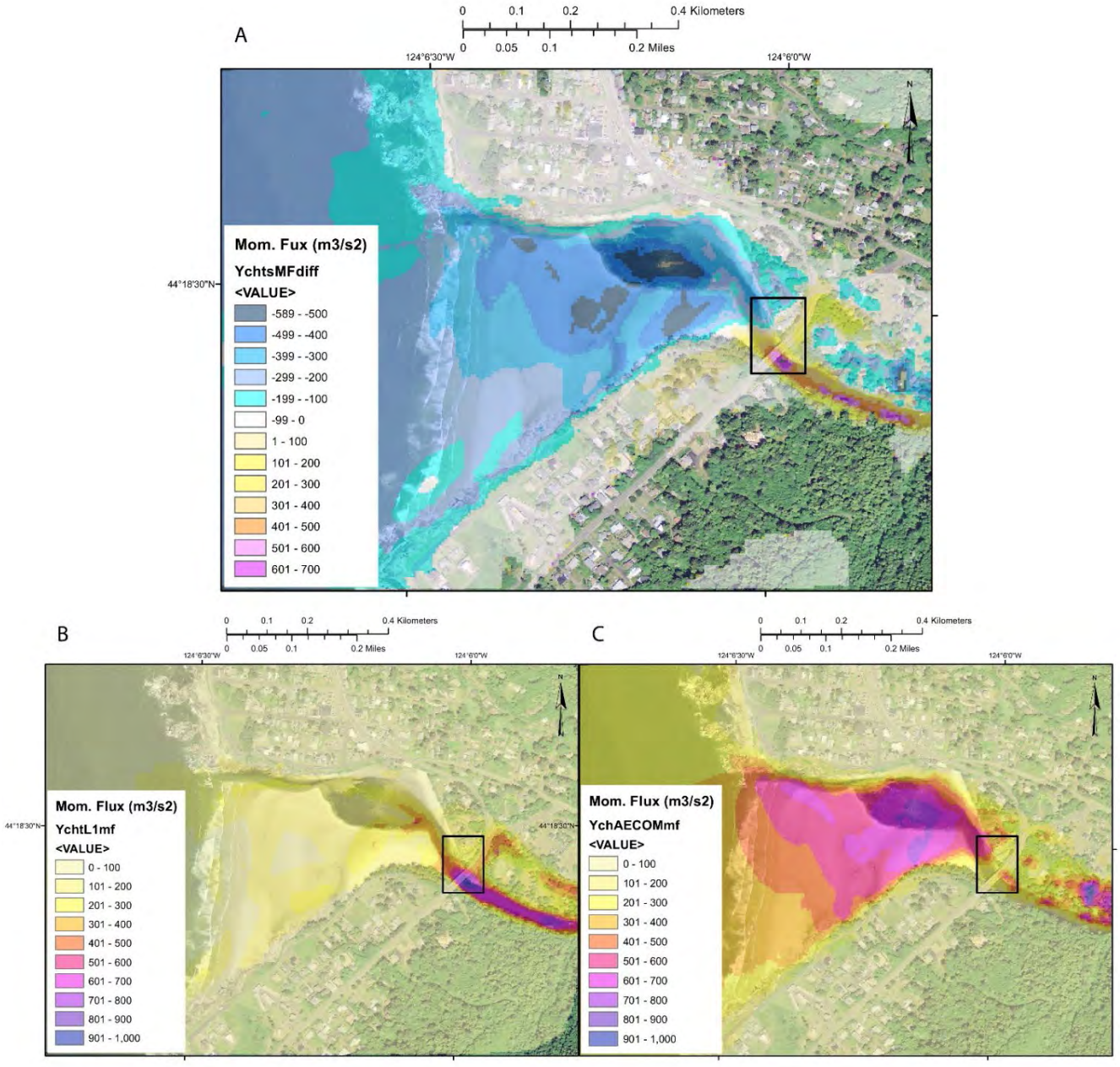

Figure C-8. Comparison of momentum flux from DOGAMI scenario L1 with zero friction (n = 0) relative to AECOM at the Highway 101 bridge over the Coquille River at Bandon. Maps show (A) L1 minus AECOM, (B) L1, and (C) AECOM. Map C has a different legend and color scheme because values are much less than maps A and B. Box is locality of computational grid map in Appendix A.

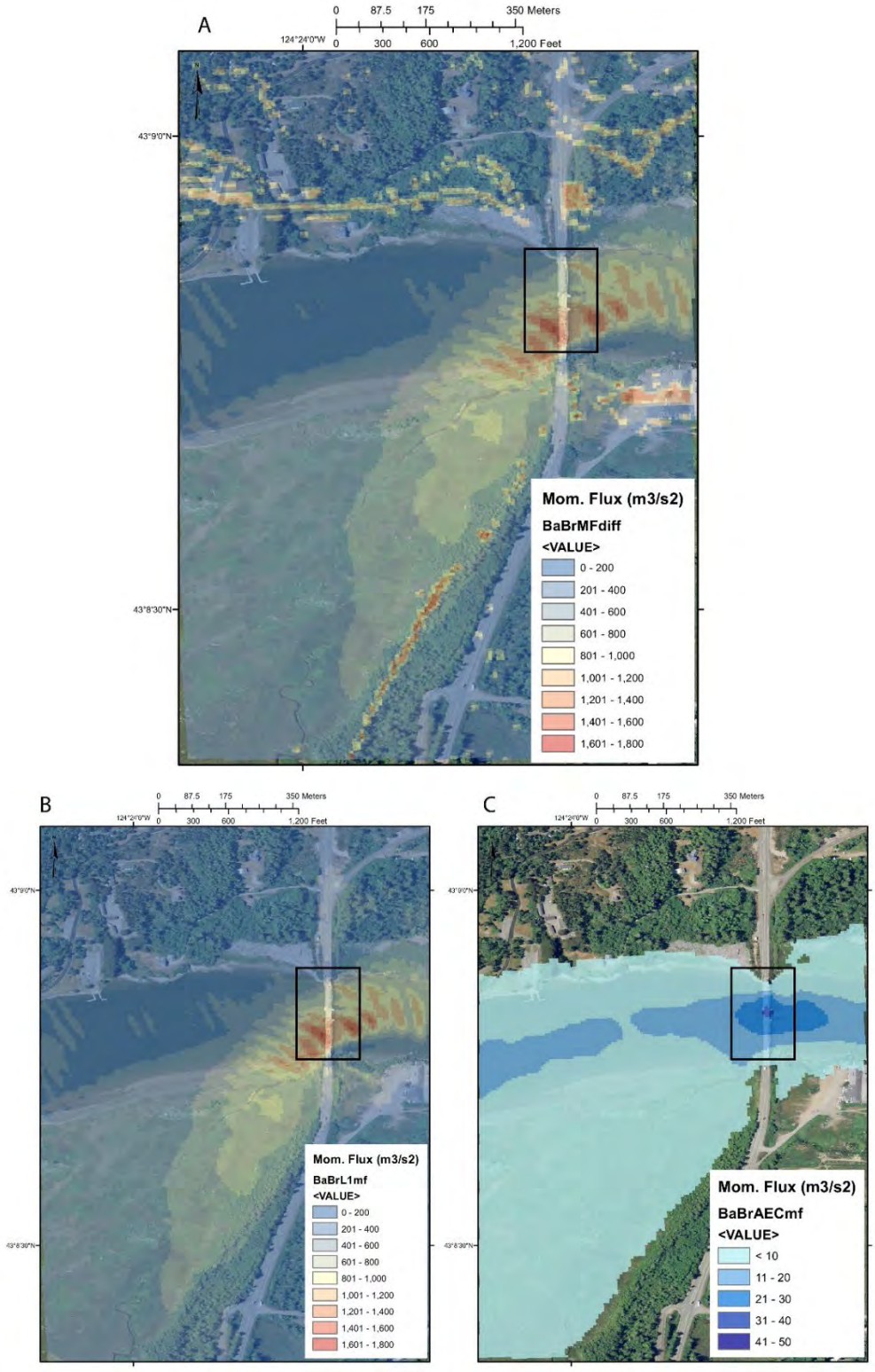

Figure C-9. Comparison of momentum flux from DOGAMI scenario L1 with zero friction (n = 0) relative to AECOM at the mouth of the Coquille River at Bandon. Maps show (A) L1 minus AECOM, (B) L1, and (C) AECOM. Box is locality of computational grid map in Appendix A.

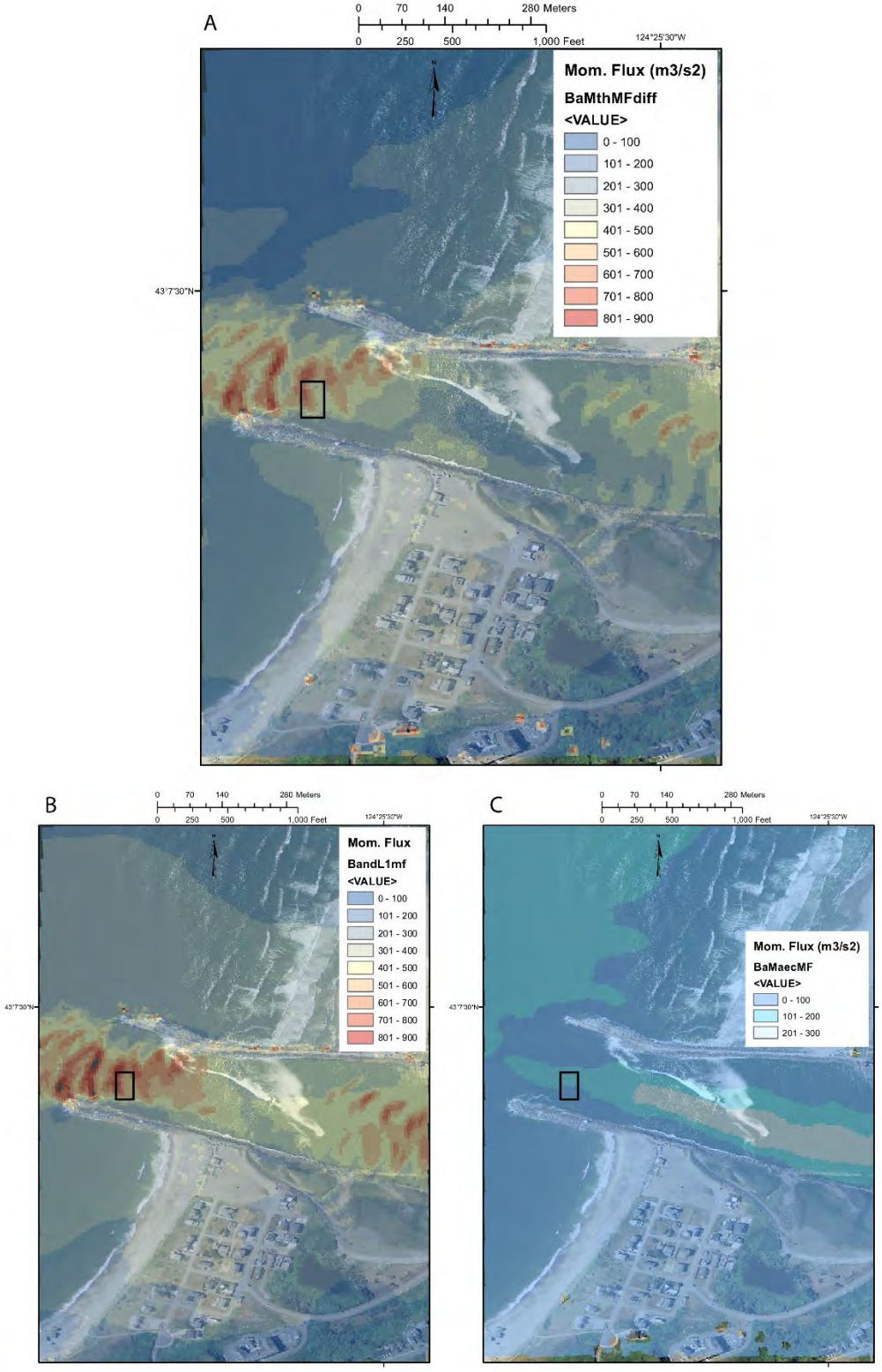

Figure C-10. Comparison of momentum flux from DOGAMI scenario L1 with zero friction (n = 0) relative to AECOM at Gold Beach. Maps show (A) L1 minus AECOM, (B) L1, and (C) AECOM. Box is locality of computational grid map in Appendix A.

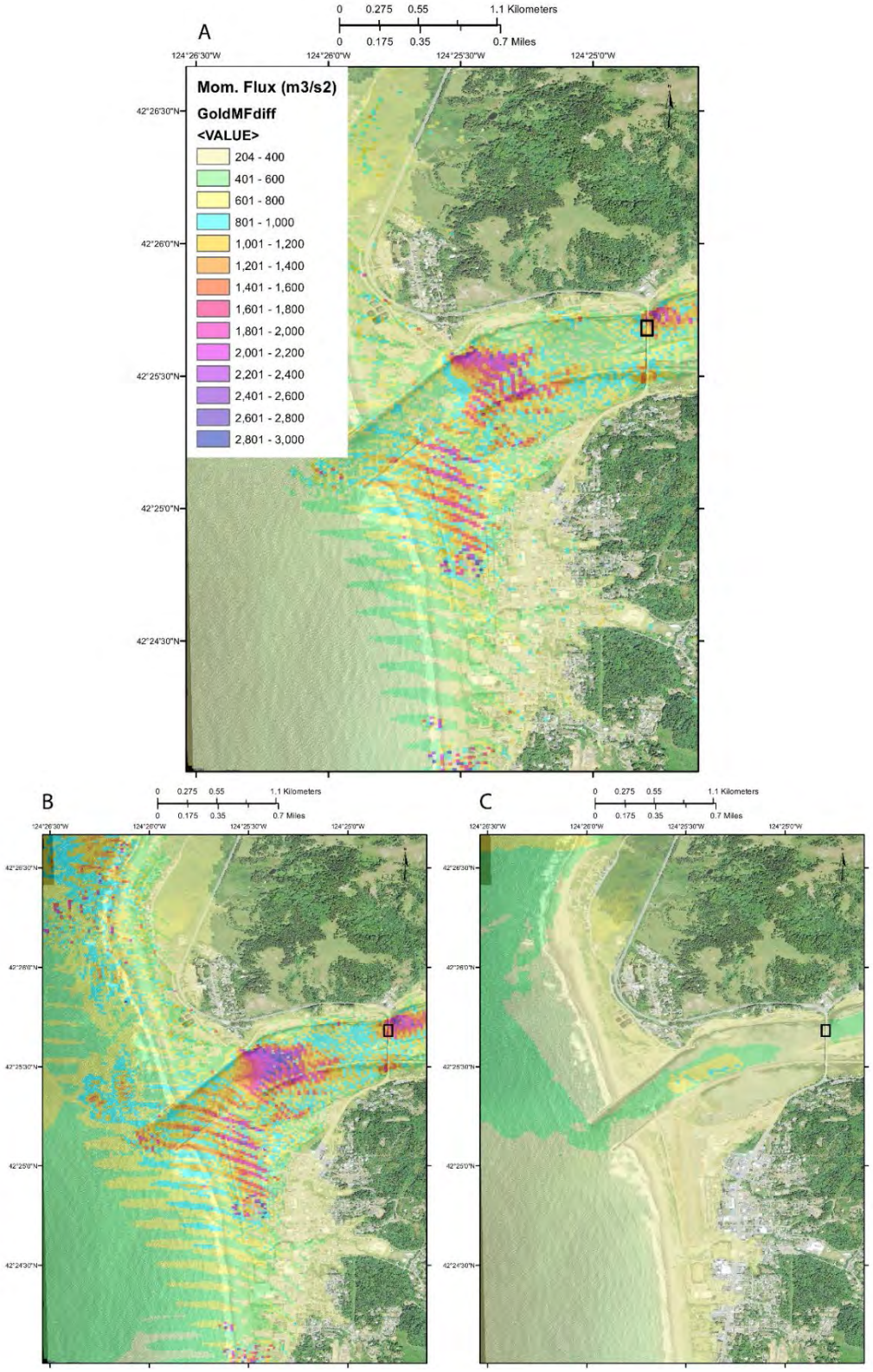

APPENDIX D. BACKGROUND INFORMATION ON CASCADIA TSUNAMI SOURCES

This appendix offers additional background information for the nontechnical reader on how tsunamis are generated from the Cascadia subduction zone (CSZ). Also included is some additional technical information on the splay fault model of Witter and others (2011, 2013) that is inappropriate for the main text.

D.1 Cascadia Subduction Zone (CSZ) Earthquake and Tsunami Basics

The CSZ is an active fault separating two major tectonic plates, the Juan de Fuca oceanic plate and the North American Plate (NAP) that are converging at rates of ~29–40 mm/y (**Figure D-1**). The plate interface breaks the seafloor at the base of the continental slope but then plunges at a low angle (~10-11°) eastward (**Figure D-2**). Because the earth gets hotter the deeper one goes, the interface starts out cold but gets hotter to the east. The cool, shallow part of the interface is where the two plates can be completely locked, producing no earthquakes until the locked zone is finally broken by the inexorable convergence. The two plates slide freely when temperatures are greater than about 450 °C, causing the rock to be plastic. The transition from full locking to full creep during the interseismic period is complex. For simplicity, it is sometimes modeled as a partially locked transition zone (**Figure D-3**).

At present, the two plates are fully locked, causing mainly the overriding NAP to buckle like a piece of rubber. The outer western edge bends downward while an upward bulge develops inland, so the whole outer part of the NAP is compressed and shortened eastward. The upward bulge is why many parts of the northwest coast are rising relative to sea level. The subduction zone earthquake allows mainly the NAP to spring westward, causing the outer edge of the plate (and overlying ocean) to rise, while the inner part of the plate, including much of the coast, subsides (**Figure D-2**). The more coseismic slip, the more up and down movement of the seafloor and overlying ocean. The upward bulge of the ocean splits in two: the eastern half heads toward the coast while the western half heads westward toward other parts of the Pacific. Both halves eventually reach shallow water where they slow down and rapidly rise in height until surging onshore as inundating tsunami floods. The tsunami height at the open coast is roughly proportional to the amount of slip on the subduction zone; see simulations of Priest and others (2009, 2010) that demonstrate this for the CSZ.

Right now, the fully locked zone on the CSZ plate interface is building up strain and accumulating a slip deficit at a rate equal to the convergence rate between the two tectonic plates. For example, it has been been 319 years since the last CSZ earthquake, so potential coseismic slip today could be the convergence rate of ~40 mm/yr times 319 years, which equals ~13 m. But the exact number would also involve slip deficit underused by previous earthquakes. The locked zone is where the hardest, coldest rocks are in contact across the plate interface. At Cascadia, it is roughly located below where the continental shelf begins to become the continental slope (the slope break).

Modern subduction zone earthquakes have coseismic slip that occurs in patches of high slip (sometimes confusingly called “asperities”) separated by areas of lower slip. The largest slip observed in modern times in these high-slip patches is on the order of 40–60 m. Where the convergence rate is fast, such as the Japan Trench, this amount of strain release can happen more often. The CSZ has half of the convergence rate as the Japan Trench, so such large slip events should not happen as often. In the Witter and others (2011, 2013) approach, they postulate that such extreme slips may have occurred only once in the last 10,000 yrs. They based this hypothesis on the ages and relative sizes of ~42 sand and silt deposits (turbidites) laid down when sand slurries were shaken off the continental slope by CSZ earthquakes over the last 10,000 years. One of the thickest of these turbidites was followed by ~1,200

years without geologic evidence of an earthquake. This long quiet period was the only one of its kind in the last 10,000 years, so we know that the CSZ built up strain for at least that long without an earthquake. That is the basis for the DOGAMI XXL earthquake source that releases 36–44 m of slip, which equals the amount of unreleased slip that could be accumulated over 1,200 years at the various CSZ convergence rates (**Figure D-1**). We argue in the technical part of this paper that use by Thio (2017, 2019) of numerous CSZ slip scenarios greatly exceeding XXL is hard to justify based on global observations and geological data from the CSZ.

D.2 Explanation of the "Bell-Shaped" Slip Distributions

The "bell shaped," buried coseismic fault slip distributions assumed by Witter and others (2011, 2013) and somewhat similar distributions of Thio (2017, 2019) are attempts to simulate two features of subduction zone earthquakes: apparent difficulty of coseismic fault ruptures to penetrate upward from the locked zone into soft rocks and lack of available unreleased slip downward where the rocks are hotter and more plastic. As an example of the latter, tsunami source models of Witter and others (2011, 2013) and Thio (2017, 2019) simulate the CSZ fault rupture during the earthquake by having the NAP lurch seaward less and less as one proceeds from the most locked part of the fault to the outer edge where the CSZ breaks the seafloor. This seems counterintuitive but matches observations of most modern subduction zone earthquakes with some exceptions. The most notable exception is the 2011 Tohoku-oki earthquake in Japan where the entire upper plate plowed into the oceanic trench sediments (Tsuji and others, 2013; Wang and others, 2018). Tohoku-style fault ruptures appear to require extreme fault displacements on the order of 50–60 m, which are probably rare on the CSZ owing to its low convergence rate and general rarity of this type of event in global observations. Given the seafloor and fault geometry at Cascadia, the models of Gao and others (2018) showed that even if the Tohoku-oki type trench-breaching rupture occurs at Cascadia, it does not produce higher tsunami waves than the buried rupture at the coast.

One hypothesis for slowing and then stopping the upper plate before it breaches the seafloor during an earthquake involves the accretionary prism or wedge (**Figure D-4**). The wedge is formed from oceanic sediment scrapped off the subducting plate onto the outer part of the overriding plate, so the outer part of the wedge is always much younger, less consolidated, and more saturated with water than the inner part. During the earthquake a fault rupture starts as a crack in the locked zone where the rock is relatively brittle, propagating in all directions but encountering some difficulty where it encounters softer rock that does not shatter like the brittle rock. Given enough time, the propagating fault rupture will penetrate the softer rocks, but not during the few seconds or minutes that cause the earthquake shaking and tsunami. The rupture will instead slowly penetrate the outer accretionary wedge over hours, days, or months following the earthquake. These "after slip" movements are usually too slow to cause seismic shaking or tsunamis. Rare exceptions are so called "tsunami earthquakes" where there is relatively little shaking, slower-than-normal fault rupture, and significant tsunamis.

The earthquake source models of Witter and others (2011, 2013) and Thio (2017, 2019) also predict decreasing coseismic slip deeper on the CSZ than the fully locked zone. Coseismic slip reaches zero where the plates are too hot to allow brittle seismic slip. The exact mechanics of fault rupture propagation in this transition zone between locked and freely sliding is not well understood, but it is basically a zone of creeping fault movements that do not allow accumulation of as much strain at the plate interface as the colder, more brittle parts of the subduction zone. A simple representation of CSZ transition zone is shown in **Figure D-3.**

D.3 Explanation of the Splay Fault Model

A possible candidate for a splay fault at CSZ is located essentially at the "backstop" where the youngest accretionary wedge rocks of the CSZ lie in contact with older, harder rocks and is a feature interpreted from geophysical surveys (**Figure D-5**). These youngest rocks accumulated during large outpourings of sediment from mainly the Columbia River but also other rivers during much wetter climates of the ice ages of the Pleistocene when sea levels were intermittently more than a hundred meters lower than at present. This sediment spread out onto the abyssal plain seaward of the subduction zone only to be scraped off onto the NAP over the last ~2 million years. Because there is less and less of this ice age sediment farther south away from the Columbia River, the piece of the accretionary wedge formed from these sediments decreases in width. The seafloor scarp of the splay fault thus gets closer and closer to the scarp of the megathrust in southern Cascadia until the two essentially merge (**Figure D-3**). Future geophysical surveys may suggest other splay fault candidates.

For their splay fault scenarios (i.e., SM1, M1, L1, XL1, and XXL1), Witter and others (2011, 2013) assume that this splay fault partitions all coseismic slip from the megathrust to the splay fault, creating a fault scarp where the splay breaches the seafloor. This scarp is quite far landward of where the megathrust reaches the seafloor in northern Cascadia, where the splay fault starts quite deep on the subduction zone. Obviously, the splay starts at progressively shallower depths as one proceeds south on the CSZ. As previously mentioned, the ~30° inclination of the splay fault greatly amplifies uplift for a given fault slip relative to the ~10-11° of the megathrust (**Figure 2-6**). Priest and others (2010) and Witter and others (2011, 2013) argued that larger earthquakes on the CSZ are more likely to partition slip from the megathrust to the splay fault and weighted their logic trees accordingly. If all slip goes to the splay, then no slip would occur on the megathrust seaward of the splay during or after the earthquake. This is a key difference between the splay fault model and the two buried rupture models of Witter and others (2011, 2013) where non seismic after-slip could occur seaward of the seismic rupture.

Figure D-1. Convergence rates of the Juan de Fuca and North America plates at the CSZ (IRIS [n.d.]).

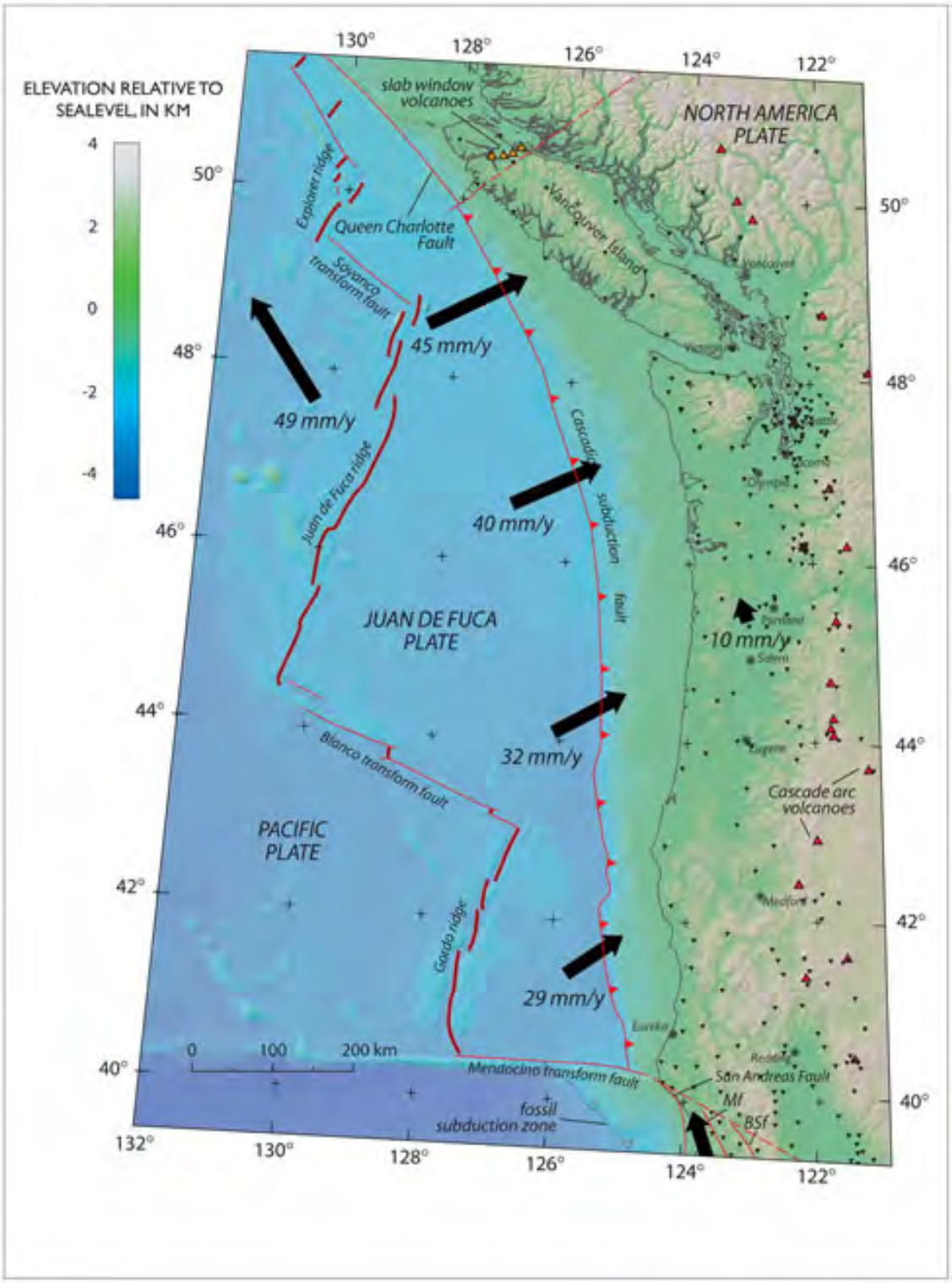

Figure D-2. How subduction zone earthquakes cause tsunamis (Atwater and others, 2005).

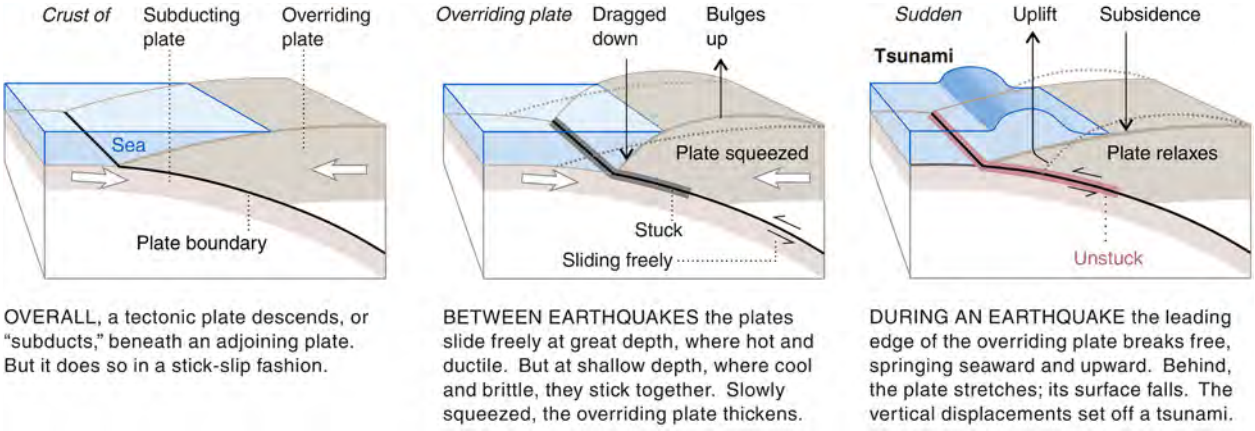

Figure D-3. Structural features of the Cascadia subduction zone used in fault dislocation modeling by DOGAMI (Witter and others, 2011, 2013). Black barbed line approximates the seaward edge of the subduction zone. White barbed line delineates the approximate location of the inferred splay fault system. Bold dashed line marks the downdip limit of rupture (Priest and others, 2010). Thin gray dashed lines are depth contours (km) of the subducting slab of McCrory and others (2004). Area of diagonal lines defines zone of landward-vergent structures in the outer accretionary wedge (Gutscher, and others, 2001; Adam and others, 2004) inferred to be weakly coupled to the subducting plate (see also the illustration of Figure 2-4). Gao and others (2018) have proposed other splay fault scenarios for the BC part of the margin. BC—British Columbia; WA—Washington; OR—Oregon; CA—California. (Modified from Witter and others, 2013.)

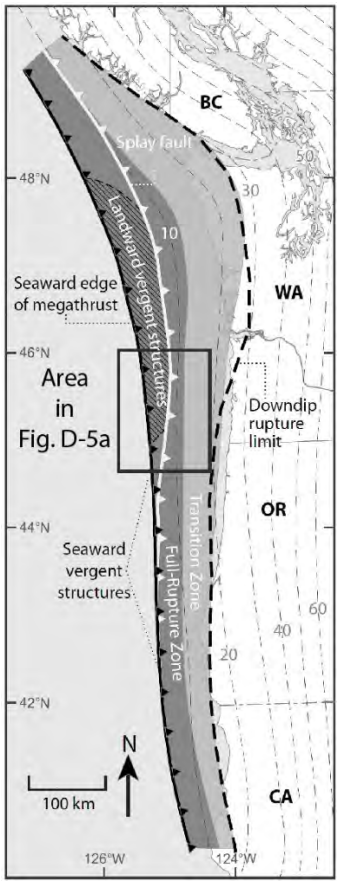

Figure D-4. Formation of an accretionary wedge by scraping oceanic sediments from the subducting plate onto the overriding plate (Martin, 2017). Only seaward-vergent thrust faults are depicted in the wedge. If the thrust faults were inclined in the opposite direction, they would be termed landward vergent, because of thrusting upward toward the land.

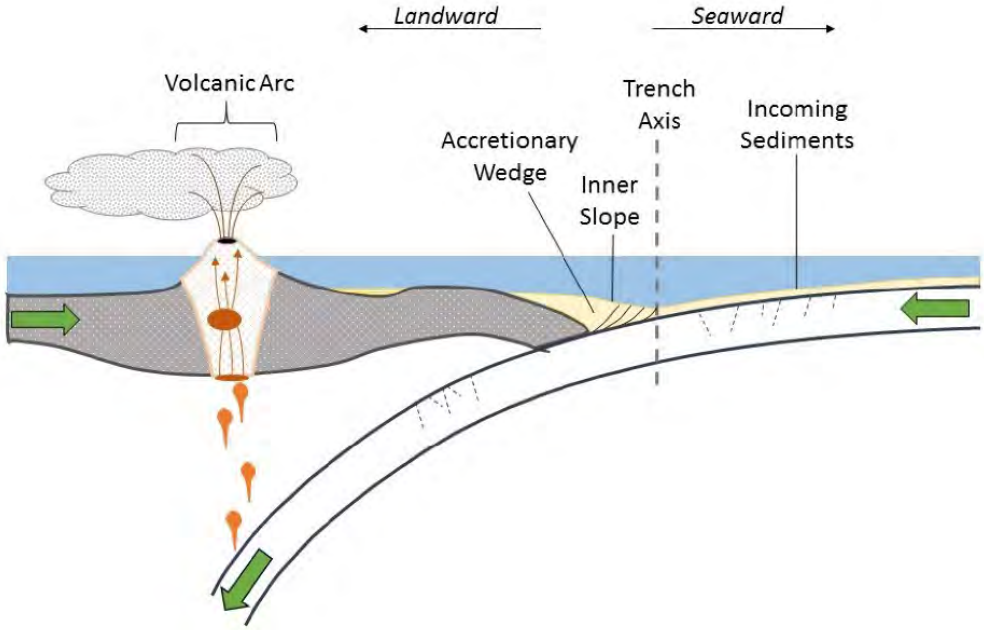

Figure D-5. Mapped Cascadia subduction zone splay fault. (A) Color bathymetry and shaded relief of the Cascadia accretionary complex offshore northern Oregon (map area shown in Figure A-12). Barbed black lines delineate mapped traces of the splay fault scarps (barbs point downdip) and an abrupt break in slope (Goldfinger, 1994). (B) Bathymetric profile (A–A') shows the abrupt break in slope separating younger accretionary wedge on the west from the older accretionary complex on the east (Goldfinger, 1994). The younger accretionary wedge is dominated by low-slope, landward-vergent structures, and widely spaced margin-parallel folds. The older accretionary complex features fold trends oriented normal to the convergence direction, a steeper slope, and seaward-vergent structures. The boundary between these two structural domains is a zone of active seaward-vergent splay faults, as shown in C. (C) U.S. Geological Survey seismic-reflection profile L-5-W077–12 (B–B' shown in A; Mann and Snavely, 1984) crosses the structural boundary and shows fault strands inferred to break the seafloor and deform young basin sediments. Vertical exaggeration is ~33:1 at the seafloor. The fault dips on this seismic profile are vertically exaggerated and would be very shallow (~30°) on a 1:1 depth profile. Taken from Witter and others (2013).